1-31-2013

Multifunctional oxidation electrocatalysts for direct alkaline fuel cells

Ulises Martinez

Ulises Martinez
Candidate

Chemical and Nuclear Engineering
Department

This dissertation is approved, and it is acceptable in quality and form for publication:

Approved by the Dissertation Committee:

Plamen Atanassov , Chairperson

Abhaya Datye

Tim Ward

Christopher Apblett

Boris Kiefer

MULTIFUNCTIONAL OXIDATION ELECTROCATALYSTS FOR DIRECT ALKALINE FUEL CELLS

by

ULISES MARTINEZ
B.A., Chemistry/Physics, Goshen College, 2004
M.S., Chemical Engineering, The University of New Mexico, 2009

DISSERTATION

Submitted in Partial Fulfillment of the

Requirements for the Degree of

Doctor of Philosophy
Engineering

The University of New Mexico

Albuquerque, New Mexico

December, 2012

DEDICATION

A mi familia, en especial a mi madre,

a quien le debo el poder haber llegado hasta aquí.

ACKNOWLEDGEMENTS

I would like to thank my advisor, Dr. Plamen Atanassov, for not only teaching me research strategies but also many history facts. I would also like to thank my co-advisor, Dr. Abhaya Datye, from whom I have learned the fundamentals in materials science. Thank you both, I have learned a great deal from both of you. Thank you to the rest of my committee members, Dr. Tim Ward, Dr. Chris Apblett, and Dr. Boris Kiefer, for taking time to be part of my dissertation.

I would like to thank group members from both Dr. Atanassov's and Dr. Datye's research groups for making this research experience more enjoyable. Specially thanks to all of those who had the patience to talk to me when I had many questions.

I would like to thank our collaborators at Daihatsu Motor Co. for giving me the opportunity to be involved in such novel research experience and seeing it develop in such a short amount of time.

Thanks to Dr. Datye for allowing me to participate in his PIRE program by spending a summer doing research at Denmark's Technical University. Thanks to Dr. Atanassov for supporting me in getting an NSF funded summer internship at Cabot-SMP. Both were great experiences from which I have gained invaluable knowledge.

To my friends, for being there when I needed some time to relax and forget about school. In particular to Jonathan Paiz and Angelica Benavidez, with whom I had the pleasure to travel the world. Thank you Angelica for keeping me sane through many sleepless nights.

Lastly, I would like to acknowledge the financial support I received from the National Science Foundation from a number of different fellowships: IGERT, GRFP, EIFP.

MULTIFUNCTIONAL OXIDATION ELECTROCATALYSTS FOR DIRECT ALKALINE FUEL CELLS

By

Ulises Martinez

B.A., CHEMISTRY/PHYSICS, GOSHEN COLLEGE, 2004

M.S., CHEMICAL ENGINEERING, THE UNIVERSITY OF NEW MEXICO, 2009

PH.D., ENGINEERING, THE UNIVERSITY OF NEW MEXICO, 2012

ABSTRACT

The need for the development of new technologies to reduce our dependence on fossil fuels requires the combination of different energy sources such as wind, solar, nuclear as well as new energy storage and powering devices. Amongst these new technologies fuel cells are a promising technology capable of transforming chemical energy stored in fuels into electric power at higher efficiencies than combustion processes. However, the commercialization of fuel cells has been limited due to the high costs associated with electrocatalysts needed for the corrosive environments in which proton-exchange membrane fuel cells operate. Electrocatalysts for such fuel cells are based on expensive noble metals such as platinum. Nevertheless, the resurging interest on the development of alkaline fuel cells presents a number of advantages addressing the limitations of proton-exchange membrane fuel cells. Alkaline fuel cells operate at high pHs which allow the use of a wider variety of inexpensive and abundant materials such as transition and rare-earth metals. Moreover, faster kinetics have been reported in alkaline

environments for both oxidation and reduction processes occurring at each of the electrodes.

The discussion related to the first part of this dissertation focuses on the development of novel electrocatalysts for the oxidation of hydrazine for application in direct hydrazine alkaline fuel cells. Hydrazine is a carbon-free nontraditional fuel with high energy density (5kW·h/kg), which is often considered a green fuel since its oxidation only produces nitrogen and water and does not contribute to the production of greenhouse gases emissions. It has been reported that transition metal catalysts such as Ni and Co demonstrate better performances than the commonly used Pt catalyst. Based on these preliminary findings, we have developed novel electrocatalysts with enhanced performance due to the addition of a second metal. α-NiZn electrocatalysts have shown improved performance due to an intrinsic effect cause by the alloying of an electron-dense atom such as Zn with Ni. Moreover, enhanced performance was also observed by the addition of a second phase, $La(OH)_3$. $La(OH)_3$ promotes the catalytic oxidation of hydrazine by providing oxygen species to the surface of the electrode for the dehydrogenation of hydrazine. Extensive *ex situ* characterization of materials using a number of different electron microscopy and X-ray spectroscopy techniques in combination with *in situ* electrochemical infrared studies provided insightful knowledge about the role of the components in the mechanism of the reaction.

The knowledge gained from the studies performed for the development catalyst for hydrazine oxidation was applied to a more complex reaction, the electrooxidation of ethanol in alkaline media. Complex kinetics have been reported for the oxidation reaction of ethanol resulting in only a partial oxidation producing acetate. Highly active

Pd/SnO_2 catalysts were developed with three times the performance of Pd. Moreover, thorough understanding of the mechanisms of the ethanol reaction at different electrolyte concentrations was carried out using *in situ* infrared studies. Results show that better performances were obtained at 1 M KOH, but ethanol only partially oxidized to acetate. On the other hand, when the concentration of the electrolyte was reduced to 0.1 M KOH complete oxidation of ethanol to CO_2 was observed. However, this resulted in higher overpotentials and lower rate constants. Mechanistic studies of reactions in both electrolytes concluded that higher concentrations of electrolyte allow for the oxidation of ethanol to occur at lower overpotentials due to the availability of hydroxide ions at the surface of the electrode, which participate in the oxidation of the adsorbed ethanol species. On the other hand, by the decreasing the concentration of electrolyte, diffusion of the hydroxide ions to the surface of the electrode is limited allowing the oxidation of ethanol to proceed to completion without desorbing the intermediate acetate product.

Table of Contents

List of Figures

List of Tables

1. Introduction

The need for the development of new technologies to reduce our dependence on fossil fuel resources along with reducing carbon emissions is one of the most significant challenges faced today. The solution to these challenges will involve a combination of different technologies such as solar, wind, geothermal, nuclear, in addition to alternative fuel sources, electrochemical and energy storage devices. Diversification to non-traditional fuels such as hydrogen, hydrazine, methanol, and ethanol, as well as the improvement of currently available storage and electrochemical devices will play an important role in powering from portable devices to automobile transportation. A promising emerging technology that can convert the chemical energy stored in such fuels into electric power is fuel cells.

Fuel cells consist of three main components: two electrodes, an anode and a cathode, and an electrolyte medium (Figure 1.1). Two complimentary reactions occur for the operation of a fuel cell. Oxidation of the fuel takes place at the anode while the cathode promotes the electrochemical reduction of the oxidant, *i.e.* oxygen from air. Oxidation of the fuel produces electrons that travel to the cathode through an outside circuit. The flow of electrons resulting from the electrochemical reaction at the anode is then used to power the device. Additionally, the ion-conducting electrolyte transports ions generated during the oxidation and reduction reactions between the electrodes [1].

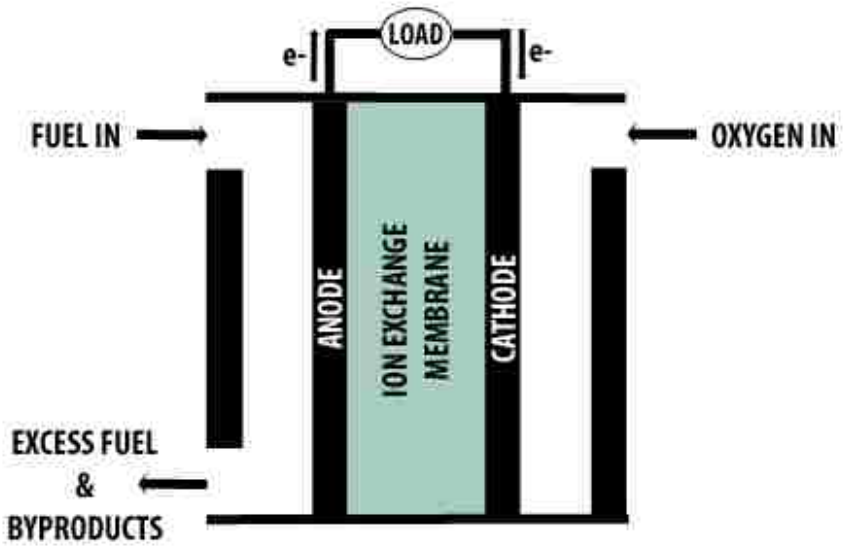

Figure 1-1. Schematic of the main components of a fuel cell.

For several decades the advancement of fuel cell technology has been focused on proton exchange membrane fuel cells (PEMFCs) mainly due to the success in the development of perfluorinated cation exchange membranes, specifically the discovery of Nafion by E.I. Dupont Company in the late 1960s [2]. Most research related to PEMFCs has focused on using hydrogen as the fuel. Although, hydrogen-fueled PEMFCs are well developed there are a number of drawbacks that have limited their commercialization. One of these drawbacks includes the need for a new infrastructure to safely store and transport hydrogen fuel. Steam reforming processes to produce hydrogen fuel onboard have been suggested. However, the steam reforming of organic fuels in mobile applications would require an onboard reformer operating at high temperature and producing products that could poison the PEMFC catalysts. PEMFC requires expensive noble metal catalysts such as platinum due to its corrosive environment. Thus, the need

for an onboard steam reformer would increase the cost of already costly PEMFCs. These limitations have significantly hindered success from fuel cell technology.

In order to eliminate the need for a new infrastructure required for hydrogen-fueled PEMFCs, direct liquid-fed fuel cells have been suggested. In direct liquid-fed fuel cells, a liquid fuel is directly oxidized at the anode without the need of a steam reformer. Nevertheless, the corrosive environment of PEMFCs still requires Pt-based catalysts for the oxidation and reduction processes in direct liquid-fed fuel cells. The combination of all of these limitations has shifted research interests to the resurgence of alkaline fuel cells (AFCs). Operation of AFCs at high pHs do not have the limitation of using only noble metal catalysts allowing for the development of novel electrocatalysts based on cheaper and more abundant materials. Furthermore, the ionic flow in AFCs is in the opposite direction of PEMFCs directing any possible fuel crossover back to the anode, which is a cause of significant voltage loss in PEMFCs.

The main drawback of AFCs is the sensitivity of the alkaline electrolyte to CO_2. In strong alkaline electrolytes, CO_2 forms carbonates according to the following reaction,

$$CO_2 + 2OH^- \rightarrow CO_3^{-2} + H_2O. \quad (1.1)$$

The poor solubility of carbonates leads to the precipitation of crystals capable of blocking electrolyte pathways as well as decreasing the pH of the electrolyte, both of which will result in decreased performance of AFCs [3, 4]. New interest in the development of AFCs has increased research focused to develop anion-exchange membranes (AEM) that will help reduce the formation of carbonates. Introducing quaternary ammonium moieties to polymer matrices is considered the most effective method of preparing AEMs [5, 6].

Varcoe *et al.* have made progress towards the development of AEM by using fluorinated polymers [7]. Fluorinated polymers are known for their good interface properties such as low surface tension and electrostatic loading in addition to good chemical and mechanical stability. Their membrane was based on poly(ethylene-co-tetrafluoroethylene) groups and exhibited enhanced tensile strength and improved conductivities of about 34 mS/cm at 50°C. Recently, Tanaka *et al.* have reported novel anion conductive membranes based on poly(arylene ether)s containing quaternary ammonium-substituted fluorene groups demonstrating high conductivity and durability [8]. Their reported conductivity was 144 mS/cm at 80°C which was retained for 5000 h. These reports demonstrate a promising future for the development of AEMs.

The principles of operation of PEMFCs and AEMFCs are similar. Figure 1.2 below highlights the main differences between both types of fuel cells.

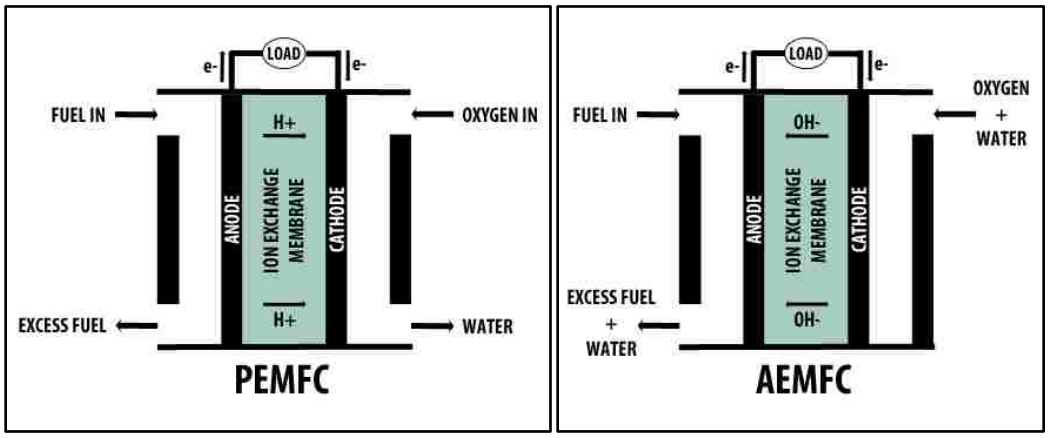

Figure 1-2. Comparison of working principles of PEMFCs and AFCs.

For PEMFCs the ion exchanged through the membrane is the hydrogen ion which travels from the anode to the cathode. Conversely, AEMFCs require membranes to transport

hydroxide ions from the cathode to the anode. Water is formed at the cathode through the reduction of oxygen in PEMFCs according to the following reaction,

$$O_2 + 4e^- + 4H^+ \rightarrow 2H_2O. \quad (1.2)$$

In the case of AEMFCs, the reduction of oxygen produces hydroxide ions at the cathode according to,

$$O_2 + 2H_2O + 4e^- \rightarrow 4OH^- . \quad (1.3)$$

In PEMFCs, the reduction of oxygen (ORR) is limited by slow kinetics with low exchange current densities ranging in the 10^{-10} A/cm^2 range. Furthermore, overpotentials for the ORR range between 200-300 mV contributing to the highest catalyst performance loss in PEMFCs. On the contrary, the kinetics of the ORR are much more rapid in alkaline environments [9]. Exchange current densities are about one to two orders of magnitude higher than in acid electrolytes. Additionally, the benefits observed for the oxygen reduction reaction are also observed for the oxidation reactions occurring at the anode [10, 11].

Alkaline fuel cell technology was first demonstrated by Francis Thomas Bacon starting in the late-1930s [12, 13]. Bacon's work was later licensed by Pratt & Whitney Division of United Technologies Corporation for the manufacturing of AFCs used to power the Apollo space shuttle flights in the 1960s [4]. Due to their success in space applications, AFCs were tested in many other applications. Allis-Chalmers Manufacturing Co. developed a 15 kW alkaline fuel cell stack to power a farm tractor. The fuel cell stack consisted of over 1000 cells with nickel-based catalysts and was able

to pull about 1.5 tons of weight (Figure 1.3). Allis-Chalmers maintained a research program with the U.S. Air Force building an AFC powered golf cart, a submersible, and a forklift.

Figure 1-3. Alkaline fuel cell tractor developed by Allis-Chalmers Manufacturing Co.

During the late 1990s, Zero Emission Vehicle Company (ZEVCO) launched its first prototype taxi in London using a 5 kW AFC with cobalt-based catalysts. Even though AFCs developed by Allis-Chalmers and ZEVCO used inexpensive transition metals as catalysts, the fuel used for these fuel cells remained hydrogen. Therefore, in order to transform fuel cell technology into an affordable and tangible technology the future might lie in the use of anion-exchange membranes, liquid fuels, and non-noble metal catalysts.

2. Electrochemical Processes

2.1 The Metal/Solution Interface

Electrochemical processes in fuel cells occur at the interface between the electron-conducting material (electrode) and an ionic conductive phase (electrolyte). It is at this metal/solution interface where electron transfer occurs between reacting chemical species. These electron transfer processes involve the chemisorption of the reactant, intermediates, and product species. Thus, the rates and mechanisms of reaction are dependent on the chemical structure of all species at the interface.

The Helmholtz model was the first model in reference to the metal/solution interface [14]. It was described as a simple capacitor with two layers, known as the electrochemical double layer. At one layer is the charged metal surface while the other is formed by a layer of ions in solution. This simplistic model was later modified by Louis Georges Gouy [15, 16] and David Chapman [17] independently to include the concept of a diffusion layer. The greatest concentration of charge would be adjacent to the electrode, where electrostatic forces are able to overcome thermal processes. Lesser concentrations would be found a greater distances from the electrode as the electrostatic forces become weaker. If either the charge of the electrode increases or the concentration of the electrolyte increases, the diffusion layer becomes more compact and the capacitance should increase. Even though the Gouy-Chapman was a significant improvement compared to the simple Helmholtz model, it had its limitations. The most unrealistic limitation was the unlimited differential capacitance. In other words, according to the Gouy-Chapman model at high polarizations the separation distance between the metal

and the ions in solution goes to zero. However, the ions cannot approach the surface any closer than its ionic radius. In the case that the ion is strongly solvated, the separation distance might even be higher. A model addressing these limitations was suggested by Stern [18]. Stern postulated an improved model by combining the Helmholtz model with the Gouy-Chapman model. Stern's model included an inner layer, also called the inner Helmholtz plane (IHP), which consisted of specifically adsorbed ions; an outer layer, or outer Helmholtz plane (OHP), consisting of solvated ions; and a diffusion layer which extends from the OHP into the bulk of the solution (Figure 2.1). The diffusion layer is composed of nonspecifically adsorbed solvated ions and its thickness depends on the ionic concentration of the solution. The structure of this Gouy-Chapman-Stern electrochemical double layer is important as it can affect the rates of electrochemical processes.

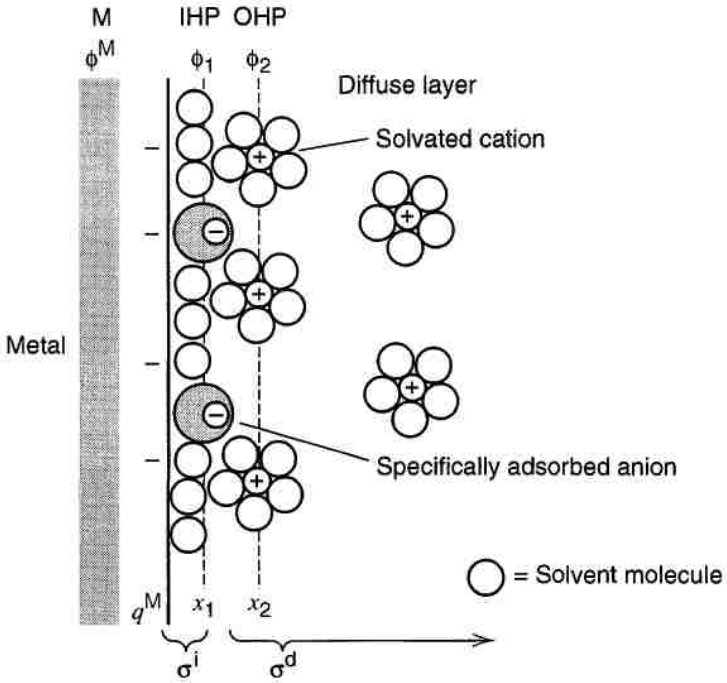

Figure 2-1. Gouy-Chapman-Stern model of the electrical double layer. Adapted from [19].

2.2 Electrochemical Kinetics and Thermodynamics

Interpreting the rate of an electrode reaction is more complex than deriving rates for homogeneous reactions. Electrochemical reactions are complex involving a series of different steps. The current (or electrode reaction rate) obtained from electrochemical reactions is governed by the rates of different processes.

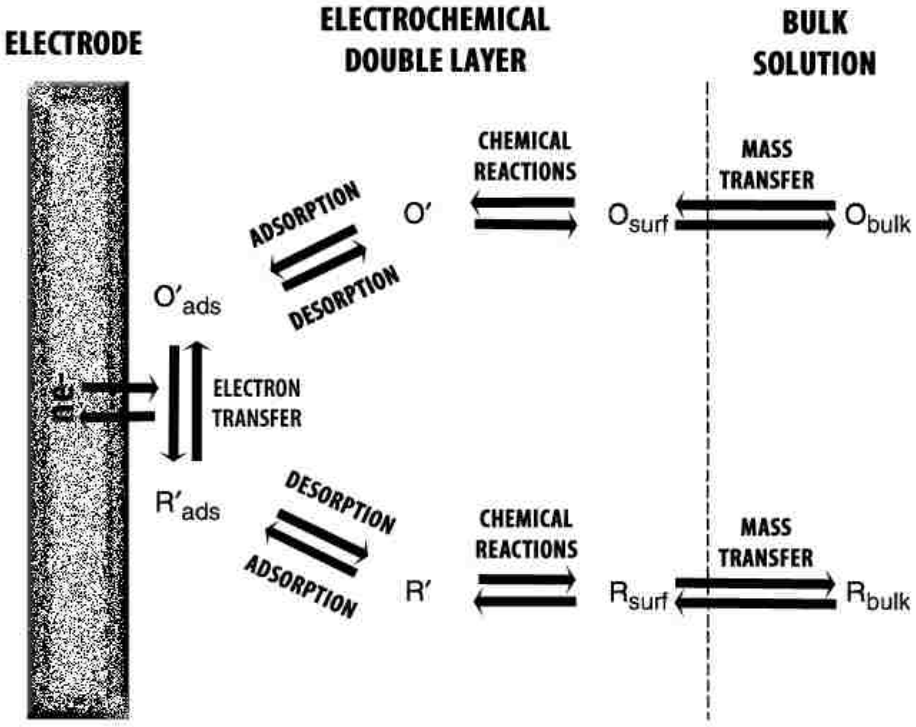

Figure 2-2. Different processes occurring at the metal/solution interface.

Figure 2.2 highlights some of the most important processes occurring at the surface of the electrode. The simplest electrochemical reactions involve the mass transfer of the reactants from the bulk solution to the electrode surface, an electron transfer involving nonadsorbed species, and mass transfer of the products back in to the bulk solution. Consequently, the overall rate of reaction will depend on both the rate of electrochemical

reaction on the surface, and the rate the electrochemically active species are supplied to the electrode surface.

In electrochemical reactions, the rate of reaction occurring at the electrode-electrolyte interface is described as follows:

$$rate = \frac{i}{nFA} = \frac{j}{nF} \tag{2.1}$$

where *i* is the current, *j* is the current density in A/cm^2, *n* is the stoichiometric number of electrons transferred in the reaction, and *F* is the Faraday constant (electric charge of one mole of electrons = 95485 C/mol). Information about the kinetics and structural properties of the electrochemical interface can be obtained from measurements of faradic and non-faradic currents as a function of the electrode potential and/or time.

Considering a simple reversible one step reaction where species *O* are being reduced to species *R* with a transfer of *n* number of electrons,

$$O + ne^- \leftrightarrow R.$$

The rate of the forward reaction can be written as follows,

$$r_f = k_f C_O(0,t) = \frac{i_f}{nFA} \tag{2.2}$$

In a similar way, the rate of the backward reaction is equal to,

$$r_b = k_b C_R(0,t) = \frac{i_b}{nFA} \tag{2.3}$$

where $C_O(0,t)$ and $C_R(0,t)$ are the surface concentrations of the reactants and products. Consequently, the net reaction rate is described as follows,

$$r_{net} = r_f - r_b = k_f C_O(0,t) - k_b C_R(0,t) = \frac{i_f - i_b}{nFA} = \frac{i_{net}}{nFA} \tag{2.4}$$

Assuming that the rate constants k_f and k_b, follow an Arrhenius form, they can be written as,

$$k_f = A_f e^{\left(-\frac{\Delta G_f}{RT}\right)} \tag{2.5}$$

$$k_b = A_b e^{\left(-\frac{\Delta G_b}{RT}\right)} \tag{2.6}$$

For an electrochemical system, the change in Gibbs free energy, ΔG, is given by

$$\Delta G = -nFE. \tag{2.7}$$

Therefore, if the potential is changed to a new potential by ΔE the energy barrier will also be modified. Equation (2.7) can then be used to write the rate constants in terms of an applied potential,

$$k_f = k_f^0 e^{\left(-\alpha n f (E - E^0)\right)} \tag{2.8}$$

$$k_b = k_b^0 e^{\left((1-\alpha) n f (E - E^0)\right)} \tag{2.9}$$

where $f = F/RT$, k^0 are the rate constants for the standard potentials, E^0, of the forward and backward reactions, α is the transfer coefficient and is related to the symmetry of the reaction. At E^0, the forward and reverse rate constants have the same value, *i.e.* $k_f^0 = k_b^0$

$= k^0$. Substituting the rate constants back into equation (2.4), a relation between current and potential can be obtained,

$$i_{net} = k^0 nFA[C_O(0,t)e^{\left(-\alpha nf\left(E-E^0\right)\right)} - C_R(0,t)e^{\left((1-\alpha)nf\left(E-E^0\right)\right)}]. \quad (2.10)$$

This relation is a very important used to describe electrode kinetics in terms of current and potential. Equation (2.10) is broadly known as the *Butler-Volmer* equation.

Several important parameters can be derived from the *Butler-Volmer* equation. At equilibrium the net current is equal to zero; therefore, equation (2.10) becomes,

$$0 = C_O(0,t)e^{\left(-\alpha nf\left(E-E^0\right)\right)} - C_R(0,t)e^{\left((1-\alpha)nf\left(E-E^0\right)\right)} \quad (2.11)$$

or

$$\frac{C_O(0,t)}{C_R(0,t)} = e^{\left(nf\left(E-E^0\right)\right)}. \quad (2.12)$$

At equilibrium the surface concentrations are equal to the bulk concentrations. Equation (2.12) can be rewritten to give another important relation in electrochemistry, known as the Nernst equation:

$$E_{eq} = E^0 + \frac{RT}{nF} ln \frac{C_O}{C_R}. \quad (2.13)$$

An important reference point for an electrochemical system is its equilibrium potential which can be obtained from the Nernst equation.

Even though at equilibrium the net current is zero, there is an exchange of electrons in both directions of the interface which are equal in magnitude but opposite in

charge. This magnitude is known as the exchange current density, i_0, and can be obtained from the *Butler-Volmer* equation,

$$i_0 = nFAk^0 C_O^{1-\alpha} C_R^{\alpha}. \tag{2.14}$$

Electrochemical reactions, however, do not occur at the thermodynamic equilibrium potential experimentally. A higher than the thermodynamic potential is needed in order for the reaction to occur. This additional potential is referred to as the overpotential, η, and is defined as,

$$\eta = E - E_{eq} \tag{2.15}$$

Reducing the overpotential value is the goal of electrocatalysts in fuel cells.

The combination of equations (2.10), (2.14) and (2.15), gives the current-overpotential equation widely used to describe electrode kinetics. The behavior obtained from equation (2.16) can be observed in figure 6.

$$i = i_0 [\frac{C_O(0,t)}{C_O} e^{(-\alpha n f \eta)} - \frac{C_R(0,t)}{C_R} e^{((1-\alpha) n f \eta)}] \tag{2.16}$$

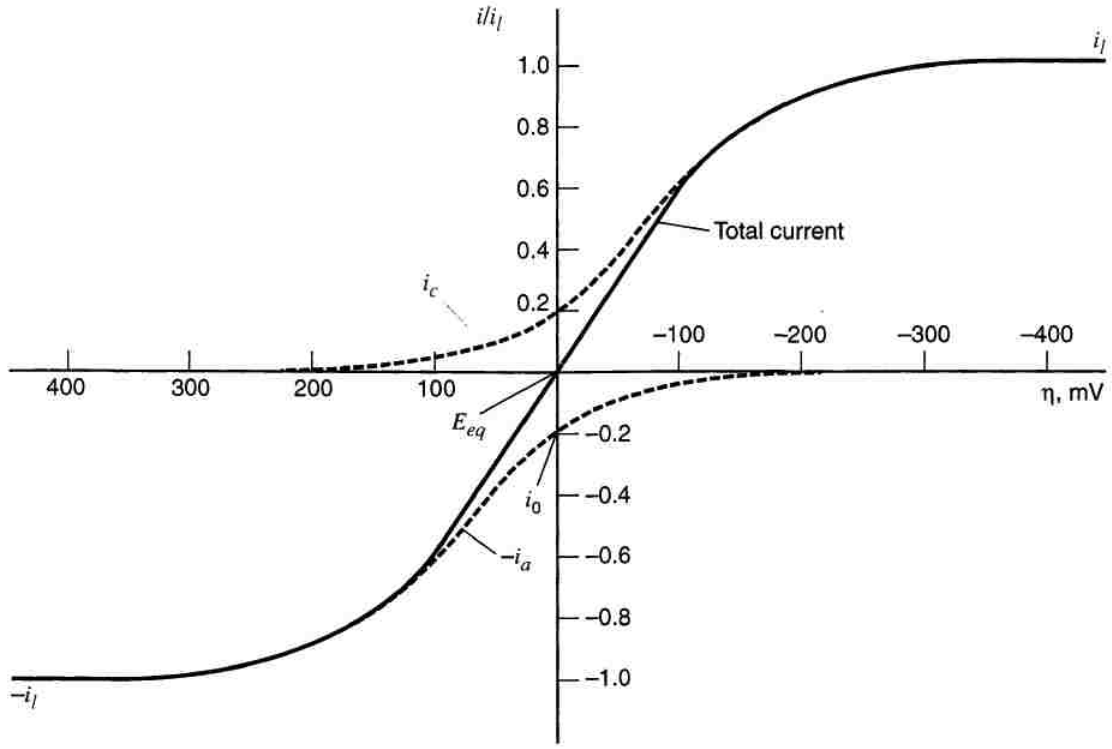

Figure 2-3. Current-overpotential curves with α = 0.5 and T = 298 K. Adapted from [19].

The solid curve from figure 2.3 represents the total current, which is the sum of the currents obtained from the forward and backward reactions, i_c and i_a respectively. At large positive or negative overpotentials the current levels off. In these level regions, the current is limited by mass transfer rather than reaction kinetics.

At large overpotentials for an anodic reaction, *i.e.* backward reaction, and no mass transfer effects, $C_O(0,t) \sim C_O$, equation (2.16) can be simplified to,

$$i = i_0[e^{((1-\alpha)nf\eta)}] \tag{2.17}$$

or

$$\eta = \frac{RT}{(1-\alpha)nF}\ln(i) - \frac{RT}{(1-\alpha)nF}\ln(i_0) \tag{2.18}$$

which is widely known as the Tafel equation.

3. Research Objectives

The development of novel electrocatalysts for the oxidation of fuels in direct alkaline fuel cells requires knowledge of the physical and chemical structure of the catalyst along with the understanding of the role of each of its components in the mechanism of reaction. There are a number of *ex situ* microscopy techniques already used to better understand the physical structure of new materials. Among these *ex situ* techniques there are electron microscopy and X-ray spectroscopy techniques such as scanning electron microscopy (SEM), transmission electron microscopy (TEM), X-ray diffraction (XRD), and X-ray photoelectron spectroscopy (XPS). The combination of all of these techniques provides a thorough insight into the structure, morphology, phase and surface compositions of new materials. However, *in situ* characterization techniques that can be applied directly to the metal/solution interface of electrochemical reactions are only starting to emerge. One of these *in situ* techniques is infrared reflection absorption spectroscopy (IRRAS). IRRAS provides information about surface intermediates and products. This information greatly benefits the development of novel electrocatalysts that could be fine-tuned for specific catalytic purposes. The combination of *ex situ* and *in situ* techniques will be exploited for the development of high performing novel electrocatalysts for the oxidation of hydrazine and ethanol for applications in direct liquid-feed alkaline fuel cells.

Part I—Direct Hydrazine Alkaline Fuel Cells

Daihatsu Motor Corporation is leading an initiative to develop a new type of direct liquid-fed fuel cell using a carbon-free fuel such as hydrazine (N_2H_4). Direct

hydrazine fuel cells will employ anionic-exchange membranes in alkaline environments permitting the use of inexpensive and abundant electrocatalysts. Moreover, the oxidation of hydrazine produces only nitrogen and water; therefore, the use of hydrazine does not contribute to greenhouse gases emissions. These features make hydrazine fuel cells a promising technology that could make fuel cell technology affordable.

The primary objectives of this work are to develop novel high-performing multifunctional electrocatalysts for the oxidation of hydrazine in direct hydrazine anionic fuel cells (DHAFCs). The development of novel electrocatalysts will be based on the study of promotion of catalysis by the alloying and/or addition of an oxide phase to the primary metal catalyst. Extensive knowledge will be gained by a number of different *ex situ* characterization techniques of synthesized materials in order to understand the role of each component in the mechanism of reaction. *In situ* spectroelectrochemical infrared studies will be performed to elucidate mechanisms of reaction and better understand the promotion of catalysis of alloyed or mixed phases.

Part II—Direct Ethanol Alkaline Fuel Cells

Similar assessment to the one established for the development of electrocatalysts for the oxidation of hydrazine will be performed on highly active elelctrocatalysts for the oxidation of ethanol for application in direct ethanol anionic fuel cells (DEAFCs). The interest in using ethanol as a fuel comes from a number of different factors. Ethanol is a biorenewable organic fuel that could be produced from biomass. Additionally, ethanol has high energy density, low toxicity, and can be stored and transported with the current infrastructure for hydrocarbon fuels. However, the limitations of using ethanol as a fuel

for fuel cells lie in the poor kinetics of its oxidation in both acidic and alkaline environments. The latter part of this work will seek to demonstrate the utility of the *in situ* infrared reflection-absorption spectroscopy on understanding the mechanism of reaction of highly active electrocatalysts for the oxidation of ethanol in an alkaline environment. Particularly, attention will be focused to the understanding of the selectivity versus performance of the ethanol oxidation reaction at different pHs.

4. Experimental Methods

4.1 Electrocatalyst Synthesis

Unsupported electrocatalysts were synthesized via the spray pyrolysis of metal nitrate precursors (Figure 4.1). Spray pyrolysis involves the atomization of an initial precursor solution with a desired chemical composition into aerosolized droplets which are typically carried by an inert gas or air through a furnace where decomposition occurs [20]. Inside the furnace the precursor solution evaporates and intraparticle reactions occur forming a catalyst precursor powder. These precursor powders are collected on a Teflon filter and post-processed either in a reducing or oxidizing environment depending on the phase formation desired. Advantages of the spray pyrolysis technique include the high purity of product powders, uniform composition, and the simplicity and facile scale-up process.

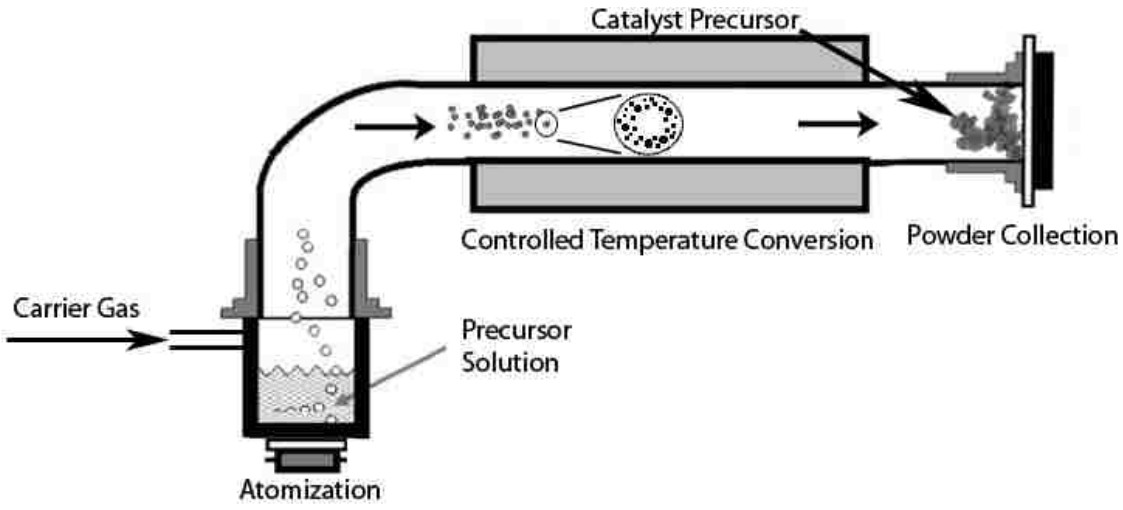

Figure 4-1. Illustration of the spray pyrolysis technique used for the synthesis of electrocatalysts.

The particle formation process involves a series of steps starting with the atomization of the solution, solvent evaporation from the surface of the droplet, solute condensation, drying, decomposition of the precipitated particles, and sintering (Figure 4.2).

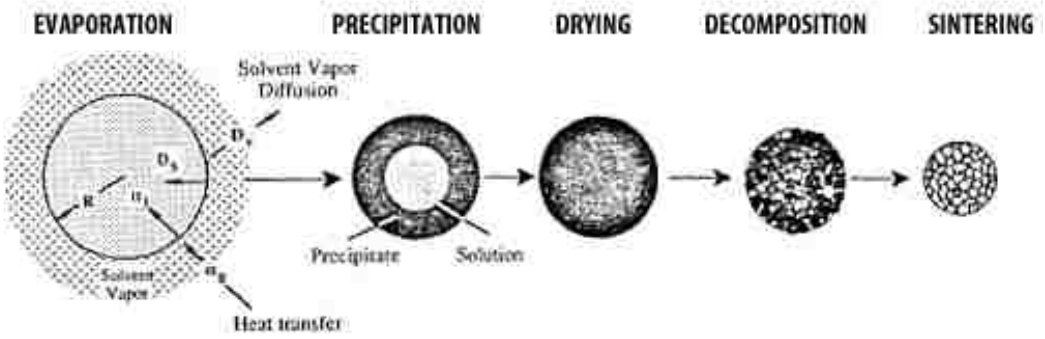

Figure 4-2. Stages of the spray pyrolysis process [21].

The characteristic of the aerosol generator determines the production rate and droplet size distribution, and thus particle size distribution, of the powders. Particular hollow particles are formed when a solute concentration gradient is created during evaporation, characteristic of precursors with low melting points. The solute precipitates first at the more highly supersaturated surface if sufficient time is not available for solute diffusion in the droplet. If a crust is formed and is not permeable to the solvent, pressure will build within the particle upon further heating and exploded particle fragments can result. Solid particle formation is promoted by high-solubility precursors, low evaporation rates, small droplet sizes, low solution concentrations, long residence times, and precursors that form permeable salts. Figure 4.3 below highlights the different particle morphologies that

could be attained from the spray pyrolysis synthesis of materials depending on precipitation conditions.

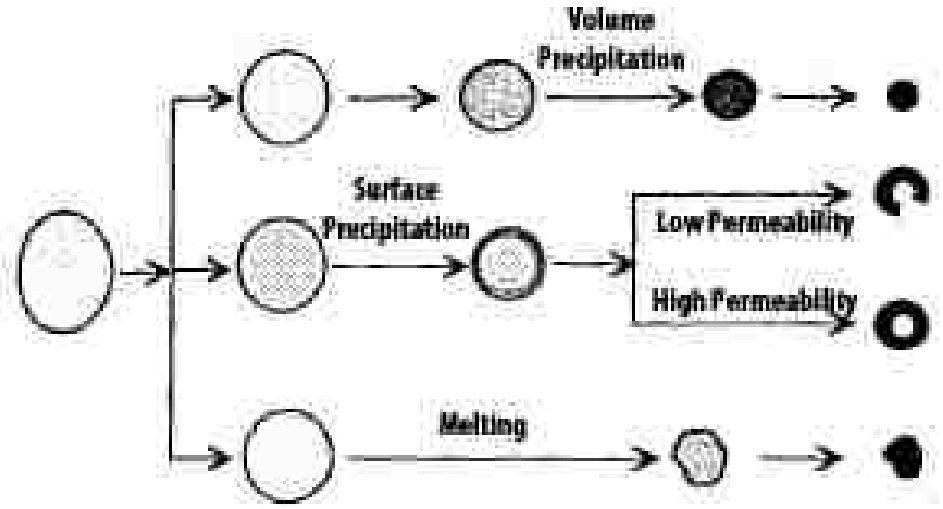

Figure 4-3. Effect of precipitation conditions on particle morphology [21].

4.2 Structural Characterization of Electrocatalysts

4.2.1 Electron Microscopy

Scanning electron microscopy (SEM) was used to provide morphological information of the synthesized catalysts. In scanning electron microscopy, an electron beam is thermoionically emitted from a tungsten filament cathode electron gun at accelerating voltages ranging from 2 to 30 keV. The emitted beam is focused by magnetic condenser lenses to a final lens where it is deflected in both x and y directions to perform a raster scan over the surface of the sample. The interaction between the electron beam and the sample causes a loss of energy by repeated random scattering and absorption within the interaction volume. These interactions cause elastic scattering of the electrons, inelastic scattering via secondary electrons, and electromagnetic radiation

emissions each of which can be detected by specialized detectors. In SEM, magnification results from the ratio of the dimensions of the raster on the sample to the raster on the display device. Therefore, magnification is controlled by the current supplied to the x and y scanning coils or the voltage supplied to the x and y deflector plates. Transmission electron microscopy (TEM) was used to obtain information about particle morphology, lattice parameters, and phase compositions. Differing from SEM, TEM uses the interaction of a beam of electrons transmitted through an ultrathin sample to form an image. TEM uses accelerated voltages ranging from 100 to 300 keV.

4.2.2 X-Ray Spectroscopy

Energy-dispersive X-ray spectroscopy (EDS) in conjunction with electron microscopy was used to determine bulk and particle composition of the synthesized materials. The principle of operation of EDS is possible due to the bombardment of the sample with high energy electrons ejecting unexcited ground state electrons from the atoms at the surface of the sample. A higher energy electron fills the resulting hole left behind by the ejected electron. The energy difference is released as an X-ray. The energy emitted by the X-rays in quantified by a detector providing information about the atomic composition of the sample.

Another X-ray technique providing valuable information about the crystal structure and phase composition of a sample is X-ray diffraction (XRD). XRD is an X-ray scattering technique that obtains information from the interference caused by the atomic planes of a crystal. This interference causes a diffraction of incoming x-rays which are collected by a detector at controlled angles. Each crystal structure of a specific

composition has a unique diffraction pattern which is used to distinguish between crystal phases present in the sample.

X-ray photoelectron spectroscopy (XPS) was used to provide information about the elemental composition, empirical formula, chemical and electronic state of the elements composing a material. XPS spectra are generated from the bombardment of a beam of X-ray to a sample while measuring the kinetic energy and number of electrons escaping from the top 1-10 nm of the sample being analyzed. An XPS spectrum is generated from the plot of the number of electrons detected versus the binding energy. Each element produces a characteristic peak of binding energy that corresponds to the electron configuration of the electrons within the atoms.

4.3 Electrochemical Characterization

Electrochemical studies were performed in a three-electrode half-cell consisting of a working electrode (glassy carbon), a counter electrode (Pt wire), and a reference electrode. The counter electrode balances the reaction being studied at the working electrode. The reference electrode is used as a standard to measure the applied potential at the working electrode.

4.3.1 Cyclic Voltammetry

In voltammetry, a controlled potential is applied to the electrochemical system while the resulting current is being monitored. The measured current is indicative of the amount of charge transfer occurring at the surface of the electrode by electrochemical processes. An important voltammetry technique that has become popular as a rapid

process to investigate new electrochemical systems is cyclic voltammetry (CV). CV is a potentiodynamic measurement technique where the potential is being swept at a constant rate, dE/dt, between an upper and a lower limit. A cyclic voltammogram is obtained by plotting the measured current as a function of the applied potential (Figure 4.4). In CV, an anodic sweep occurs when then potential is swept in the positive direction. Conversely, the cathodic sweep occurs by the reverse of the anodic sweep. The value of the current is a direct measure of the reaction rate while the behavior of the cyclic voltammogram gives information about the thermodynamic and reaction overpotentials (as described in chapter 2).

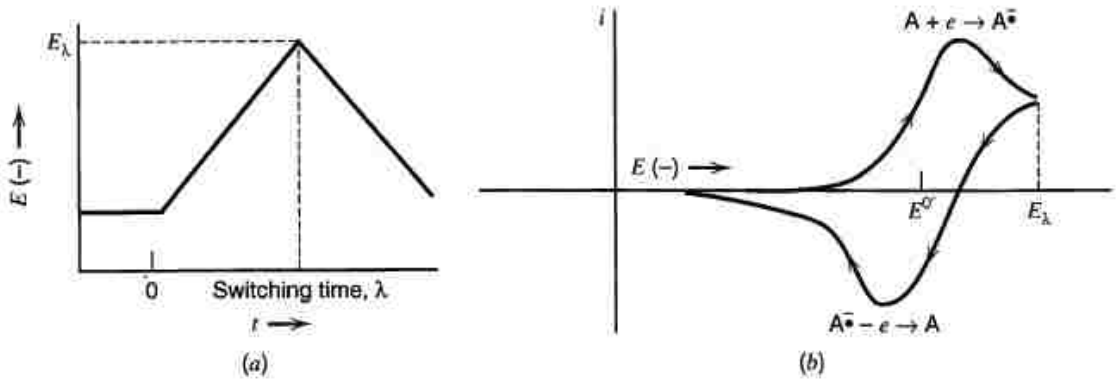

Figure 4-4. Waveform in cyclic voltammetry (a). i vs. E representation of a cyclic voltammogram (b) [19].

4.3.2 Rotating Disc Electrode (RDE)

Kinetic studies of the electrochemical reactions occurring at the surface of the electrode require a well-defined mass transport system. The rotating disk electrode (RDE) is a technique that allows electrochemical studies with limited mass transport limitations. When the electrode is rotating it pumps the electrolyte toward the surface and then

radially disperses the electrolyte back to the bulk of the solution. This pumping action prevents the extension of the concentration gradient limiting the diffusion layer to very short distances from the electrode surface.

4.3.3 In Situ Infrared Reflection-Absorption Spectroscopy (IRRAS)

A more complete assessment of reaction intermediates occurring at the electrochemical double layer of the metal/solution interface can be obtained from *in situ* vibrational characterization of adsorbed species. *in situ* infrared reflection-absorption spectroscopy (IRRAS) provides time resolved vibrational and chemical information which can help determine important information about the electrochemical reaction such as rate-limiting steps, final products, and kinetic parameters based on the understanding of electron transfer reaction occurring.

Part I.

Direct Hydrazine Fuel Cells

5. Direct Hydrazine Alkaline Fuel Cells

5.1 Introduction

The development of emerging fuel cell technologies with the focus on improving air quality by reducing greenhouse emissions has seen promising results from nontraditional nitrogen-containing fuels such as hydrazine (N_2H_4). Hydrazine is a carbon-free fuel of particular interest since their consumption yields N_2 as the main product [22-24]. The utilization of hydrazine as a fuel has a number of advantages: starting from the products obtained from its decomposition (nitrogen and water), high energy density (5.26 kW·h/kg) [25], and the possibility of using the current infrastructure for the transportation and storage of hydrazine hydrate as a fuel. An industrial process is already in place for the production of hydrazine. This industrial process is the Raschig process.

5.1.1 The Raschig Process

The Raschig process was first discovered in 1907. The main chemical reactions of the Raschig process involve three steps:

$$NaOH + Cl_2 \rightarrow NaOCl + HCl \quad (5.1)$$

$$NH_3 + NaOCl \rightarrow NH_2Cl + NaOH \quad (5.2)$$

$$NH_2Cl + NH_3 + NaOH \rightarrow N_2H_4 \cdot H_2O + NaCl \quad (5.3)$$

In the Raschig process NaOCl is produced by feeding chlorine into a 30% aqueous caustic solution in a circulating reactor system. The reaction temperature is kept below 30°C and the NaOH concentration is kept below 1 g/L to prevent decomposition and

chlorate formation. Hydrazine hydrate synthesis involves the partial oxidation of ammonia using the formed sodium hypochlorite in the presence of gelatin or glue at temperatures around 160-180°C and elevated pressures (Equation 5.3). The reaction liquor contains 1% hydrazine hydrate and 4% NaCl. Ammonia is condensed and recycled. The product is concentrated by fractional distillation to obtain a higher concentration of hydrazine hydrate.

5.2 Development of Hydrazine Fuel Cells

The utilization of hydrazine for direct hydrazine fuel cells (DHFCs) in an alkaline electrolyte has been suggested since the 1960s [26, 27]. Since then, a number of different companies such as Chloride Electric Storage Company, Shell Research Company, Allis Chalmers Manufacturing Company, Electrochimica Corporation and Monsanto Company have researched the possible development and applications of hydrazine fuel cells. The most noteworthy progress was carried through by Allis Chalmers Manufacturing Company. Allis Chalmers developed a 3 kW hydrazine fuel cell with a maximum power density of 250 mW/cm^2 which was used to power a golf cart.

However, a report on the toxicity of hydrazine published in 1977 hindered further research on DHFCs as it reported that hydrazine is both highly toxic and mutagenic [28]. Daihatsu Motor Co. has addressed the toxicity concerns of using hydrazine by developing a detoxification technique in which hydrazine is safely stored as hydrazone ($>C=N-NH_2$) or hydrazide ($-CO-NH-NH_2$) (Figure 5.1) [29]. Hydrazine hydrate is then released by the addition of a solvent when required.

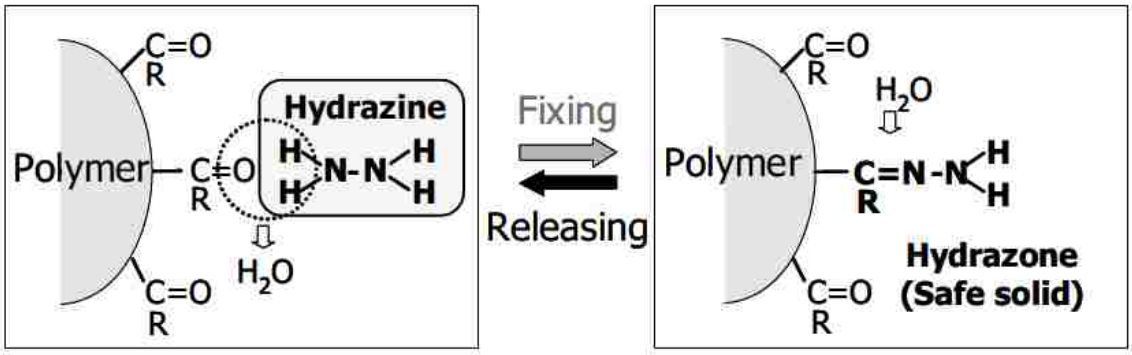

Figure 5-1. Schematic of safe storage of hydrazine.

As introduced in chapter 1, alkaline fuel cells utilizing anion-exchange membranes (AEMs) possess a number of advantages over PEMFCs which require corrosive acidic electrolytes and expensive noble metal catalysts. The less-corrosive alkaline electrolyte permits the use of non-noble transition metals as catalysts, which are more abundant and less expensive, thus, making fuel cells more affordable. Moreover, improvement in the oxidation and reduction kinetics has been reported for alkaline environments over acidic environments [10, 11]. Lastly, DHFCs do not suffer from CO poisoning, a main drawback for PEMFCs using Pt-based catalysts [24, 27, 30].

The theoretical cell voltage for a direct hydrazine fuel cell is 1.56 V, higher than that obtained from a hydrogen/oxygen fuel cell. The electrochemical half-reactions of the DHFC are as follows:

Anode Reaction:

$$N_2H_4 + 4OH^- \rightarrow N_2 + 4H_2O + 4e^- \quad E^0 = -0.33 \text{ V (vs. RHE)} \qquad (5.1)$$

Cathode Reaction:

$$O_2 + 2H_2O + 4e- \rightarrow 4OH- \qquad E^0 = 1.23 \text{ V (vs. RHE)} \qquad (5.2)$$

Overall Cell Reaction:

$$N_2H_4 + O_2 \rightarrow N_2 + 2H_2O \qquad E^0 = 1.56 \text{ V (vs. RHE)} \qquad (5.3)$$

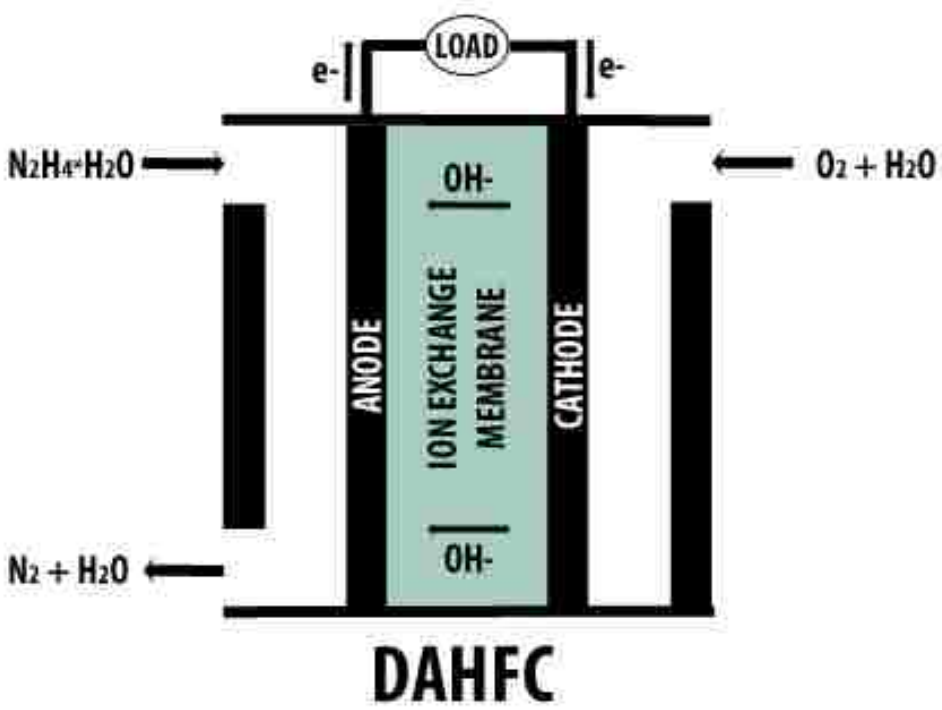

Figure 5-2. Schematic of a direct hydrazine anionic fuel cell.

Development of new direct hydrazine anionic-exchange membrane fuel cells (DHAFCs) has been led by the Daihatsu Motor Corporation [8, 29, 31-37]. Research related to the development of new anionic-exchange membranes for hydrazine fuel cells has been reported by several groups. Tanaka *et al.* reported results of an anionic conductive block poly(arylene ether) membrane containing quaternized ammonia-substituted fluorine groups. These membranes showed considerably high hydroxide ion conductivities of about 144 mS/cm at 80°C. Durability studies reported the retention of high conductivities in water at 80°C for 5000 h. When tested in a noble metal-free direct hydrazine fuel cell, the obtained maximum power density was 297 mW/cm^2 achieving a

current density of 826 mA/cm^2. Another development in anionic-exchange membranes for hydrazine fuel cells was reported by Zhang *et al.* [38]. Zhang reported a polytetrafluoroethylene (PTFE) based membrane with good conductivities of 49 mS/cm at room temperature as well as good stability and strength. Therefore, promising results have already been reported in relation to the development of new anionic-exchange membranes targeted for direct hydrazine fuel cells.

A number of different catalysts have been reported for the anodic oxidation of hydrazine. Among these catalysts are Pt [26, 30, 31, 39-41], Pd [42-45], Ag [46-48], Au [48], Hg [30, 48, 49], Ni [32, 42, 50], and Co [32, 44]. Daihatsu Motor Co. has reported electrochemical activity from a number of different metal catalysts [32, 33]. Various polycrystalline metal electrodes (Ni, Co, Fe, Cu, Ag, Au) were compared to Pt which is often the electrocatalysts of choice for the oxidation of small molecules. Lower onset potentials from Ni and Co were observed when compared to Pt. Furthermore, higher power densities from fuel cell testing were also observed from both Ni and Co when compared to Pt. However, Co exhibited a higher rate of hydrazine decomposition to form ammonia compared to Ni [51]. Consequently, Ni was determined to be the most suitable anode catalyst.

It has been extensively reported that the performance of catalysts can be significantly improved by alloying or addition of secondary phases to promote the rate of catalysis. Therefore, it is the goal of this dissertation to conduct research related to the enhancement of active Ni catalysts for the oxidation of hydrazine in alkaline media by studying the promotion of catalysis by alloying or combining with an oxide phase. Chapter 6 will be devoted to the study of nickel alloying with zinc, an electron dense and

oxophilic metal that could cause an intrinsic effect improving the catalytic performance of nickel. Chapter 7 will be focused on the discussion of the promotion effect caused by the synergism created by the presence of an oxide phase of lanthanum and nickel.

6. $Ni_{1-x}Zn_x$ Electrocatalysts: Promotion by an Alloyed Phase

6.1 Introduction

In addition to the advantages provided by the use of alkaline media, the utilization of binary and/or ternary metal catalytic systems have been known to provide stability, increased reactivity and functionality over single-metal catalytic systems [52, 53]. Ye *et al.* reported on the electrocatalytic activity of a heterogeneous Pd-Ni/C composite compared to that of its single-constituents. The study found better performance from the Pd-Ni/C catalyst than both Pd/C and Ni/C for the electrooxidation of hydrazine [42]. Nevertheless, the non-homogeneity of the Pd-Ni/C catalyst makes it difficult to deduce any mechanism since in addition to the synergy of the Pd-Ni catalyst different reactions could also happen at each of its counterparts. Moreover, Sakamoto *et al.* reported the catalytic activity of unsupported Ni_xCo_y catalysts. They found $Ni_{50}Co_{50}$ exhibited higher mass activity than the compositions $Ni_{75}Co_{25}$ and $Ni_{25}Co_{75}$ as well as their pure components Ni and Co [35]. Sanabria-Chinchilla *et al.* performed a study on the reaction pathways of these highly active Ni-Co alloys. Differentially pumped electrochemical mass spectroscopy (DEMS) studies suggest competing faradic (electrochemical) and nonfaradic (chemical) reaction pathways [34].

The enhanced activity provided by intermetallic catalytic systems has been attributed to two different phenomena: bifunctional and electronic effects. A bifunctional effect is attributed to the synergistic contribution of each of the constituents of the catalyst towards a particular reaction mechanism. A ligand or electronic effect refers to the altering of the electronic properties of an atom promoted by its neighbouring atoms.

This chapter focuses on the study of the effect on the catalytic activity and reaction pathways of aerosol-derived unsupported $Ni_{1-x}Zn_x$ catalysts. We hypothesize that the alloying of an oxophilic and electron-dense atom such as Zn with Ni could provide a Lewis-base type of catalyst capable of producing a ligand effect increasing its reactivity and functionality. Additionally, Zn atoms could also offer a synergistic type of effect by providing oxygen species near the surface of the electrode at lower potentials to oxidize and remove adsorbed intermediates.

6.2 Experimental Methods

6.2.1 Electrocatalyst Synthesis

Synthesis of unsupported $Ni_{1-x}Zn_x$ electrocatalysts was achieved using spray pyrolysis (see Fig. 1). Ni, Zn, and Co nitrates (99.999%, Sigma-Aldrich Co.) were dissolved in 10% HNO_3 to a final concentration of 5 wt% to specific stoichiometric ratios. The dissolved bimetallic solution was ultrasonically atomized and pyrolyzed using a quartz tube (1 in. OD, 24 in. long) in a furnace operating at 500°C using N_2 (1 L/min) as the carrier gas. Pyrolyzed particles were collected and air dried on a Teflon filter. Alloys and solid solutions were formed by reduction of the oxide precursor powders under flowing 5% H_2 in N_2 at 400°C. Ni and three different stoichiometric compositions of Ni and Zn nitrates were synthesized: $Ni_{0.87}Zn_{0.13}$, $Ni_{0.50}Zn_{0.50}$, and $Ni_{0.33}Zn_{0.67}$, representing different phases of the $Ni_{1-x}Zn_x$ system as discussed later.

6.2.2 Structural and Compositional Characterization

After reduction, phase purity, morphology, and composition of synthesized

powders were characterized using X-Ray Diffraction (XRD), Scanning Electron Microscopy (SEM), High-Resolution Transmission Electron Microscopy (HRTEM), and Energy Dispersion Spectroscopy (EDS). X-ray powder diffraction spectra were recorded using Scintag Pad V diffractometer with DataScan 4 software (MDI, Inc.) for system automation and data collection. Cu Kα radiation (40 kV, 35 mA) was used with a Bicron Scintillation detector (with a pyrolitic graphite curved crystal monochromator). Data sets were analyzed with Jade 9.5 Software (MDI, Inc.) using the ICDD (International Center for Diffraction Data) PDF2 database (rev. 2004) for phase identification.

Scanning electron microscopy (SEM) was performed on a Hitachi S-5200, with a resolution of 0.5 nm at 30 kV and 1.7 nm at 1 kV, equipped with PGT EDS. Transmission electron microscopy (TEM) was performed on a JEOL 2010F FASTEM field emission gun scanning transmission electron microscope equipped with Oxford EDS. The probe size was 1.0 nm, and accelerating voltage was 200kV.

6.2.3 Electrochemical Characterization

An aqueous suspension (4 mg/mL in THF:1-Propanol [1:4]) of each powder was prepared and sonicated to disperse the powder in solution. A 2 wt% anion ionomer solution (A3, Tokuyama Corp.) was added to the suspension to act as a binder. 3 µl aliquots of the aqueous suspension were deposited onto a glassy carbon rotating-disc electrode (RDE) and allowed to air dry. Electrochemical measurements were conducted in a jacketed electrochemical cell containing 1 M KOH at 60 °C.

Hydrazine hydrate (24-26% in H_2O, Sigma-Aldrich Co.) was dissolved to 5 wt% in 1 M KOH to perform linear sweep voltammetry (LSV) measurements at a scan rate of 20 mV/s. A Pt-coil was used as a counter electrode and a Hg/HgO electrode (XR440,

Radiometer Analytical SAS) was used as reference electrode. Before each experiment, the electrolyte solution was deoxygenated by bubbling Ar gas for at least 15 minutes prior to taking any measurements.

6.2.4 Infrared Studies

In situ Infrared Reflection Adsorption Spectroscopy (IRRAS) experiments were performed at room temperature with a Nicolet 6700 FT-IR spectrometer equipped with a Mercury Cadmium Telluride (MCT) detector cooled with liquid nitrogen. Experimental setup is described previously [54]. For each spectrum, 128 interferograms were added together at a resolution of 8 cm^{-1} with unpolarized light. Absorbance units of the spectra are defined as $A = -\log(R/R_0)$, where R and R_0 represent reflected IR intensities corresponding to the sample and reference single beam spectrum, respectively. Thus, a positive peak in the resulting spectrum indicates a production of species, while a negative peak indicates consumption or decrease in concentration of a species compared to the reference spectrum. The reference spectrum was collected at -0.42 V (vs. RHE) with 0.1 M hydrazine and 1 M KOH. A thin layer of ink was pipetted onto a polished glassy carbon electrode with a diameter of 5 mm. A ZnSe hemisphere was used as the IR window, and the working electrode was pressed against the window, creating a thin solution layer with a thickness of a few micrometers. The incident angle of the IR radiation passing through the ZnSe window was 36° [55]. Argon was used to purge the electrolyte while dry air was used to purge the spectrometer and chamber, reducing the spectral interference from ambient CO_2 and water vapor.

6.3 Results and Discussion

6.3.1 Electrocatalyst Synthesis and Characterization

Unsupported $Ni_{1-x}Zn_x$ electrocatalysts were synthesized through the pyrolysis of aerosolized precursors (Figure 6.1).

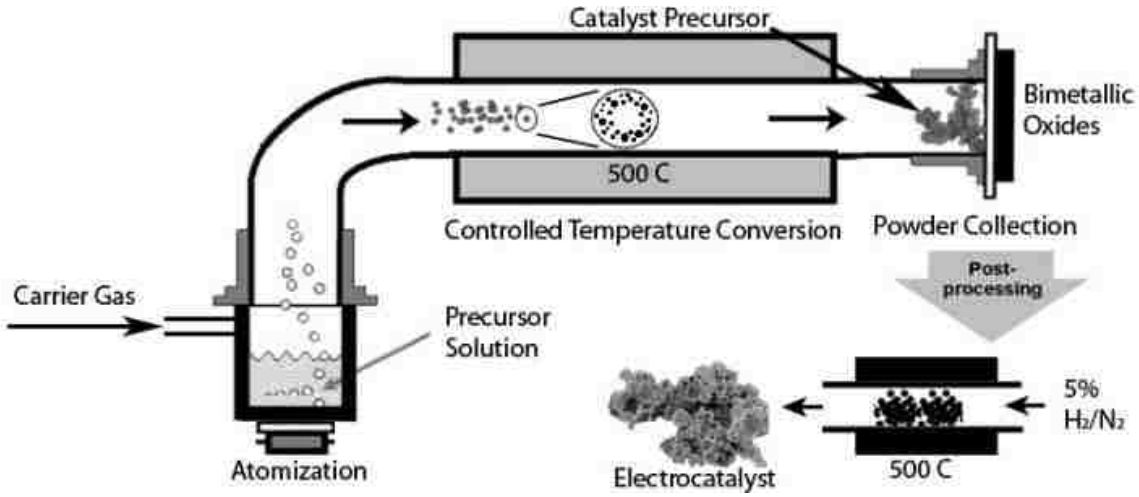

Figure 6-1. Schematic of the spray pyrolysis process for the synthesis of $Ni_{1-x}Zn_x$ electrocatalysts.

Spray pyrolysis allows for thermally driven processes to occur in aerosolized droplets of the precursor while the dispersion of such micron-sized liquid droplets is being carried in a laminar flow through a controlled temperature hot-wall reactor/furnace. A wide variety of materials including metals, their alloys, oxides, carbides, nitrides, and a broad spectrum of composites including one or more of those classes have been exemplified by spray pyrolysis [20, 21, 56-59]. Spray pyrolysis offers the advantage of generating particles with uniform compositions due to the unique control of particle formation within droplets ensuring complete retention of the precursor stoichiometry.

The characteristic morphology of synthesized electrocatalysts post-pyrolysis and

post-reduction were analyzed using scanning electron microscopy (SEM) (Figure 6.2, a and b).

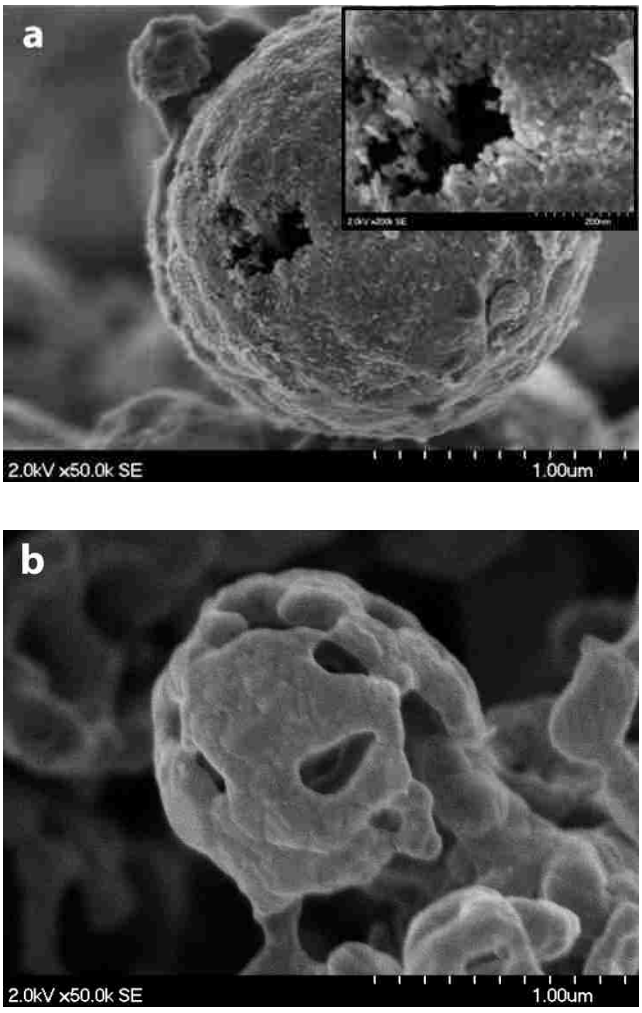

Figure 6-2. SEM micrographs of α-$Ni_{0.87}Zn_{0.13}$. a) after the pyrolysis process (inset: hollow spherical micron-size particles are composed of 5-10 nm agglomerates) and b) after the post-reduction process.

Figure 6.2a illustrates bimetallic oxide precursor particles obtained post-pyrolysis for the α-$Ni_{0.87}Zn_{0.13}$ catalyst. During pyrolysis, 5-10 nm particles agglomerate within each droplet to form hollow micron-size spherical particles (inset in Figure 6.2a). Hollow particles can be formed due to surface precipitation. As the salts precipitate at the outer

layer of the aerosolized particles, the permittivity of the gases produced through the molten salts is reduced causing the internal pressure, and volume, of the particle to increase and create hollow particles [20, 21]. As these hollow particles are reduced at 400°C in a flowing 5% H_2 environment, sintering of the nanoparticles occurs while retaining the micron-size spherical morphology observed for the bimetallic oxide precursor (Figure 6.2b). For miscible metals as is the case for the α-$Ni_{0.87}Zn_{0.13}$ illustrated in Figure 6.2b, a network of particles with a sponge-like morphology is observed. BET-surface area of synthesized catalysts ranged from 5-7 m^2/g.

X-ray diffraction was used to confirm crystal structures and phase purities of the synthesized $Ni_{1-x}Zn_x$ electrocatalysts.

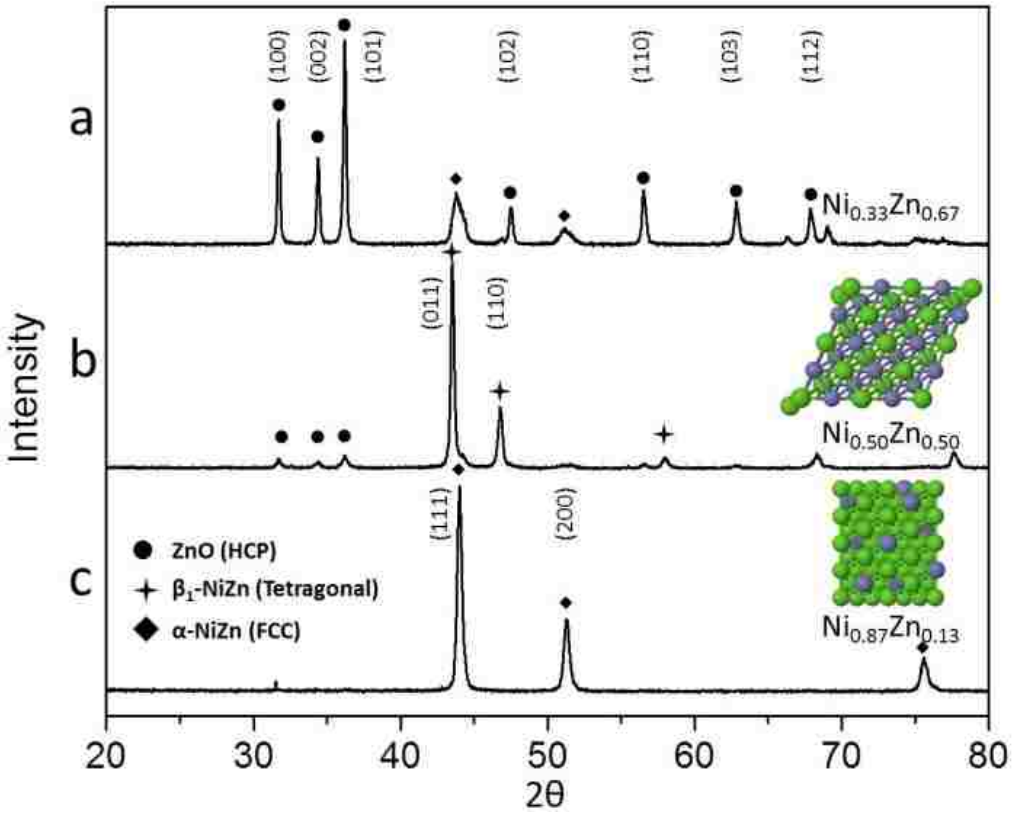

Figure 6-3. XRD spectra of $Ni_{1-x}Zn_x$ electrocatalysts. a. Predominantly ZnO at x = 0.67 at% Zn. b. FC tetragonal β1-NiZn. c. FC cubic α-NiZn.

XRD spectra for the three synthesized $Ni_{1-x}Zn_x$ electrocatalysts are shown in figure 6.3. The three compositions of $Ni_{1-x}Zn_x$ catalysts, $Ni_{0.87}Zn_{0.13}$, $Ni_{0.50}Zn_{0.50}$, and $Ni_{0.33}Zn_{0.67}$, belong to different regions of the Ni-Zn phase diagram [60].

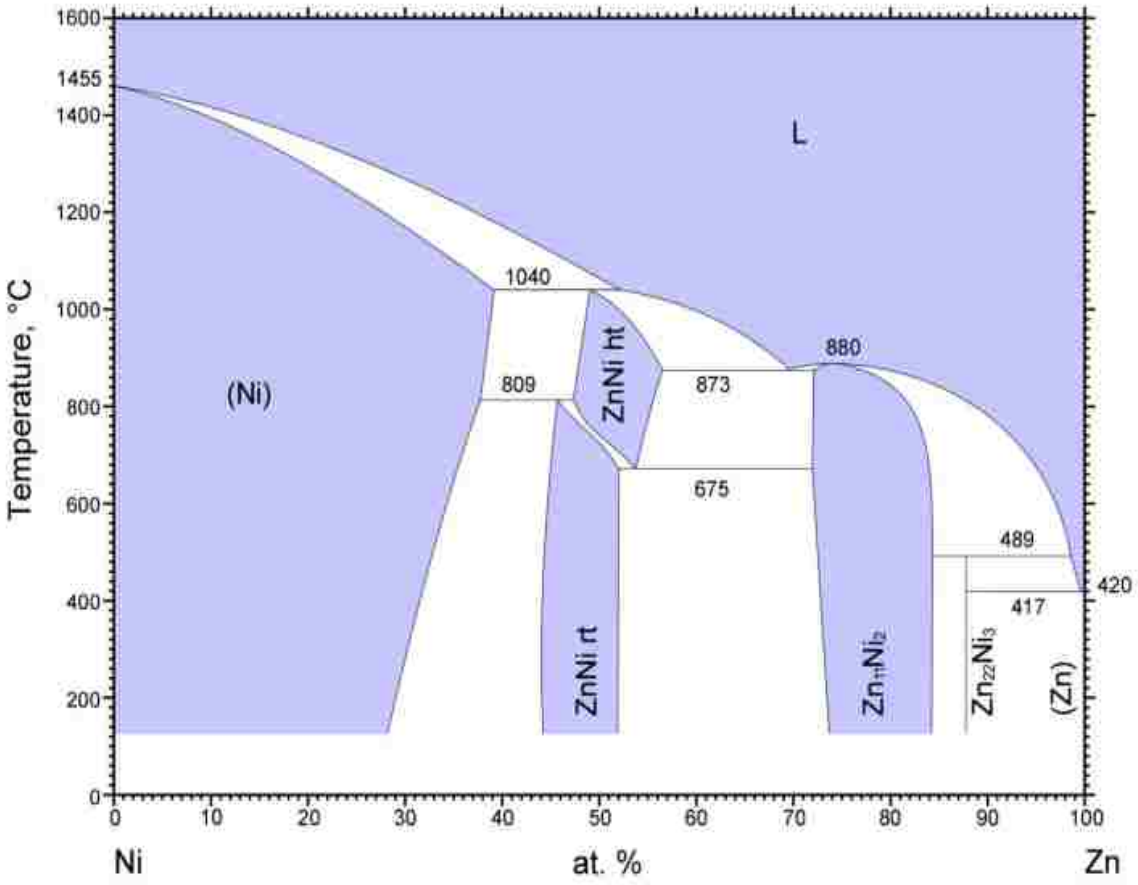

Figure 6-4. Ni-Zn phase diagram [60].

The α-NiZn phase is formed by the random substitution of Ni atoms with Zn atoms while retaining the Ni FCC crystal structure. Although the crystal structure is retained, lattice spacing changes due to the difference in atomic size which causes a shift on the XRD spectrum. This α-NiZn phase exists for ranges from 0 to 28-37 at% Zn. The α-$Ni_{0.87}Zn_{0.13}$ catalyst shows characteristic FCC peaks at 2θ angles 44.0°, 51.3°, and 75.5° which correspond to the (111), (200), and (220) planes, respectively (Figure 6.3c). At ranges from 44-52 at% Zn, a highly ordered intermetallic NiZn structure is formed. This β_1-

phase structure consists of a FC tetragonal superlattice with Ni and Zn atoms occupying the alternate (001) planes [61]. Characteristic peaks of this β_1-phase are observed in the XRD spectrum of the β_1-$Ni_{0.50}Zn_{0.50}$ catalyst (Figure 6.3b). Peaks observed at 2θ angles 43.5° and 46.8° correspond to planes (011) and (110), respectively, and have already been reported as the peaks responsible for the $L1_0$ structure of the intermetallic β_1-NiZn phase [62]. The spectrum of the β_1-$Ni_{0.50}Zn_{0.50}$ catalyst also shows minimal traces of ZnO with peaks at 32°, 34.5°, and 36°. This ZnO phase is predominant in the spectrum for the $Ni_{0.33}Zn_{0.67}$ catalyst (Figure 6.3a). According to the NiZn phase diagram, a composition of $Ni_{0.33}Zn_{0.67}$ should yield a mixture of the β_1 structure plus a cubic (γ-phase) structure. However, neither of these phases is present. The post-treatment reduction process yielded a more thermodynamically stable ZnO phase and some α-NiZn particles for concentration of Zn higher than 50 at%.

Prior to the reduction post-treatment, spray pyrolyzed materials consist of oxide phases. Figure 6.5 below shows the XRD spectrum of $Ni_{0.87}Zn_{0.13}$ after the pyrolysis process. The main phase present is NiO with characteristic 2θ angles at 37.0°, 43.1°, 62.5°, 75.1°, and 79.1° which correspond to planes (111), (200), (220), (311), and (222) respectively. Reflections appearing at 2θ angles between 10° and 35° correspond to intermediate hydroxide phases, $Zn(NO_3)_2 \cdot 2Zn(OH)_2$ and $Ni(NO_3)_2 \cdot Ni(OH)_2 \cdot 2H_2O$.

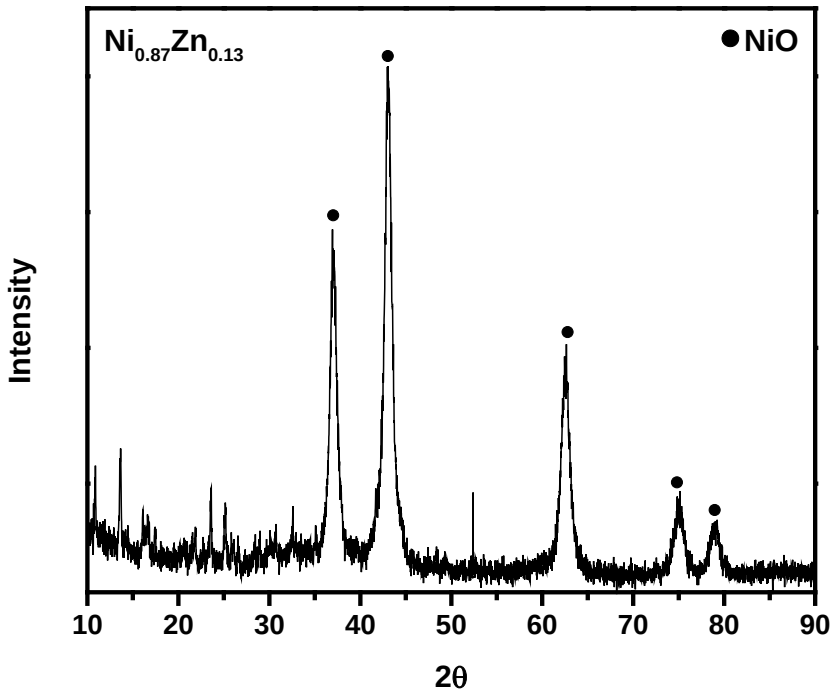

Figure 6-5. XRD spectrum of $Ni_{0.87}Zn_{0.13}$ prior to the post-treatment process.

High-Resolution Transmission Electron Microscopy (HRTEM) micrographs of α-$Ni_{0.87}Zn_{0.13}$ are shown in figure 6.6. The overall morphology of the aerosol-derived catalysts is illustrated in Figure 6.6a. Crystallinity of these catalysts is illustrated in figure 6.6b. Lattice spacings of 0.20 nm and 0.18 nm measured from the FFT diffraction pattern shown in the inset of figure 6.6b corresponds to the (111) and (200) planes, respectively. Thus, confirming the FCC structure observed from the XRD spectrum.

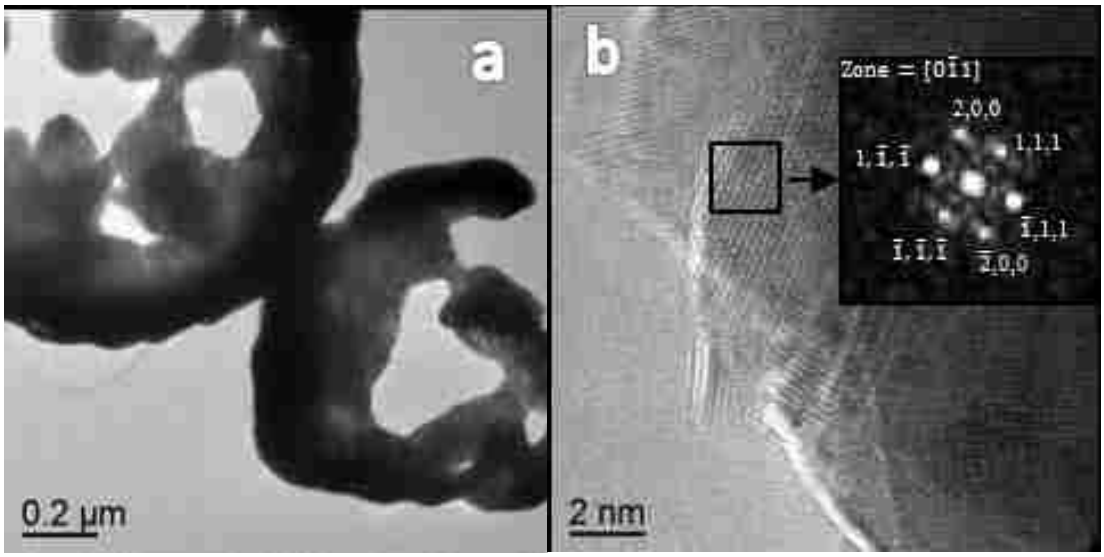

Figure 6-6. HRTEM micrographs of α-$Ni_{0.87}Zn_{0.13}$ catalyst. Catalyst is formed of crystalline agglomerates ranging from 20-60 nm in size.

6.3.2 Electrochemical Performance

Once the understanding of the material structure and phase purity of the synthesized electrocatalysts was established, their performance as anode catalysts for the oxidation of hydrazine was examined in a 1 M KOH electrolyte.

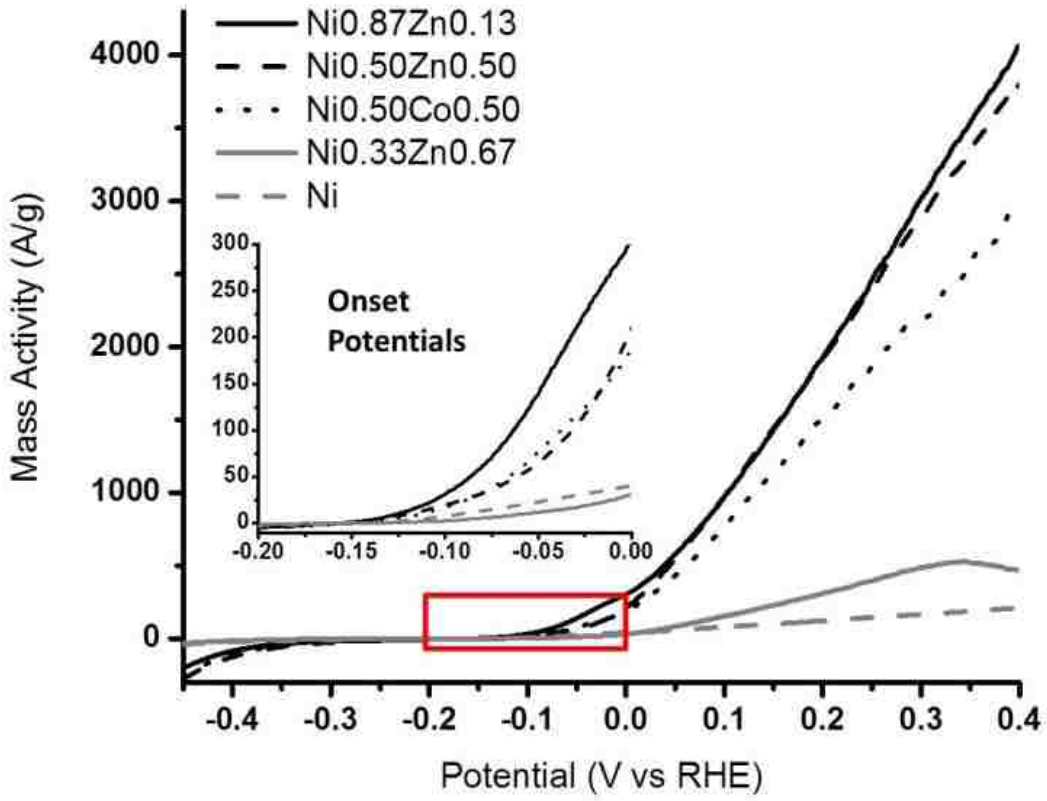

Figure 6-7. LSV of aerosol-derived $Ni_{1-x}Zn_x$ catalysts compared to $Ni_{0.50}Co_{0.50}$ and Ni. Reaction conditions: 20 mV/s in 1M KOH and 5% hydrazine at 60 °C and 1600 rpm.

Figure 6.7 compares the mass activity of $Ni_{0.87}Zn_{0.13}$, $Ni_{0.50}Zn_{0.50}$, $Ni_{0.33}Zn_{0.67}$, $Ni_{0.50}Co_{0.50}$, and Ni catalysts. All electrocatalysts tested were synthesized using spray pyrolysis. The $Ni_{0.50}Co_{0.50}$ catalyst was included in this comparison since it has been reported that Ni-Co catalysts are highly active for the oxidation of hydrazine in alkaline media. Sakamoto *et al.* reported on the activity of unsupported NiCo catalysts synthesized by the liquid reduction process [35]. The study finds $Ni_{0.50}Co_{0.50}$ as the most active catalyst with a maximum mass activity of 171.2 A/g at 0.05 V (vs. RHE) and an onset potential of -0.21 V when compared to $Ni_{0.25}Co_{0.75}$, $Ni_{0.75}Co_{0.25}$, Ni, and Co. Sanabria-Chinchilla *et al.* also reported on the catalytic activity and mechanism of a $Ni_{0.60}Co_{0.40}$/C catalyst [34]. Maximum mass activity was found to be 1300 $A/g_{total\ metal}$ at

0.22 V (vs. RHE) followed by a decrease in mass activity due to the passivation of the electrocatalyts. The onset potential is observed at about -0.15 V and has a mass activity of 480 $A/g_{total\ metal}$ at 0.05 V (vs. RHE). The $Ni_{0.60}Co_{0.40}/C$ catalyst was synthesized by an impregnation/freeze-drying procedure where metal precursors were supported on high-surface-area carbons and then converted to the zerovalent state in a reductive H_2 atmosphere followed by thermal annealing. A direct comparison between the results obtained for the spray pyrolyzed materials reported in this study with the results reported by Sanabria-Chinchilla *et al.* cannot be determined due to the lack of understanding of the role played by the difference in surface areas and the carbon support. However, a similar performance was observed from the spray pyrolyzed unsupported $Ni_{0.50}Co_{0.50}$ catalyst near the onset potential (Figure 6.7). The onset potential of the electrooxidation of hydrazine starts near -0.15 V and has a mass activity of 440 A/g at 0.05 V. No passivation for the potential range swept was observed and a maximum activity of 3000 A/g at 0.4 V (vs. RHE) was reached. This phenomenon could be due to the *in situ* reduction of the electrocatalyst surface by hydrazine or one of its intermediates. Nevertheless, α-$Ni_{0.87}Zn_{0.13}$ and β_1-$Ni_{0.50}Zn_{0.50}$ catalysts exhibit higher mass activity than the $Ni_{0.50}Co_{0.50}$ catalyst, with the α-$Ni_{0.87}Zn_{0.13}$ catalyst showing a better activity near the onset potential. Onset potentials are similar for all catalysts, starting at around -0.15 V (vs. RHE), but mass activity is about 1000 A/g higher than $Ni_{0.50}Co_{0.50}$ at 0.4 V. As reported before [32, 33], Ni and Co are both catalytically active for the oxidation of hydrazine in alkaline media; thus, the high mass activity observed for Ni-Co bimetallic catalysts could be due to a co-catalytic mechanism in which active sites are found in both constituents. On the other hand, Zn is nearly inactive for the oxidation of hydrazine; thus,

high mass activity observed for α-$Ni_{0.87}Zn_{0.13}$ and β_1-$Ni_{0.50}Zn_{0.50}$ catalysts must be due to a bifunctional and/or electronic effect of the Zn on the active Ni catalyst. A DFT evaluation showed that the interaction between hydrazine and surfaces depends strongly on the composition. Hydrazine is predicted to decompose on Ni(111) to form two NH_2 fragments with a combined binding energy of E_B = 1.5 eV. In contrast, hydrazine remains molecular on β_1-$Ni_{0.50}Zn_{0.50}$ with the lone pair pointing toward Ni and filling the Ni 3d shell. The binding energy of hydrazine to Ni in the presence of Zn is much lower, E_B = 0.8 eV. These results indicate that the contribution of Zn is to stabilize molecular hydrazine and reduce its binding energy such that it can be oxidized in an alkaline environment. Further studies using *in situ* IRRAS were performed to understand the mechanism of oxidation on these highly active catalysts.

6.3.3 In Situ IRRAS Experiments

In situ infrared reflection absorbance spectroscopy (IRRAS) studies were conducted to identify intermediates and understand the mechanism of reaction of the highly active α-$Ni_{0.87}Zn_{0.13}$. Figure 6.8 shows the infrared spectra taken at 25 °C and 0 rpm from the potential range of -0.4 V to 0.4 V (vs. RHE). All spectra shown in Figure 6.8 are compared to a reference spectrum taken at the starting potential. Therefore, a trough represents the disappearance of species, while a peak represents a new kind of species being formed. Following the adsorption of hydrazine, the spectrum at -0.39 V shows troughs at 3225, 1646, and 801 cm^{-1}. These bands belong to the N-H and O-H species; therefore, these troughs represent a decrease of these species. At the same potential, peaks at 2775, 1900, and 1080 cm^{-1} appear. The peak at 2775 cm^{-1} signifies the formation of an amine salt $–NH_2^{+2}$ possibly due to the partial dehydrogenation of

hydrazine as it adsorbs. Furthermore, the peak at 1080 cm^{-1} corresponds to the N-N stretch of the adsorbed hydrazine species as reported by Gland *et al.* [63] and confirmed by infrared hydrazine studies reported by Giguere and Liu [64] along with Tipton *et al.* [65]. The most important finding from the infrared spectra experiments is the species formed at 1900 cm^{-1}. The vibrational frequency at 1900 cm^{-1} corresponds to the Ni-H stretch [66]. This finding in correlation with the decrease of NH and OH species observed can be attributed to two different steps of the mechanism of reaction. In the first step, hydrazine hydrate adsorbs to the Ni active site losing the water molecule (Equation 6.4); in the second step, hydrazine is partially dehydrogenated by neighbouring Ni atoms forming the adsorbed $N_2H_2^{+2}$ salt (Equation 6.5).

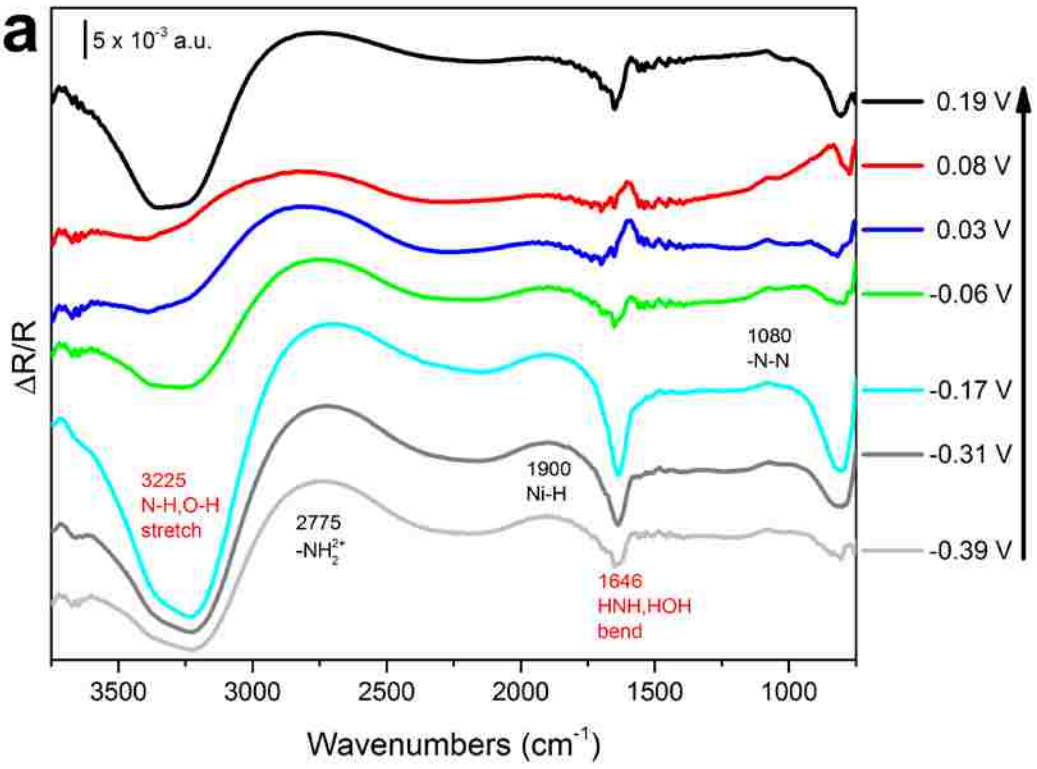

Figure 6-8. IRRAS spectra of the oxidation of hydrazine on α-$Ni_{0.87}Zn_{0.13}$.

Table 6-1. IRRAS band assignments for the electrooxidation of hydrazine on α-$Ni_{0.87}Zn_{0.13}$.

Wavenumber (cm^{-1})	Assignment
3225	N-H, O-H stretch
2775	$-NH_2^{+2}$
1900	Ni-H stretch [a]
1646, 1587	HNH, HOH bend
1080	-N-N stretch (in hydrazine)[b]
801, 840	OH, NH deformations
[a] ref: [66]. [b] refs: [63-65].	

Figure 6.9 below displays the absorbance ratio of the Ni-H species (1900 cm^{-1}) normalized to the N-N species (1080 cm^{-1}).

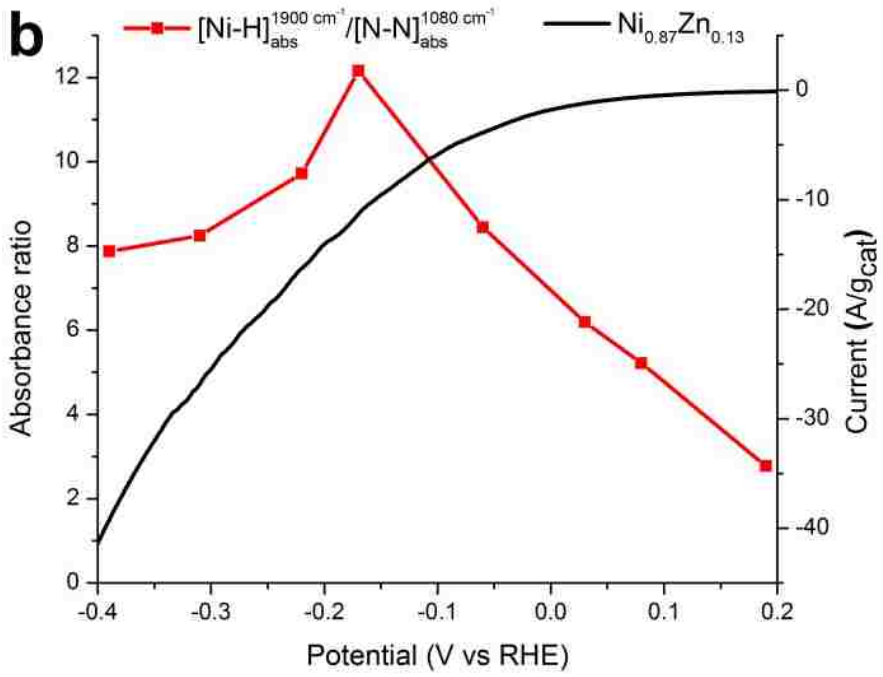

Figure 6-9. Graph of the Ni-H vibrational frequencies normalized to the N-N frequencies and the corresponding linear sweep voltammogram (LSV) of the hydrazine oxidation reaction. Reaction conditions: 1 mV/s, 1M KOH, and 0.1M hydrazine at 25°C and 0 rpm.

The $[Ni\text{-}H]_{abs}/[N\text{-}N]_{abs}$ ratio increases as the potential is increased, reaching a maximum at -0.17 V vs. RHE. At higher potentials, 0.03 V and 0.08 V, hydroxide ions begin to appear near the surface of the electrode as can be observed from the widening of the peak at 2775 cm^{-1} and the emergence of the peak at 840 cm^{-1} in figure 6.8. As the onset potential is reached, hydroxide ions near the surface of the electrode oxidize the adsorbed hydrogen species forming water (Equation 6.6). This reaction causes the decrease of the $[Ni\text{-}H]_{abs}/[N\text{-}N]_{abs}$ ratio observed in Figure 6.9 and the disappearance of the Ni-H peak at 1900 cm^{-1} detected from the IRRAS spectra at 0.19 V (Figure 6.8). In summary, the mechanism of reaction can be described as follows,

$$N_2H_4 \cdot H_2O \rightarrow N_2H_{4ads} + H_2O \tag{6.4}$$

$$N_2H_{4ads} \rightarrow 2H_{ads} + {N_2H_2}^{+2}{}_{ads} \tag{6.5}$$

$$2H_{ads} + {N_2H_2}^{+}{}_{ads} + 4OH^- \rightarrow N_2 + 4H_2O + 4e^- \tag{6.6}$$

Kodera *et al.* had suggested a similar mechanism for the oxidation of hydrazine on a Pt electrode in alkaline media [41]. However, evidence that the ${N_2H_2}^{+2}{}_{ads}$ species were stable was lacking and therefore chose a different mechanism of dehydrogenation forming N_2H_{2ads} species instead. Evidence that those charged species prevail until these species are removed at the moment of electrooxidation is shown here. Another important aspect of this mechanism is the ability of the $\alpha\text{-}Ni_{0.87}Zn_{0.13}$ catalyst to partially dehydrogenate hydrazine. This ability was not observed on the Ni-Co catalysts reported by Sanabria-Chinchilla *et al.* [56] nor is it observed for the oxidation mechanism on pure Ni (Figure 6.10).

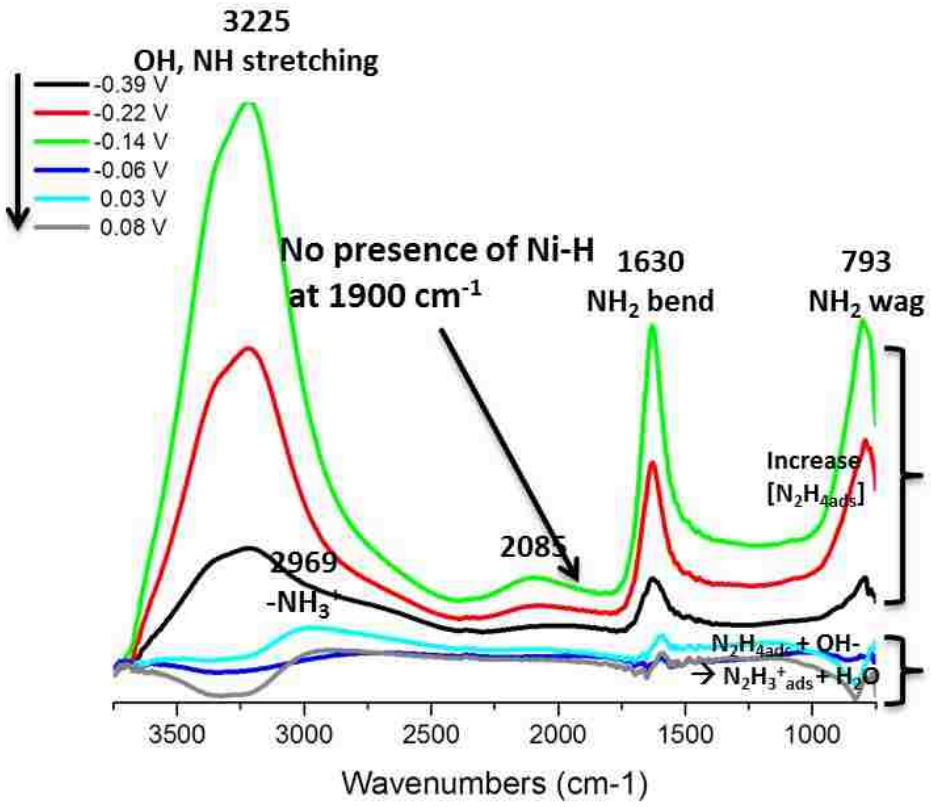

Figure 6-10. IRRAS spectra for the oxidation of hydrazine on Ni.

Ni-H formation could help in preventing passivation of the catalyst and extend the durability of the catalyst. Thus, we conclude that Zn alloying with Ni intrinsically modifies the catalytic activity of Ni by creating a Lewis base catalyst in which it enhances the ability for Ni to act as electron-pair donor capable of inducing hydrazine adsorption and partial dehydrogenation.

6.4 Conclusions

We have reported in this study the synthesis and characterization of highly active unsupported $Ni_{1-x}Zn_x$ electrocatalysts synthesized through spray pyrolysis, which proved to be a versatile and facile technique that is easily scalable. XRD analysis showed that at low at% of Zn phase pure α-NiZn can be obtained. At atomic concentrations of Zn higher

than 50% a more thermodynamically stable ZnO phase is predominant. LSV results showed high mass activity from both α-$Ni_{0.87}Zn_{0.13}$ and β_1-$Ni_{0.50}Zn_{0.50}$, with the α-$Ni_{0.87}Zn_{0.13}$ showing a better performance near the onset potential (-0.15 V vs. RHE, at 60 °C). *In situ* IRRAS studies conducted for the α-$Ni_{0.87}Zn_{0.13}$ catalyst indicated a pathway of hydrazine oxidation in which the α-$Ni_{0.87}Zn_{0.13}$ catalyst partially dehydrogenates hydrazine forming Ni-H complexes which could prevent the passivation of α-$Ni_{0.87}Zn_{0.13}$ catalysts. Consequently, Ni alloying with Zn intrinsically modified the catalytic activity of Ni creating a Lewis base catalyst in which Ni is able to act as an electron-pair donor capable of inducing the adsorption and partial dehydrogenation of hydrazine, making aerosol-derived α-$Ni_{0.87}Zn_{0.13}$ a viable anode catalyst for applications in direct hydrazine anionic fuel cells for a number of different applications.

7. $Ni_{1-x}La_x$ Electrocatalysts: Promotion by an Oxide Phase

7.1 Introduction

The promotion effect of metal oxides on the electrochemical activity of several catalysts has been reported for numerous reaction systems [54, 67, 68]. However, there are only a few reports on the promotion effect of oxides for the electrooxidation of hydrazine [69, 70]. Karim-Nezad *et al.* reported an improved performance in the kinetics of the hydrazine oxidation by a copper hydroxide-modified copper electrode compared to bare copper electrodes [69]. Rare-earth metal oxides have been widely used in high temperature fuel cell. Recently, the use of rare-earth metal oxides to function as either catalysts or co-catalysts has been suggested for low-temperature fuel cells [71]. From the viewpoint of material resources, transition and rare-earth metals are abundant and less costly than noble metal catalysts, so their use could potentially reduce the cost of fuel cells. CeO_2 is one of the most commonly used rare-earth metal oxide for the promotion of catalysis on platinum electrocatalysts. Pt-CeO_2/C electrocatalysts have shown improved performance and stability over traditional Pt/C for the oxidation of alcohols [72, 73].

As reported before, Ni-based electrocatalysts have shown best performance for the hydrazine oxidation when compared to Pt [32, 34-36, 42, 50]. The studies reported in this chapter aim to investigate the promotion effect observed from La_2O_3 and $La(OH)_3$ phases on the electrocatalytic activity of Ni for the oxidation of hydrazine hydrate in an alkaline electrolyte. Thorough physical and electrochemical characterization was performed along with *in situ* infrared studies to understand the mechanism of oxidation.

Lastly, the fuel cell performance using Ni/$La(OH)_3$ electrocatalysts was reported in a direct hydrazine anionic fuel cell.

7.2 Experimental Methods

7.2.1 Electrocatalyst Synthesis

Synthesis of unsupported $Ni_{1-x}La_x$ electrocatalysts was achieved using spray pyrolysis (Figure 7.1). Ni and La nitrates (99.999%, Alfa-Aesar) were dissolved in 10% HNO_3 to a final concentration of 5 wt% to specific stoichiometric ratios. The dissolved solution was ultrasonically atomized and pyrolyzed using a quartz tube in a furnace operating at 500°C using N_2 (1 L/min) as the carrier gas. Pyrolyzed particles were collected and air dried on a Teflon filter. Post processing of collected catalysts was performed in a reducing environment using 5% H_2/95% N_2 gas at 500°C.

7.2.2 Structural and Compositional Characterization

X-ray powder diffraction spectra were recorded using Scintag Pad V diffractometer with DataScan 4 software (MDI, Inc.) for system automation and data collection. Cu Kα radiation (40 kV, 35 mA) was used with a Bicron Scintillation detector (with a pyrolitic graphite curved crystal monochromator). Data sets were analyzed with Jade 9.5 Software (MDI, Inc.) using the ICDD (International Center for Diffraction Data) PDF2 database (rev. 2004) for phase identification.

SEM was performed on a FEI Quanta 3D Field Emission Gun SEM equipped with EDAX Apollo 40 EDS system. HRTEM were performed on a JEOL 2010F FASTEM field emission gun scanning transmission electron microscope equipped with

EDS. Probe size for high resolution work was 0.2 nm, 1.0 nm for analytical work, and accelerating voltage was 200 kV.

X-ray photoelectron spectroscopy (XPS) was performed on a Kratos Axis Ultra X-ray photoelectron spectrometer. Spectra were recorded under the operating pressure of around 2×10^{-9} Torr using a monochromatic Al Kα source operating at 300 W with charge compensation. Broad-range spectra were acquired at 80 eV pass energy while high resolution spectra were acquired at a pass energy of 20 eV. Ambient Pressure-XPS experiments were carried out at ISIS, the catalysis beamline of the Fritz Haber Institute at the 3rd generation synchrotron BESSY II (Helmholtz-Zentrum Berlin). The powder samples were pressed into self-supporting ~1 mm disks thick that were mounted in the in situ heated holder and exposed to gases at up to 0.25 mbar. Spectra were generated using incident photon energies of 120 eV above monitored B.E. energy window and adjusted for beamline photon flux variations. Quantification of XPS was performed using CasaXPS software. Curve-fitting was carried out using individual peaks with 70% Gaussian/30% Lorentzian line shape and widths and binding energies were constrained to best experimental fittings of reference Ni and La_2O_3 materials.

7.2.3 Electrochemical Characterization

An aqueous suspension (4 mg/mL in THF:1-Propanol [1:4]) of each powder was prepared and sonicated to disperse the powder in solution. A 2 wt% anion ionomer solution (A3, Tokuyama Corp.) was added to the suspension to act as a binder. 3 µl aliquots of the aqueous suspension were deposited onto a glassy carbon rotating-disc

electrode (RDE) and allowed to air dry. Electrochemical measurements were conducted in a jacketed electrochemical cell containing 1 M KOH at 60 °C.

Hydrazine hydrate (24-26% in H2O, Sigma-Aldrich Co.) was dissolved to 5 wt% in 1 M KOH to perform linear sweep voltammetry (LSV) measurements at a scan rate of 20 mV/s. A Pt-coil was used as a counter electrode and a Hg/HgO electrode (XR440, Radiometer Analytical SAS) was used as reference electrode. Before each experiment, the electrolyte solution was deoxygenated by bubbling Ar gas for at least 15 minutes prior to taking any measurements.

7.2.4 Infrared Studies

In situ Infrared Reflection Adsorption Spectroscopy (IRRAS) experiments were performed at room temperature with a Nicolet 6700 FT-IR spectrometer equipped with a Mercury Cadmium Telluride (MCT) detector cooled with liquid nitrogen. Experimental setup is described previously [54]. For each spectrum, 128 interferograms were added together at a resolution of 8 cm^{-1} with unpolarized light. Absorbance units of the spectra are defined as $A = -\log(R/R_0)$, where R and R_0 represent reflected IR intensities corresponding to the sample and reference single beam spectrum, respectively. Thus, a positive peak in the resulting spectrum indicates a production of species, while a negative peak indicates consumption or decrease in concentration of a species compared to the reference spectrum. The reference spectrum was collected at -0.42 V vs. RHE with 0.1 M hydrazine and 1 M KOH. A thin layer of ink was pipetted onto a polished glassy carbon electrode with a diameter of 5 mm. A ZnSe hemisphere was used as the IR window, and the working electrode was pressed against the window, creating a thin solution layer with

a thickness of a few micrometers. The incident angle of the IR radiation passing through the ZnSe window was 36° [55]. Argon was used to purge the electrolyte while dry air was used to purge the spectrometer and chamber, reducing the spectral interference from ambient CO_2 and water vapor.

7.2.5 DHFC Evaluation

100 mg of the catalyst was combined with 0.96 ml of isopropanol, 0.24 ml of THF and 0.2 ml of a 5 wt% anionic ionomer solution. The ink was then sonicated for 5 min. Following sonication, the mixture was better dispersed using ZrO2 beads (d=2.0mm, Nikkato Corp.) for 15 min. The prepared ink was directly sprayed onto an anionic electrolyte membrane (A201, Tokuyama). Co-PPY-C (PPY: polypyrrole, Hokko Chemical Industry) cathode catalyst was formed into an electrode using a similar method to that for the anode. The membrane was then pressed for 5min at room temperature to bond between catalyst layers and a membrane. The membrane was immersed in 1.0M KOH solution for 8 h.

The prepared MEA was inserted in a single cell to measure the cell performance using a round shaped working electrode area of 1 cm^2. The fuel of 1.0M KOH + 20% $N_2H_4 \bullet H_2O$ was supplied to the anode at flow rate of 2 ml/min, and oxygen gas humidified at 50°C was supplied to the cathode at the flow rate of 500 mL/min. The anode had a serpentine flow-field design while the cathode was comb-shaped. The cell temperature was controlled at 80°C. The operating pressures on both anode and cathode sides were 20 kPa.

7.3 Results and Discussion

7.3.1 Electrocatalyst Synthesis and Characterization

Four different compositions of $Ni_{1-x}La_x$ electrocatalysts (x=0.05, 0.10, 0.15, 0.17) were synthesized by the pyrolysis of aerosolized precursors (Figure 7.1). Spray pyrolysis ensures complete retention of the precursor stoichiometry by generating aerosolized droplets with uniform composition due to the unique control of particle formation within droplets.

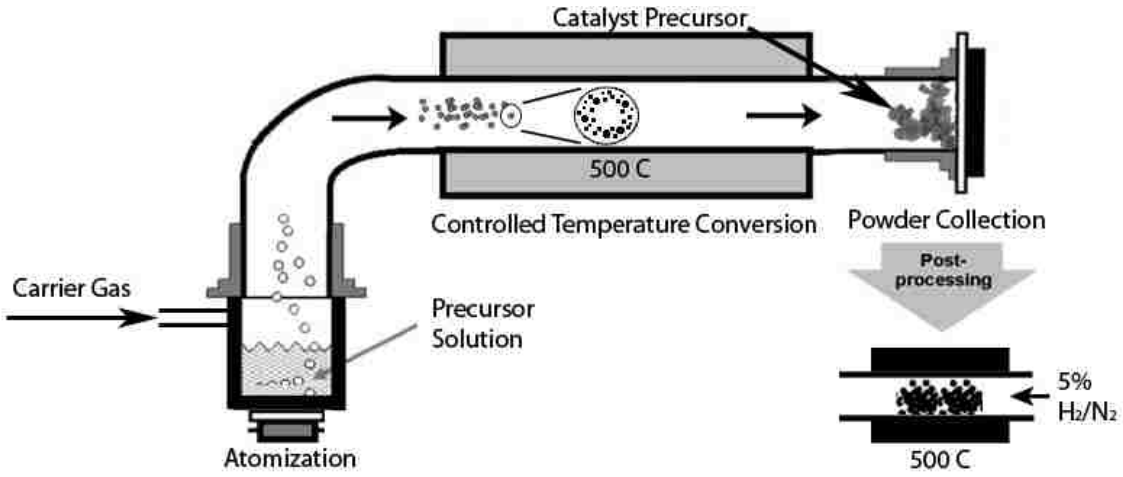

Figure 7-1. Schematic of spray pyrolysis technique for the synthesis of $Ni_{1-x}La_x$ electrocatalysts.

Spray pyrolysis of $Ni_{1-x}La_x$ nitrate precursors generated hollow spherical particles (Figure 7.2). Synthesized catalysts are hollow due to the surface precipitation of the metal precursors. As the salts precipitate at the outer layer of the aerosolized particles, the permittivity of the gases produced through the molten salts is reduced causing the internal pressure, and volume, of the particle to increase and create hollow particles [20, 21].

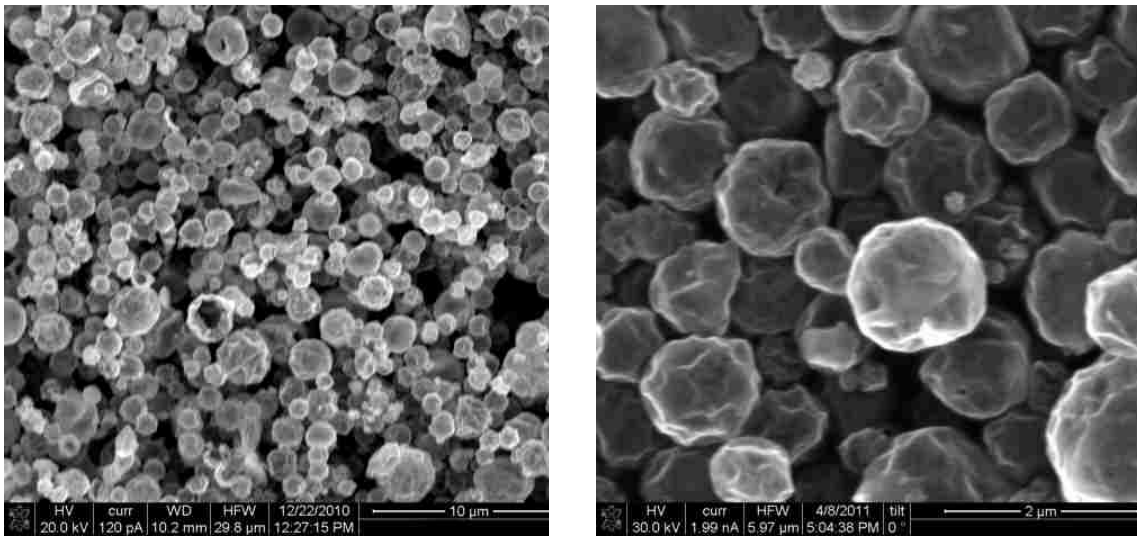

Figure 7-2. SEM micrographs of synthesized $Ni_{0.90}La_{0.10}$ (left) and $Ni_{0.95}La_{0.05}$ (right).

Further information about the phase composition of the electrocatalysts was obtained from X-ray diffraction. Figure 7.3 below shows the XRD spectra of the four synthesized $Ni_{1-x}La_x$ electrocatalysts (x=0.05, 0.10, 0.15, and 0.17). The predominant phase for catalysts $Ni_{0.95}La_{0.05}$, $Ni_{0.90}La_{0.10}$, and $Ni_{0.85}La_{0.15}$ is the FCC Ni phase with reflections at 2θ angles 44.5°, 51.8°, and 76.3° which correspond to planes (111), (200), and (220) respectively. The reflections at 26.0° and 30.0° for the $Ni_{0.95}La_{0.05}$ catalyst corresponds to the (100) and (011) planes of the hexagonal β-La_2O_3 phase. A different La phase was observed for the $Ni_{0.90}La_{0.10}$ catalyst. 2θ angles at 15.6°, 27.9°, 39.5°, 48.7°, and 55.5° correspond to the planes (100), (101), (201), (211), and (112) of the hexagonal $La(OH)_3$ phase. It is not unexpected to see a hydroxide forming from an oxide phase for lanthanum, as it has been reported that lanthanum oxide reacts with water vapor at room temperature to form lanthanum hydroxide [74, 75]. For the $Ni_{0.85}La_{0.15}$ catalyst, lanthanum formed the cubic α–La_2O_3 phase. 2θ angles for the α–La_2O_3 phase appear at 26.8°, 31.0°, and 52.6° for planes (222), (400), and (622). While the $Ni_{0.95}La_{0.05}$,

$Ni_{0.90}La_{0.10}$, and $Ni_{0.85}La_{0.15}$ electrocatalysts are composed of predominantly Ni and a lanthanum oxide phase, the electrocatalyst $Ni_{0.83}La_{0.17}$ is largely composed of two oxide phases, NiO and β-La_2O_3, in addition to the FCC Ni phase.

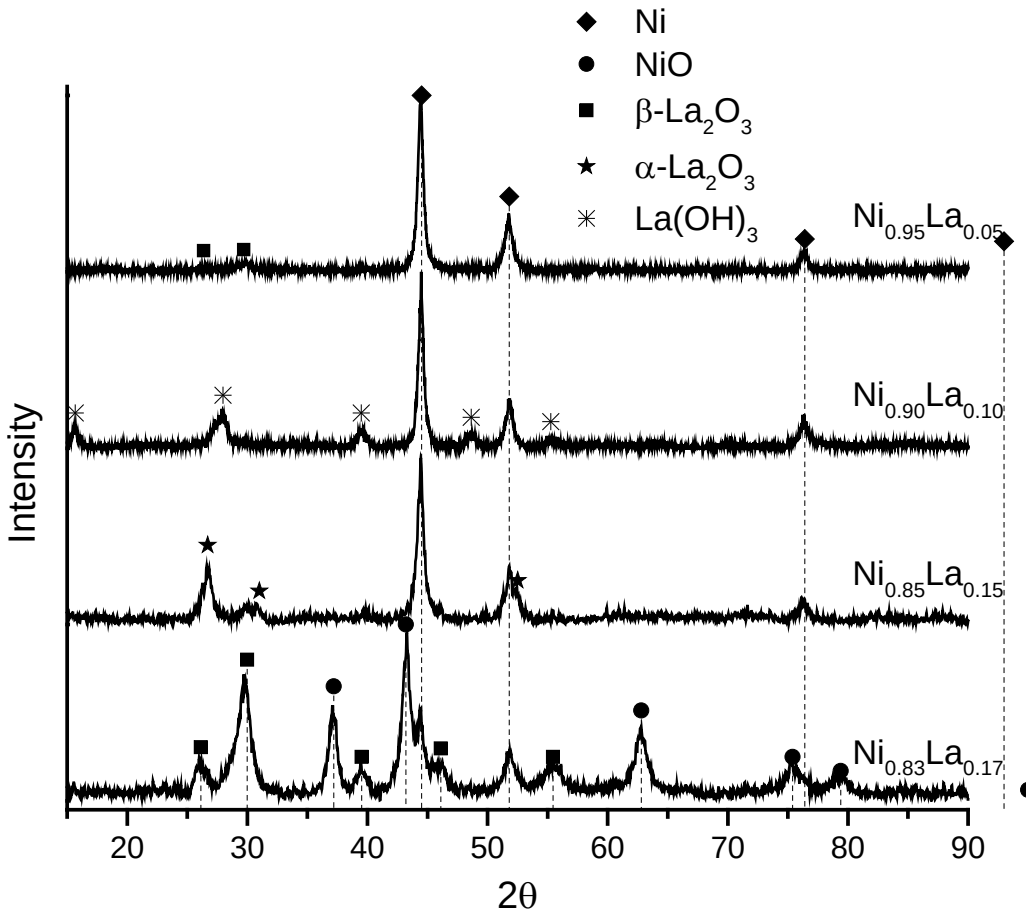

Figure 7-3. XRD Spectra of $Ni_{1-x}La_x$ electrocatalysts.

Further confirmation of the lanthanum hydroxide phase in the $Ni_{0.90}La_{0.10}$ catalyst was obtained using HRTEM (Figure 7.4). FFT analysis of two different areas within the HRTEM micrograph revealed the presence of both $La(OH)_3$ (HCP) as well as Ni (FCC). Lattice spacings of 0.33 nm, 0.32 nm, and 0.19 nm were measured from the FFT diffraction pattern shown in the inset on the left of figure 7.4. These lattice spacings

correspond to the planes (110), (101), and (211), respectively. A similar analysis of a particle towards the right of the micrograph reveals lattice spacings of 0.22 nm and 0.17 nm, which correspond to the (111) and (200) of the Ni FCC structure.

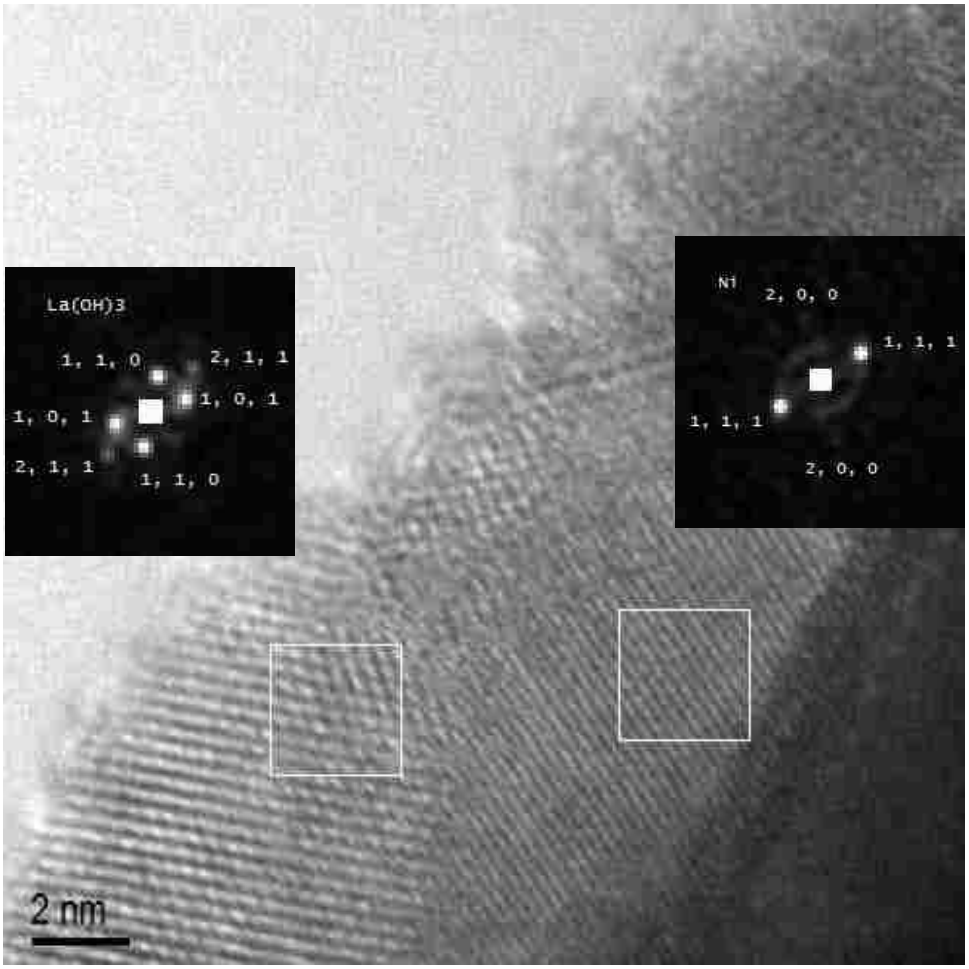

Figure 7-4. HRTEM micrograph of $Ni_{0.90}La_{0.10}$ showing both $La(OH)_3$ and Ni phases.

7.3.2 Electrochemical characterization

The promotion effect of the oxide phases on the Ni catalyst was assessed for the electrochemical oxidation of hydrazine hydrate in a 1 M KOH electrolyte. Figure 7.5 below shows the current density performance observed for all $Ni_{1-x}La_x$ electrocatalysts.

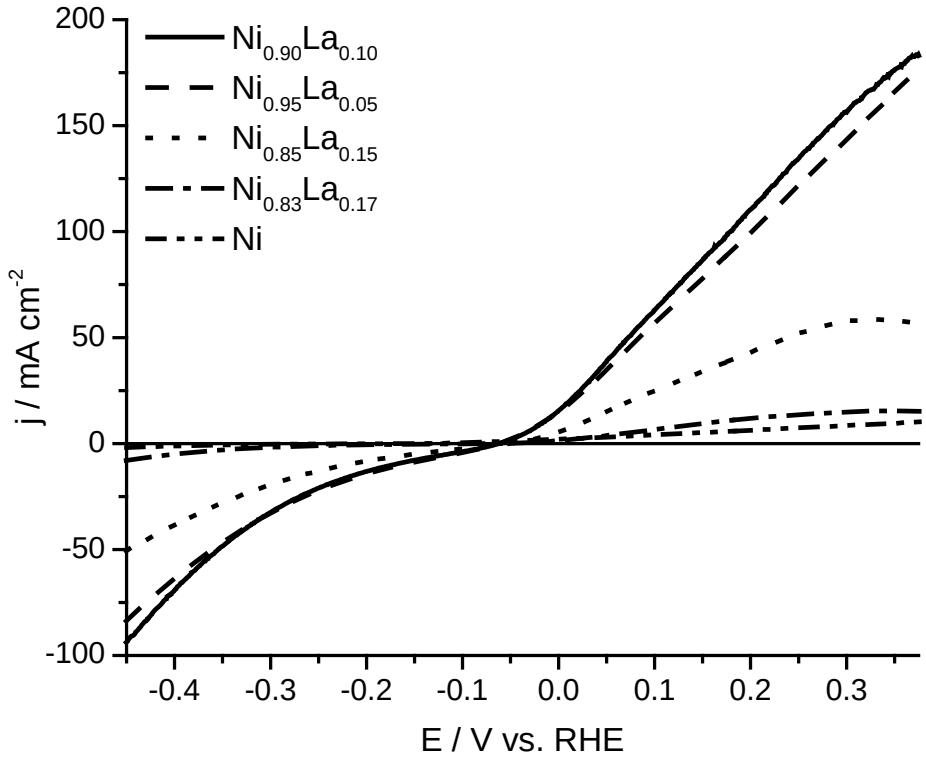

Figure 7-5. Linear Sweep Voltammetry of aerosol-derived $Ni_{1-x}La_x$ electrocatalysts. Reaction conditions: 20 mV/s, 1M KOH, 5% hydrazine hydrate, 60°C, and 1600rpm.

Onset potentials for all electrocatalysts are similar, starting at -0.06 V vs. RHE. However, the observed electrochemical activity was higher for both $Ni_{0.95}La_{0.05}$ and $Ni_{0.90}La_{0.10}$, with the $Ni_{0.90}La_{0.10}$ catalyst showing a slight higher current density. $Ni_{0.85}La_{0.15}$ also showed an improved performance over pure Ni although the activity was not as high as it was for the previously mentioned catalysts. No improvement was observed from the $Ni_{0.83}La_{0.17}$ due to the large amount of oxide phases present. The active phase for the oxidation of hydrazine is the FCC Ni. However, most of the Ni in the $Ni_{0.83}La_{0.17}$ catalyst is present in the NiO phase, thus the activity of the $Ni_{0.83}La_{0.17}$ catalyst comes from only the reduced form of Ni promoted by the oxide phases. The

enhanced performance observed from the electrocatalysts with the lowest concentration of lanthanum oxide phase demonstrates a promotion effect of the lanthanum oxide phase on the Ni catalysts activity. Maximum performance was observed for La at% no higher than 10%. Further evaluation of the higher performing $Ni_{0.90}La_{0.10}$ and $Ni_{0.95}La_{0.05}$ electrocatalysts will be discussed using XPS, DFT, and *in situ* infrared studies to understand the role of the lanthanum oxide phase.

7.3.3 XPS Characterization

Information about the chemical and elemental surface composition of the $Ni_{0.95}La_{0.05}$ catalyst was obtained from X-ray photoelectron spectroscopy (XPS) studies. Figures 7.6 and 7.7 below shows the XPS spectra for the La 3d and O 1s regions of the $Ni_{0.95}La_{0.05}$ sample taken under vacuum and in water. Figure 7.6a shows the characteristic binding energies in the La 3d region for the core levels and satellite peaks representing the La_2O_3 phase. These energies are tabulated below (Table 7.1). However, when the sample is exposed to H_2O the intensities of the satellite peaks change (Figure 7.6b). The increase in the intensities of the satellites is due to the decrease in electronegativity of binding. Therefore, as the electronegativity of the anions composing the ligand cluster around the La^{3+} decreases the intensity of the satellites increases until they become more intense then the parent peaks. This may indicate OH^- binding to La which is also confirmed by O 1s signal in figure 7.7.

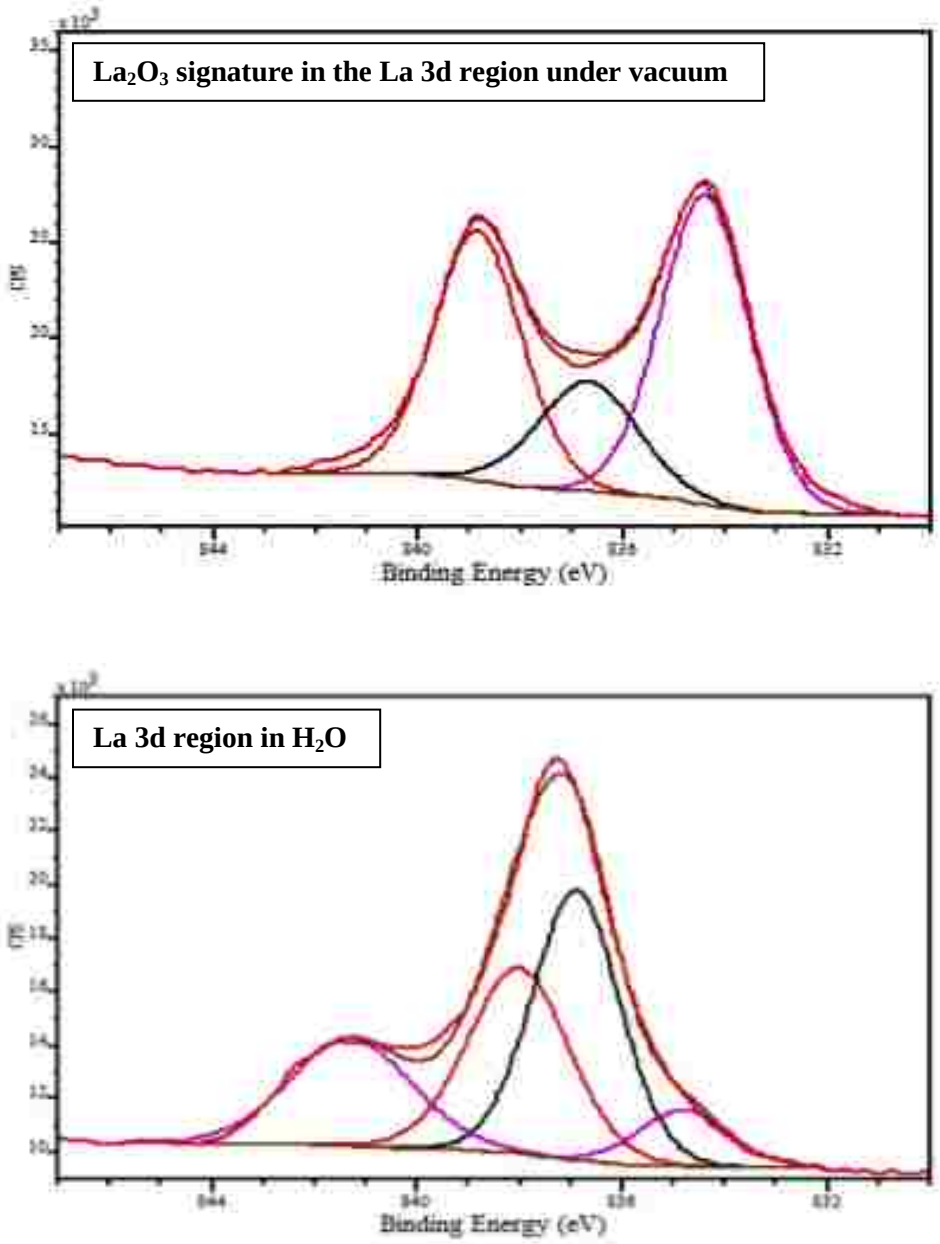

Figure 7-6. XPS spectra of the La 3d region for the $Ni_{0.95}La_{0.05}$ catalyst in vacuum (a) and in H_2O (b).

Indication of the formation of a La-OH phase can be confirmed by investigating the O 1s region shown in figure 7.7 below. The strongest peak for both spectra shown in figure 7.7 appears at 530.2 eV. This peak is attributed to the oxygen in La_2O_3 as it has been reported

previously [76, 77]. The second strongest component observed in both vacuum and H_2O samples appears at 532.0 eV. This peak is characteristic of the OH in $La(OH)_3$ [78]. Lastly, a smaller peak is observed in the $Ni_{0.95}La_{0.05}$ catalyst under H_2O at 533.5 eV. This peak has been identified before as the adsorption of water [79].

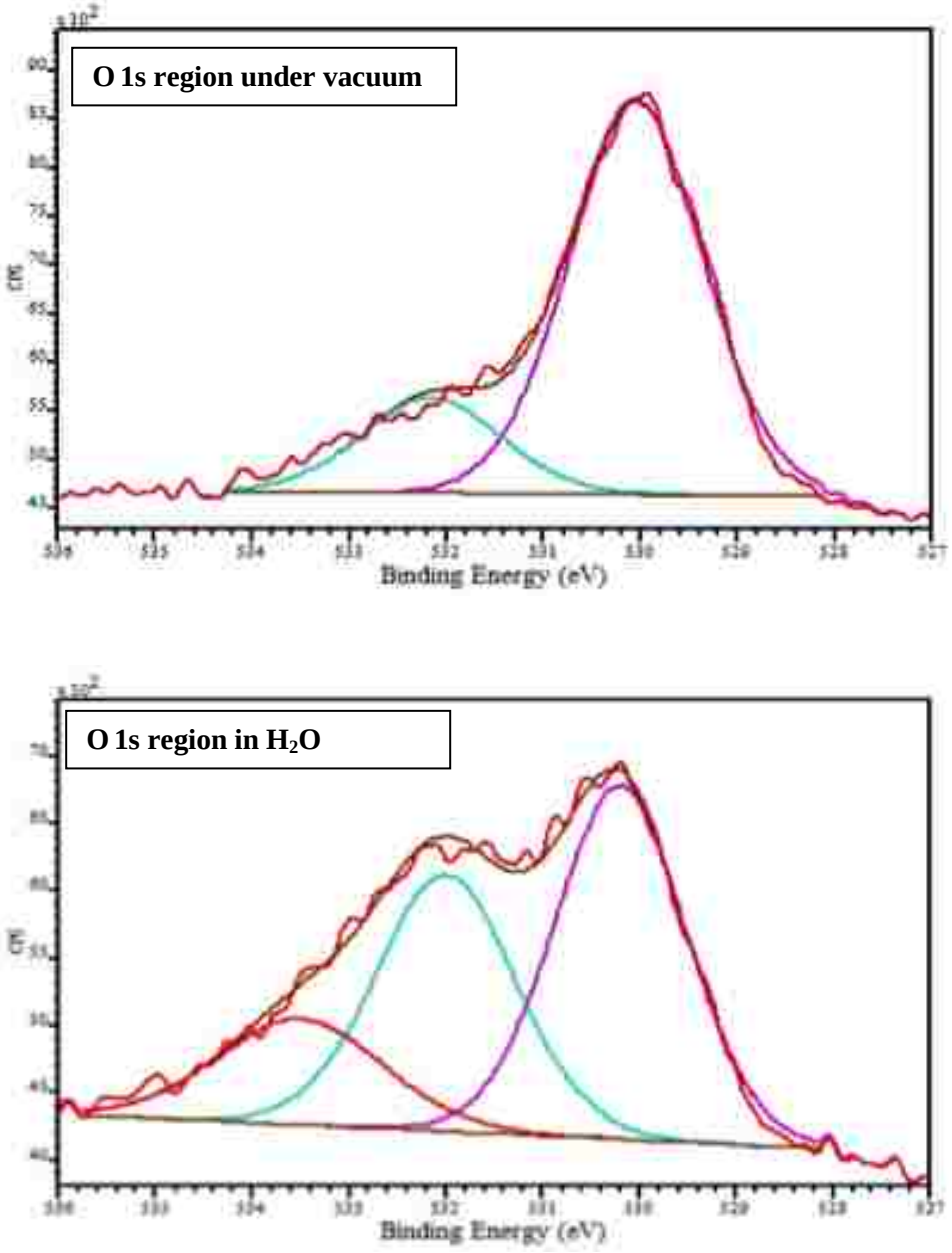

Figure 7-7. XPS spectra for the La 3d and O 1s region in vacuum.

Table 7-1. Peak positions and relative intensities for La $3d_{5/2}$ and O 1s regions.

	La $3d_{5/2}$				O 1s		
Position (eV)	834.6	837.0	838.2	841.3	530.2	532.0	533.5
Identification	La_2O_3	satellites			La_2O_3	OH	H_2O
In vacuum	45.4	18.2	36.4	0.0	79.6	20.4	--
In H_2O	8.5	38.9	30.9	21.8	46.4	35.9	17.6

7.3.4 In Situ IRRAS Experiments

In situ infrared reflection absorbance spectroscopy (IRRAS) studies were conducted to identify intermediates and understand the mechanism of reaction of the most active electrocatalyst $Ni_{0.90}La_{0.10}$. Figure 7.8 shows the infrared spectra taken at 25 °C and 0 rpm from the potential range of -0.4 V to 0.4 V (vs. RHE). All spectra shown in Figure 7.8 are compared to a reference spectrum taken at the starting potential. Therefore, a trough represents the disappearance of species, while a peak represents a new kind of species being formed.

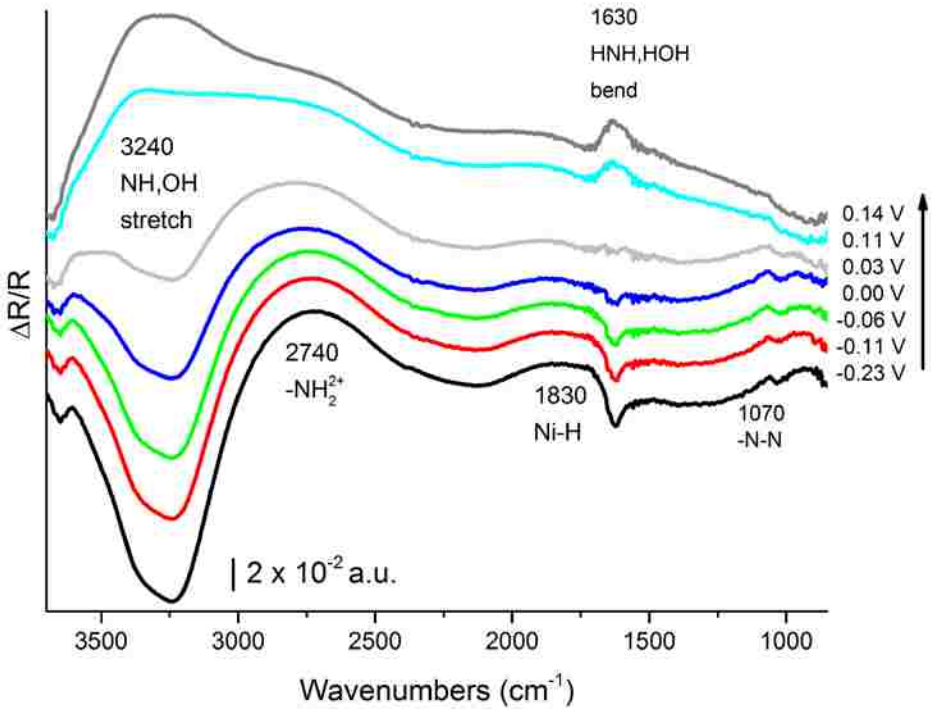

Figure 7-8. IRRAS spectra of hydrazine oxidation on the $Ni_{0.90}La_{0.10}$ electrocatalyst.

The summary of the peaks and troughs observed from infrared spectra are shown in table 7.2.

Table 7-2. IRRAS band assignments for hydrazine oxidation on $Ni_{0.90}La_{0.10}$ electrocatalysts.

Wavenumber (cm^{-1})	Assignment
3240	N-H, O-H stretch
2740	$-N-H_2^{+2}$
1830	Ni-H stretch
1630	NH, OH bend
1070	-N-N stretch (in hydrazine)

At low potentials, troughs appear at 3240 cm^{-1} and 1624 cm^{-1} representing a decrease in N-H/O-H species. This decrease of O-H species could be attributed to the adsorption of hydrazine hydrate releasing water according to the following reaction,

$$N_2H_4 \cdot H_2O \rightarrow N_2H_{4ads} + H_2O. \quad (7.1)$$

Correspondingly, as the hydrazine is adsorbed amine salts are formed due to the dehydrogenation of hydrazine as follows,

$$N_2H_{4ads} \rightarrow 2H_{ads} + {N_2H_2}^{+2}{}_{ads} \quad (7.2)$$

Or

$$N_2H_{4ads} + 2OH^- \rightarrow 2H_2O + {N_2H_2}^{+2}{}_{ads}. \quad (7.3)$$

These amine salts appear in the infrared spectrum at wavenumbers 2718 cm-^{1} (-N-H_2^{+2}) and 1064 cm^{-1} (-N-N stretch in hydrazine) [63-65]. Promotion of catalysis by the presence of lanthanum hydroxide could be observed by the broad infrared peak occurring at 1836 cm^{-1}, which could be attributed to the Ni-H vibration as shown in equation (7.2) [66]. Thus, lanthanum hydroxide promotes the dehydrogenation of hydrazine by nickel as it has been reported for Ni alloys [36].

Figure 7.9 below displays the peak areas for the absorbance of the N-H and O-H vibrations along with the –N-NH_2^{2+} species plotted along with the linear sweep voltammogram for the reaction.

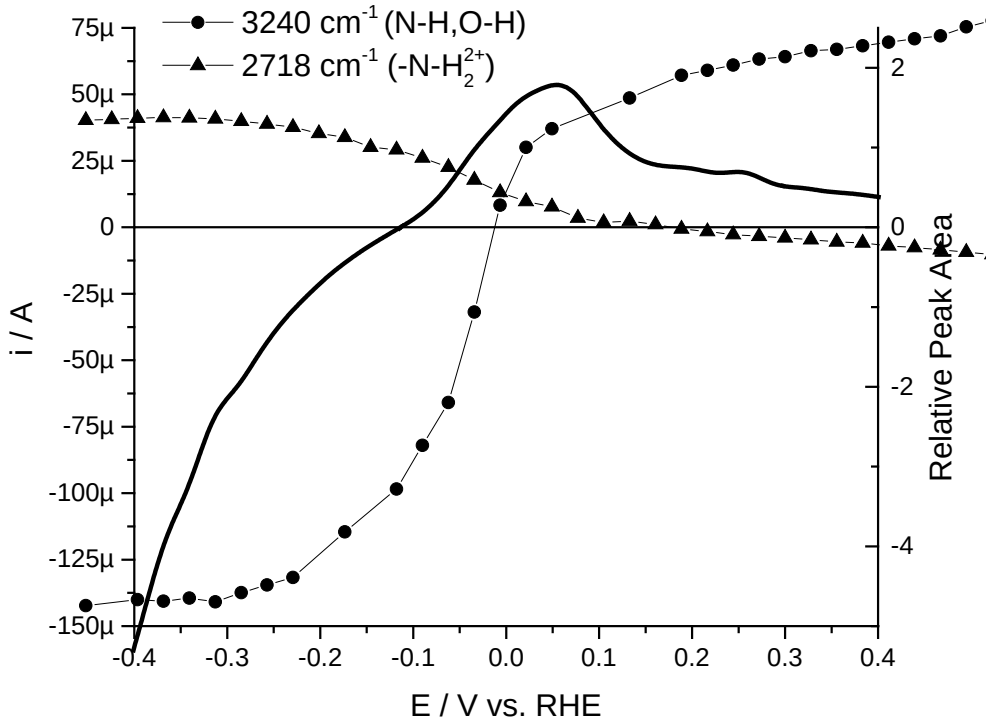

Figure 7-9. Corresponding LSV of the hydrazine reaction on $Ni_{0.90}La_{0.10}$.

Conditions: 1 mV/s, 1 M KOH, 0.1 M hydrazine hydrate, 25°C, 0 rpm.

From this figure, it can be observed that the decrease in the N-H/O-H species due to the adsorption and partial dehydrogenation of hydrazine at the beginning of the sweep start to increase as the reaction approaches the onset potential. Simultaneously, the $–N\text{-}NH_2^{2+}$ species start to decrease. These simultaneous reactions can be attributed to the oxidation of the amine salt to form nitrogen and water according to the following reaction,

$$N_2H_2^{+2}{}_{ads} + 2OH^- \rightarrow N_2 + 2H_2O + 2e^- \qquad (7.4)$$

As the reaction reaches its maximum current at 0.06 V, the presence of $–N\text{-}NH_2^{2+}$ species nears zero and no more water is being produced. At this point the catalyst is completely passivated and inactive towards the oxidation of hydrazine.

Similar mechanisms of the hydrazine oxidation have already been suggested. A highly active α-NiZn catalyst was previously reported with a similar mechanism of oxidation in which the increased performance was due to an intrinsic effect caused by the Zn on the Ni catalyst [36]. For the oxidation of hydrazine on a Pt electrode, Kodera *et al*. suggested the formation of a $N_2H_2^{+2}{}_{ads}$ intermediate [41].

7.3.5 Fuel Cell Performance Evaluation of the $Ni_{0.90}La_{0.10}$ Catalyst

Figure 7.10 shows the single MEA fuel cell performance of DHAFCs operated at 80°C using $Ni_{0.90}La_{0.10}$ as an anode catalyst compared to a conventional Ni catalyst (210H, INCO) as reference. Co−PPY−C was used as a cathode catalyst for both fuel cells. The results of MEA evaluation are summarized in table 7.3. Open circuit voltages (OCV) were similar for both electrocatalysts, 0.746 V for Ni and 0.751 V for $Ni_{0.90}La_{0.10}$. A maximum power density of 453 $mW \cdot cm^{-2}$ was obtained from the $Ni_{0.90}La_{0.10}$ DHAFC, which is 1.14 times higher than that obtained from the Ni DHAFC. Thus, the improved performance observed from the RDE evaluations was confirmed at the fuel cell level. Both DHAFCs tested revealed high performances without the need of precious metal catalysts for both anode and cathode electrodes highlighting the promising development of affordable fuel cell technology.

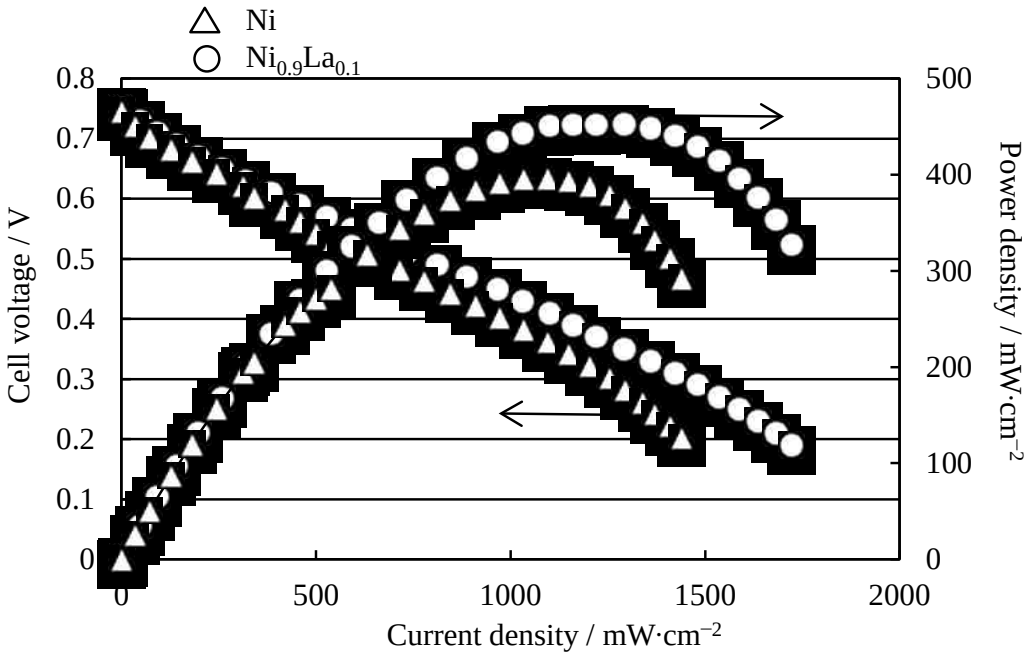

Figure 7-10. Single MEA fuel cell performance of the $Ni_{0.90}La_{0.10}$ electrocatalyst compared to Ni (210H, INCO). Loading of anode / cathode is 2.7 / 0.24 mg·cm^{-2}

Table 7-3. Results of fuel cell performances.

Anode Catalyst	Open Circuit Voltage (V)	Maximum Power Density (mW/cm^2)
Ni (210H, INCO)	0.746	397
$Ni_{0.90}La_{0.10}$	0.751	453

7.4 Conclusions

This study has reported a thorough understanding of the physical and chemical structure, reaction mechanisms, and electrochemical performance of spray pyrolyzed $Ni_{1-x}La_x$ electrocatalysts. Physical and chemical characterization through a number of different techniques revealed the presence of a β-La_2O_3/$La(OH)_3$ phases for the most active catalysts. XPS studies revealed the formation of a La-OH species on the surface of

the $Ni_{0.95}La_{0.05}$ catalyst when exposed to water. Thus, the improved performance observed from both $Ni_{0.90}La_{0.10}$ and $Ni_{0.95}La_{0.05}$ can be attributed to the presence of an $La(OH)_3$ phase responsible for the providing hydroxide ions to the surface of the electrode for the oxidation of $N\text{-}NH_2^{2+}$ adsorbed species as it was observed from the *in situ* IRRAS studies. Promotion of catalysis by an oxide phase could be attributed to synergistic effect where the oxide phase is capable of bringing hydroxide ions near the surface of the electrode at much lower potentials than pure metals. Observed single MEA fuel cell performance of the $Ni_{0.90}La_{0.10}$ electrocatalyst is comparable to the performances observed from H_2/O_2 PEMFCs. Therefore, the development of new DHAFCs using Pt-free electrocatalysts present a promising and affordable technology for applications ranging from stationary to mobile applications.

Part II.

Direct Ethanol Fuel Cells

8. Direct Ethanol Fuel Cells

8.1 Introduction

The necessity for clean, renewable alternative fuel sources to reduce the dependence on petroleum has focused its attention on using ethanol as a fuel. Ethanol can be obtained through the fermentation of renewable biomass resources such as sugar cane and corn. There is considerable research and development of fuel cell technologies using direct alcohol fuel cells (DAFCs) in which alcohols are directly oxidized at the anode instead of being used in steam reforming for hydrogen production. Methanol, although not renewable, is the simplest and the most investigated alcohol. However, the toxicity and low boiling point exhibit important disadvantages for using methanol as a fuel source. Ethanol has low toxicity, high boiling point, and more importantly, an energy density similar to that of gasoline (8 kWh/kg). Additionally, ethanol can be stored and transported with the use of the current infrastructure. Therefore, direct ethanol fuel cells (DEFCs) is a promising emerging technology that can transform the chemical energy stored in ethanol into electrical energy to power a number of devices ranging from portable applications to vehicles. However, the commercialization of DEFCs has been limited by the use of expensive noble catalysts generally used for the oxidation of small molecules as well as poor kinetics of the electrooxidation of ethanol.

Regardless of its high cost and scarcity, current catalysts of choice for the oxidation of small molecules remain Pt-based catalysts. However, these compounds present important drawbacks for their employment as catalysts for the electrooxidation of

ethanol. Pt-based catalysts have shown to only partially oxidize ethanol into acetaldehyde, acetic acid, or acetate, depending on the pH of the solution. Partial oxidation of ethanol produces only a 2- and 4-electron transfer. Maximum performance from DEFCs can be achieved by completely oxidizing ethanol into CO_2 producing a 12-electron transfer. The mentioned electrochemical reactions for a low pH environment are listed below.

Complete oxidation reaction	$C_2H_5OH + 3H_2O \rightarrow 2CO_2 + 12H^+ + 12e^-$	(8.1)
Partial oxidation reactions	$C_2H_5OH \rightarrow CH_3CHO + 2H^+ + 2e^-$	(8.2)
	$C_2H_5OH + H_2O \rightarrow CH_3COOH + 4H^+ + 4e^-$	(8.3)

Another issue with Pt-based catalysts is the poisoning of the catalytic active sites due to the strong adsorption of the intermediate CO species formed. These challenges highlight the need for the development of new multifunctional electrocatalysts that will fully oxidize ethanol into CO_2 in addition to eliminating poisoning problems caused by CO adsorption.

The main challenge to reach complete oxidation of ethanol at the anode lies in the inability to cleave the C-C bond. High yields of acetaldehyde and acetic acid have been seen as the main products using Pt catalysts in acid media [80, 81]. Electrocatalytic systems used today do not possess the selectivity to completely oxidize ethanol into CO_2. The best performing catalytic systems currently used for the electrooxidation of ethanol are Pt-based binary catalysts, PtSn and PtRu. Overall, bimetallic systems used as catalysts have been known to provide stability, increased reactivity, and increased functionality for many catalytic systems. The superior performance observed on these

catalysts is attributed to two different effects caused by the addition of a second metal to Pt. The bifunctional or promoted mechanism effect refers to a synergistic contribution by each of the components of the binary system. In the case of alcohols, the presence of oxophilic metals such as Sn and Ru promotes the oxidation of adsorbed oxygen-containing species. An electronic or intrinsic mechanism effect takes place when the presence of an additional metal in proximity to each Pt atom modifying its electronic structure. This electronic modification can be fine-tuned into a more desirable surface electronic structure by coupling different metal ligands according to the desired catalytic reaction [82, 83].

An extensive review of publications on PtSn and PtRu catalytic systems was published by Antolini [82]. In summary, when comparing the results obtained from PtSn and PtRu catalysts, Pt is a better performing catalyst for the electrooxidation of ethanol when alloyed to Sn as compared to Ru [84, 85]. However, there is no agreement as to which composition of PtSn is the ideal composition for maximum activity. Different synthesis methods have produced different results. For example, Zhou *et al* reported optimum composition with 33-40 at.% Sn for PtSn catalysts synthesized by a modified polyol process [85]. Conversely, Lamy *et al* found an optimum composition in the 10-20 at.% Sn range for PtSn catalysts synthesized by the Bönneman method [86]. The difference in performance for Pt_xSn_y alloys might be attributed to the homogeneity of each catalyst tested. While two catalysts with the exact same composition might be expected to perform similarly, there are a number of factors that have to be considered to determine whether two catalysts are comparable. Among these factors the most important includes the extent of the alloying, in other words, the performance of the

Pt_xSn_y catalyst will depend on whether Pt_xSn_y forms a single phase or whether Pt_xSn_y is a multiphase catalyst.

Jiang *et al* highlighted the importance of Pt_xSn_y alloys with either homogenous or heterogeneous phases [87]. They found that a heterogeneous Pt-SnO_x catalyst has a higher catalytic activity for ethanol electrooxidation than a single phase homogeneous PtSn alloy, both having the same Pt:Sn ratio of 3:1. They attribute the higher activity to the favorable ethanol adsorption on Pt nanoparticles in conjunction with SnO_x particles offering oxygen species for the oxidation of CO-like species adsorbed on Pt sites. In the case of the PtSn alloy, the lower activity can be caused by the inhibition of the hydrogen adsorption/desorption region, and thus dehydrogenations steps, which was shown by cyclic voltammetry.

Although PtSn and PtRu are the better catalysts for ethanol oxidation in acidic media, neither of these catalysts are selective towards the complete oxidation of ethanol [88]. A more selective catalyst has been found in PtRh [89, 90]. PtRh/C catalysts increased the efficiency of ethanol oxidation to CO_2 from 0.08 for Pt/C to 0.50 for $Pt_{47}Rh_{53}$/C (at 0.7 V vs. RHE). Increased selectivity is attributed to modification on the electronic structure of Pt by the addition of Rh in a way that Pt-adsorbate interactions are weakened, thus, lowering the energy barrier for oxidation. Unfortunately, current densities obtained from this catalytic system did not increase in response to increased selectivity. This phenomenon could be attributed to a decrease of Pt content by the substitution of Pt atoms with Rh atoms in the bimetallic catalysts, or also, the segregation of Rh to the surface of the nanoparticle due to the higher adsorption energy for Rh-CO

than for Pt-CO. Therefore, Pt-based catalysts have not addressed the need for a highly selective and high performing catalyst for the oxidation of ethanol.

Selection of metal ligands is limited when using an acidic electrolyte due to its inherently corrosive environment. Advantageously, recent studies have reported faster kinetics can be achieved for methanol and ethanol oxidation in high alkaline pHs [10, 11]. These alkaline environments present the opportunity of using a wider range of catalytic systems due to the less corrosive environment. Furthermore, kinetics of the oxygen reduction reaction have been found to be more facile in alkaline electrolyte when compared to acidic electrolytes such as H_2SO_4 and $HClO_4$ [91, 92]. Thus, the wider range of catalytic systems available in alkaline media might provide the solution for the development of a highly selective catalyst for the complete oxidation of ethanol.

The advantages of operating in alkaline conditions are numerous. In addition to the improved kinetics previously mentioned, high pH environments provide the advantages of having a wider range of possible catalytic systems due to the abundance and low cost of non-noble transition and rare-earth metals. Conversely, the main disadvantage of using direct alcohol alkaline fuel cells is the possible carbonation of the electrolyte due to CO_2 retention from the oxidation of the fuel as well as from the air. This carbonation can cause solid precipitation of carbonate salts and decrease the pH of the solution. However, development of new solid alkaline electrolytes as well as new concepts such as electrolyte recirculation and carbonate electrolytes are keeping the interest on direct alcohol alkaline fuel cells alive [5, 93, 94]. Research on the electrooxidation of ethanol in alkaline media is only at its early stages and has not been

researched to the same extent of alcohol oxidation in proton exchange membrane fuel cells. Thus, the field is wide open to contributions in this area.

Numerous reports have shown Pd as a better catalyst for the oxidation of ethanol in alkaline media when compared to Pt [72, 95-97]. Other reports have compared the performance of Pt/C and Pd/C with the addition of oxides such as CeO_2, ZrO_2, MgO, Co_3O_4, Mn_3O_4, NiO and In_2O_3 in alkaline media [97]. For all of these catalytic systems tested, Pd-NiO/C showed the highest activity in terms of both the lowest onset potential and highest peak current density (Figure 8.1) [68, 72]. Further studies attributed this finding to a weaker adsorption of CO species on Pd-NiO/C [98]. Moreover, the addition of oxides benefits the onset potential of ethanol oxidation in comparison to the pure metal systems, Pd/C and Pt/C. This phenomenon can be due to a similar mechanism compared to that of Ru and Sn play in Pt-based catalysts in acidic environments, where a surface hydroxide is formed at the oxide particles facilitating the oxidation of CO-like species at lower potentials.

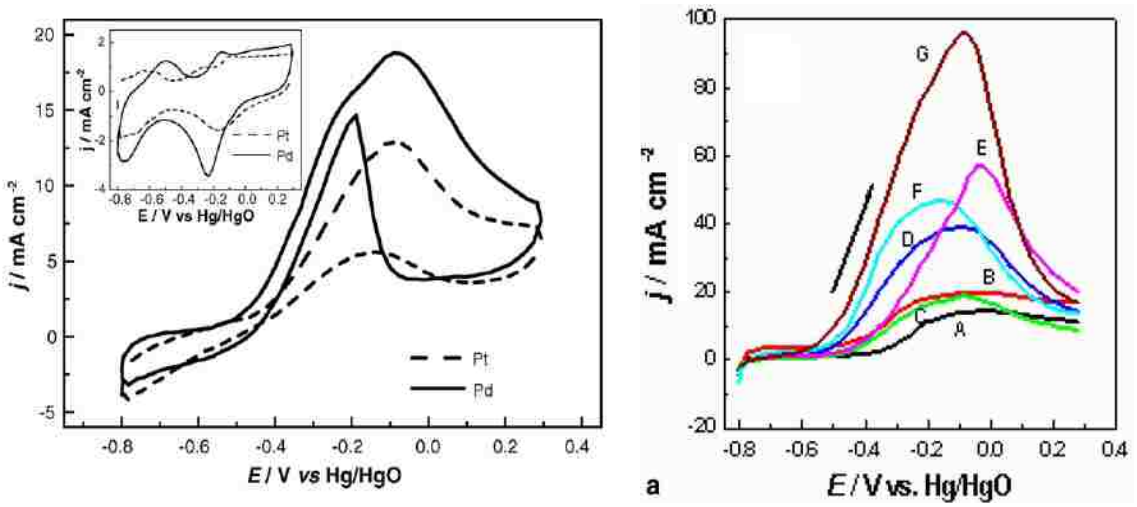

Figure 8-1. Performance comparison of Pt/C and Pd/C in alkaline media (1M KOH, 1M ethanol, 0.30 mg Pd/cm^2, left) [72]. Comparison of performance of the addition of different oxides: [A. Pt/C; B.PtRu/C; C.Pd/C; D.Pd-CeO_2/C; E.Pd-Co_3O_4/C; F. Pd-Mn_3O_4/C; G. Pd-NiO/C] (1M KOH, 1M ethanol, 0.30 mg Pd/cm^2, right) [68].

Bambagioni *et al.* has also reported the high performance of a catalyst prepared by spontaneous deposition of Pd through redox transmetalation reaction on Ni-Zn/C and Ni-Zn-P/C supports [99]. According to this report, Pd-(Ni-Zn)/C performs better than Pd-(Ni-Zn-P)/C and Pd/C catalysts (Figure 8.2). Characterization of these materials demonstrated that the highest performing ternary catalytic system, Pd-(Ni-Zn)/C, is actually a binary system composed of separate Pd and Ni nanoparticles, which are not alloyed; thus, the redox transmetalation reaction occurred between Pd and Zn. Although this catalyst is able to produce specific currents around 3600 A/g_{Pd}, comparing this result to that obtained by Xu *et al* [72], it is more likely that this result is due to a particle size and dispersion effect rather than an effect produced by the presence of Ni particles in the binary system.

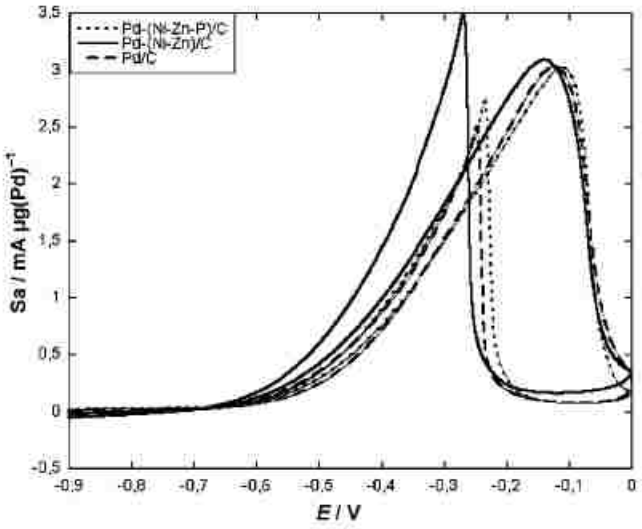

Figure 8-2. Cyclic voltammograms of ethanol oxidation on Pd/C, Pd-(Ni-Zn)/C, and Pd-(Ni-Zn-P)/C electrodes (E vs. Ag/AgCl/KCl$_{sat}$, 2M KOH, 10 wt% ethanol) [25].

In order to improve the catalytic activity of Pd systems toward the complete electrooxidation of ethanol it is necessary to design catalysts that will hinder the formation of undesired intermediates as well as improving the kinetics of the desired rate determining step. For this goal to be achieved further understanding of the possible reaction mechanism is necessary. It is generally agreed that oxidation of alcohols occurs following two different pathways: one is the C-C breakage involving a CO intermediate, and the other pathway involves the conservation of the C-C bond which results into acetaldehyde, acetic acid, or acetate depending on the operating pH of the solution. For either pathway, the role of the hydroxide ions in alkaline electrolytes must be taken into account as it becomes important for the final step of the oxidation of adsorbed CO species from the active sites of the catalyst.

Zhao *et al* has reported on a mechanistic study of the partial oxidation of ethanol on a Pd catalyst in alkaline media [100]. The mechanism derived by DFT studies can be summarized as follows:

$$CH_3CH_2OH + OH^- \rightarrow CH_3CHOH^- + H_2O \quad (8.4)$$

$$Pd + CH_3CHOH^- \rightarrow Pd\text{-}CH_3CHOH_{ads} + e^- \quad (8.5)$$

$$CH_3CHOH \rightarrow CH_3CHO + H_{ads} \quad (8.6)$$

According to this study the main reason that Pd is not an active catalyst for the oxidation of ethanol in acidic media is due to the lack of OH^- groups necessary for cleaving of the α-H atom (CH_3CH_2OH) and activating the ethanol molecule. Additionally, this article suggested that the rate determining step for the partial oxidation of ethanol is the removal of the adsorbed species through oxidation by $Pd\text{-}(OH)_{ads}$ groups in proximity to the adsorbed acyl group, *i.e.*

$$Pd\text{-}(COCH_3)_{ads} + Pd\text{-}OH_{ads} \rightarrow Pd\text{-}CH_3COOH_{ads} + Pd \quad (8.7)$$

The reaction mechanism proposed suggests a dependence on the concentration of hydroxide ions at the surface of the electrode as the hydroxide ions are important for the improvement of the rate determining step of the oxidation of ethanol in alkaline media on Pd-based systems by removing adsorbed species. More importantly, in order to achieve full oxidation of the ethanol molecule it is necessary to cleave the β-H atom (CH_3CH_2OH) in order for the β-C to adsorb. Several groups have suggested these C_{1ads} and C_{2ads} as the intermediates formed towards the complete oxidation of ethanol [82, 101,

102]. Adzic *et al* were able to fully oxidize ethanol into CO_2 by employing a ternary PtRh-SnO_2/C catalyst in an acidic electrolyte. The suggested mechanism following the α-H atom dehydrogenation and adsorption is as follows:

$$CH_3CH_2OH_{ads} \rightarrow CH_3CH_2O_{ads} + H_{ads} \rightarrow CH_2CH_2O_{ads} + 2H_{ads} \rightarrow CH_{2ads} + CH_2O_{ads} + 2H_{ads}$$

The ability to break the C-C bond in this ternary catalyst was attributed to a specific property found in each of its constituents. Pt atoms are involved in the initial and subsequent dehydrogenation reactions, Rh or a PtRh alloy is responsible for the cleavage of the C-C, and SnO_2 is involved in the activation of H_2O at low overpotentials and further oxidize the CO_{ads} complex into CO_2.

As reported by Zhao *et al*, the rate limiting step in the oxidation of ethanol using Pd as a catalyst was stated to be the oxidation of CO-adsorbed species [100]. This step is limited by the Pd properties for water activation since it requires the presence of Pd-OH_{ads} species. Oxophilic metals require a much lower potential to activate water and form the necessary oxide layer. The design of new multifunctional catalysts for the complete electrooxidation of ethanol based on principles of rational design gained from the knowledge and understanding from parallel projects moves closer towards the goal of catalyst design. Furthermore, understanding of the role of oxiphilic ligands in the mechanism of ethanol oxidation in alkaline media is essential for the application to other fuels or the development of a ternary catalytic system to break the C-C bond.

9. Pd/SnO_2 Electrocatalysts for the Oxidation of Ethanol

9.1 Introduction

Fundamental studies of the ethanol electrooxidation on Pt-based catalysts in acid electrolytes have been widely reported in the literature [54, 80, 88, 89, 103, 104]. However, very few mechanistic studies exist for ethanol oxidation in alkaline solutions. The electrooxidation of ethanol is a very complex reaction with multiple pathways. In an alkaline electrolyte, ethanol electrooxidation can result in a 2-, 4-, or 12-electron transfer as shown below.

$$CH_3CH_2OH + 2OH^- \rightarrow CH_3CHO + 2H_2O + 2e^- \quad (9.1)$$

$$CH_3CH_2OH + 4OH^- \rightarrow CH_3COOH + 3H_2O + 4e^- \quad (9.2)$$

$$CH_3CH_2OH + 12OH^- \rightarrow 2CO_2 + 9H_2O + 12e^- \quad (9.3)$$

Unquestionably, the desired reaction is the complete oxidation of ethanol to CO_2 producing a 12-electron transfer to obtain the maximum energy density. Zhou *et al.* and Fang *et al.* [105, 106] have reported *in situ* FTIR studies on the mechanism of ethanol electrooxidation on Pd electrodes in alkaline environments at different concentrations. Both studies report acetate as the main oxidation product. Fang *et al.* observed the best performance in a 1M NaOH solution.

Improved stability, reactivity, and functionality has been observed from alloyed and supported catalysts. The improved performance of these multifunctional catalysts has

been attributed to two different effects caused by the interaction of the primary catalyst with a second element either by a promotion or intrinsic effect. A promotion effect refers to a synergistic contribution by each of the components of the multiphase system. In the case of alcohols, the presence of oxide supports has shown to promote the catalytic activity of the main catalysts. Xu *et al.* has demonstrated this promotion effect on Pd catalysts using CeO_2, NiO, Co_3O_4, and Mn_3O_4 to improve the electrooxidation performance on a number of different alcohols [72, 73]. An intrinsic effect is caused by the alloying of a second metal modifying the electronic structure of the primary catalyst inducing a higher catalytic performance. Oxophilic metals, such as Ru, Sn, and Ni, have shown to improve the catalytic performance of Pt and Pd catalysts for alcohol electrooxidation [59, 107-110].

There have been a few studies reporting the improvement on the catalytic activity of Pd by alloying with Sn for the electrooxidation of ethanol in alkaline environments. Du *et al.* [108] has reported the benefit of alloying Sn with Pd on carbon supported catalysts synthesized via the polyol method. The study reports an increased current density of two times over commercial Pd/C catalysts, with an optimal Sn content of 14 at%. Reaction studies suggest ethanol is only partially oxidizing to produce acetic acid as the main product. Similarly, He *et al.* [111] reported the promoting effect of Sn on $Pd_{2.5}Sn$/C catalysts resulting in increased current densities in 0.25 M KOH. However, there are no reports on using Pd/SnO_2 in alkaline environments.

This study reports on the activity of highly active Pd/SnO_2 catalysts for the electrooxidation of ethanol along with mechanistic studies based on *in situ* FTIR

spectroscopy. Reaction mechanisms will be analyzed in two different electrolyte concentrations 0.1 M and 1M KOH, *i.e.* different pH. Particular attention will be focused to the pH effect in relationship to performance versus selectivity of the ethanol electrooxidation.

9.2 Experimental

9.2.1 Synthesis of Electrocatalysts

Two different methods were utilized to synthesize SnO_2: spray pyrolysis (SP) and sacrificial support (SS). Spray pyrolyzed SnO_2 was synthesized using a $SnCl_4$ precursor (Sigma-Aldrich Co.) dissolved in deionized water to a final concentration of 5 wt.%. The precursor solution was ultrasonically atomized and pyrolyzed using a quartz tube in a furnace operating at 500°C using air (0.5 L/min) as the carrier gas. Pyrolyzed particles were collected and air dried on a Teflon filter. Collected oxide precursor was heat treated in air at 300°C for 2 hours. Similarly, SnO_2 was also synthesized through a sacrificial support method. The sacrificial support method is based on the implementation of silica materials instead of conventional carbon supports. First, silica (Cab-O-Sil, EH-5, surface area: ~400 m^2g^{-1}) was dispersed in water using an ultrasound bath. $SnCl_4$ (Sigma-Aldrich) was then added to the silica solution. Total loading of metals on silica was calculated to be 20 wt.%. Pd(NO_3) precursor was chemically reduced onto both oxides by using excess amount of $NaBH_4$ added drop-wise to the precursors-silica solution under constant ultrasonication. The resulting black slurry was aged for 2 h. The silica support was etched by means of 7 M KOH for 8 h. Pd/SnO2 catalysts were washed with deionized water until neutral reaction of water. The Pd to Sn ratio (atomic) was selected

as 3:1. In order to compare the catalytic activity of Pd/SnO2 catalysts with Pd, unsupported Pd catalyst was synthesized by the chemical reduction method described above.

9.2.2 Catalyst Characterization

Phase composition and morphologies of the synthesized catalysts were characterized using X-Ray Diffraction (XRD), Scanning Electron Microscopy (SEM), High-Resolution Transmission Electron Microscopy (HRTEM), and Energy Dispersion Spectroscopy (EDS). X-ray powder diffraction spectra were recorded using Scintag Pad V diffractometer with DataScan 4 software (MDI, Inc.) for system automation and data collection. Cu Kα radiation (40 kV, 35 mA) was used with a Bicron Scintillation detector (with a pyrolitic graphite curved crystal monochromator). Data sets were analyzed with Jade 9.5 Software (MDI, Inc.) using the ICDD (International Center for Diffraction Data) PDF2 database (rev. 2004) for phase identification.

Scanning electron microscopy (SEM) was performed on a Hitachi S-5200, with a resolution of 0.5 nm at 30 kV and 1.7 nm at 1 kV, equipped with PGT EDS. Transmission electron microscopy (TEM) was performed on a JEOL 2010F FASTEM field emission gun scanning transmission electron microscope equipped with Oxford EDS. The probe size was 1.0 nm, and accelerating voltage was 200kV.

9.2.3 Electrochemical Measurements

An aqueous suspension (5 mg/mL in H_2O:isopropanol [4:1]) of each catalyst was prepared and sonicated to disperse the powder in solution. 10 µl aliquots of the aqueous

suspension were deposited onto a glassy carbon rotating-disc electrode (RDE) and allowed to air dry. Electrochemical measurements were conducted in 0.1M and 1 M KOH with N_2 as the purging gas. Ethanol (Sigma-Aldrich Co.) was added to the electrolyte at 1M concentration. A Pt-coil was used as a counter electrode and a Hg/HgO electrode (XR440, Radiometer Analytical SAS) was used as reference electrode.

9.2.4 Infrared Spectroscopy

In Situ Infrared Reflection Adsorption Spectroscopy (IRRAS) experiments were performed at room temperature with a Nicolet 6700 FT-IR spectrometer equipped with a Mercury Cadmium Telluride (MCT) detector cooled with liquid nitrogen. Experimental setup is described previously [54]. For each spectrum, 128 interferograms were added together at a resolution of 8 cm^{-1} with unpolarized light. Absorbance units of the spectra are defined as $A = -\log(R/R_0)$, where R and R_0 represent reflected IR intensities corresponding to the sample and reference single beam spectrum, respectively. Thus, a positive peak in the resulting spectrum indicates a production of species, while a negative peak indicates consumption or decrease in concentration of a species compared to the reference spectrum. The reference spectrum was collected at -1.04 V (vs. Hg/HgO). A thin layer of ink was pipetted onto a polished glassy carbon electrode with a diameter of 5 mm. A ZnSe hemisphere was used as the IR window, and the working electrode was pressed against the window, creating a thin solution layer with a thickness of a few micrometers. The incident angle of the IR radiation passing through the ZnSe window was 36° [55]. Argon was used to purge the electrolyte while dry air was used to purge the

spectrometer and chamber, reducing the spectral interference from ambient CO_2 and water vapor.

9.3 Results and Discussion

9.3.1 Electrocatalyst Characterization

Phase composition of synthesized catalysts was characterized through X-ray diffraction. Figure 9.1 below displays XRD spectra for both Pd/SnO_2 (Sacrifical Support) and Pd/SnO_2 (Spray Pyrolysis). Diffraction peaks at 2θ angles 40.0°, 46.3°, 67.7°, and 81.5° confirm the FCC palladium diffraction planes (111), (200), (220), and (311), respectively. Similarly, peaks at angles 26.6°, 33.8°, and 51.8° confirm diffraction planes (110), (101), and (211) for the SnO_2 phase. The crystallite size of the Pd nanoparticles was calculated from the Pd (111) peak using the Scherrer equation. Crystallite size of Pd nanoparticles are very similar for both catalysts, 6.5 nm for Pd/SnO_2(SP) and 6.9 nm for Pd/SnO_2(SS). On the other hand, the crystallite size for SnO_2 differed depending on the synthesis method. Spray pyrolyzed SnO_2 has a crystallite size of 3.3 nm whereas SnO_2 synthesized through the sacrificial support method resulted in a higher crystallite size of 4.6 nm based on the (110) peak for SnO_2.

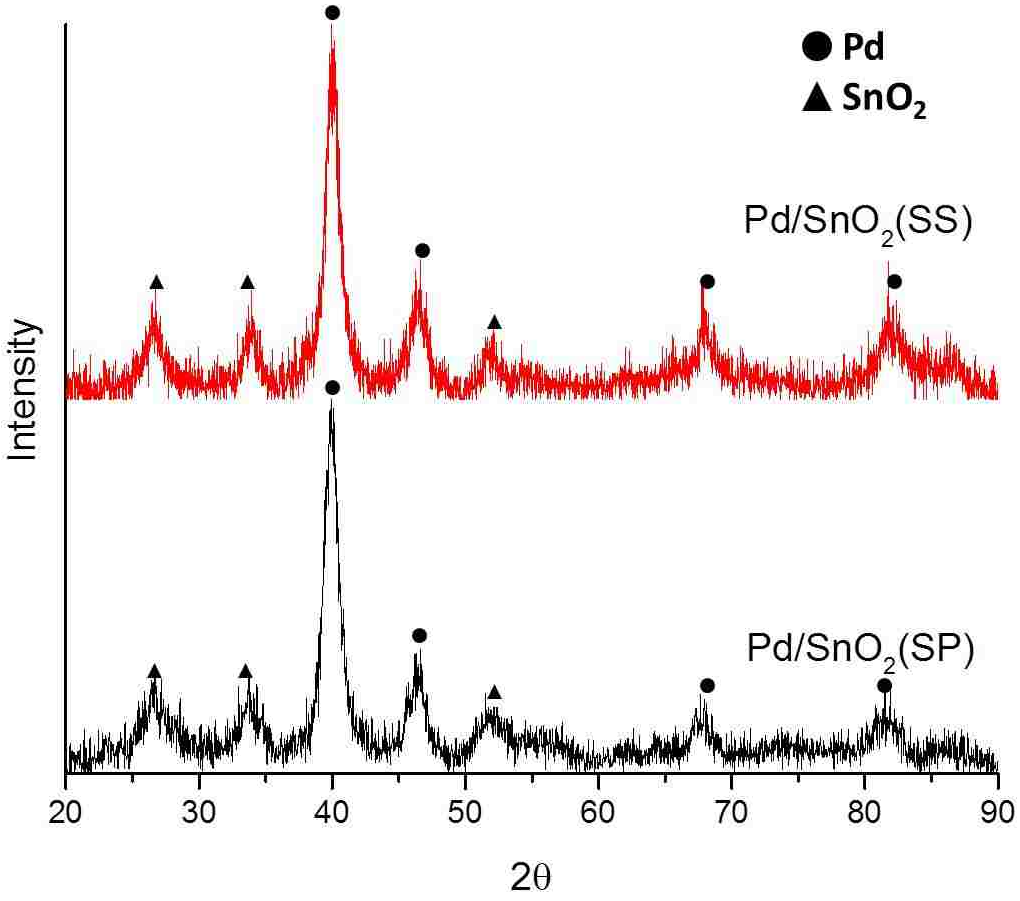

Figure 9-1. XRD spectra for the two Pd/SnO_2 electrocatalysts.

SS—sacrificial support, SP—spray pyrolyzed.

Further morphological information was obtained from scanning electron micrographs. Figure 9.2 below shows the morphological difference between both electrocatalysts. Spray pyrolyzed tin oxide, SnO_2(SP), consisted of sub-micron size spherical particles composed of agglomerated nanoparticles of about 3.3 nm in size (Figure 9.2, right). Conversely, tin oxide synthesized through the sacrifical support method, SnO_2(SS), consists of large micron size bulk particles with porosity in the tens of nanometers (Figure 9.2, left).

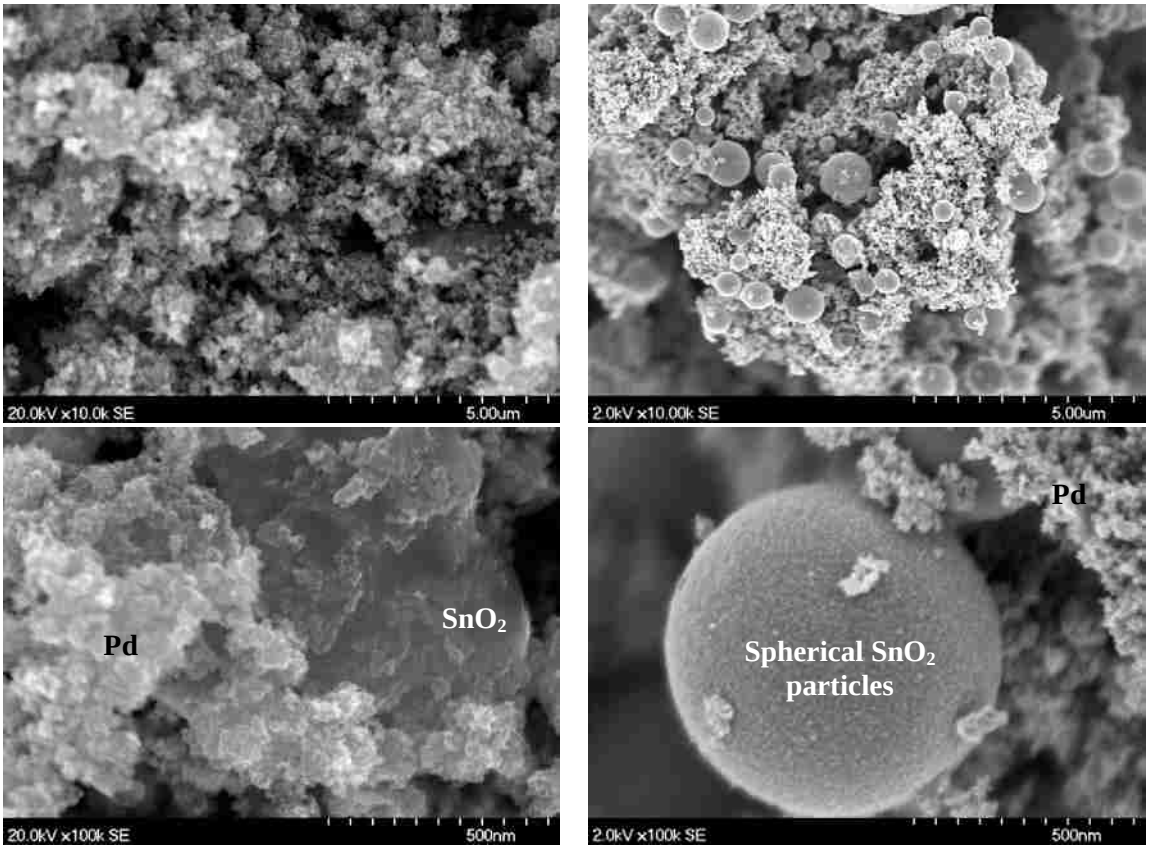

Figure 9-2. SEM micrographs of Pd/SnO_2 electrocatalysts.

Left: Pd/SnO_2(SS), Right: Pd/SnO_2(SP).

9.3.2 Electrochemical Performance

The electrocatalytic activity of these synthesized catalysts was studied for the electrooxidation of ethanol in an alkaline environment. Figure 9.3 shows the cyclic voltammograms in 1M KOH of both catalysts and a chemically reduced pure Pd catalyst for comparison. Onset potentials for all catalysts are similar, -0.64 V (vs. Hg/HgO) for pure Pd, -0.62 V for Pd/SnO_2(SP) and -0.61V for Pd/SnO_2(SS). Both Pd/SnO_2 catalysts demonstrate better kinetics than pure Pd catalyst. However, peak current density for the Pd/SnO_2(SP) catalyst is three times that of Pd/SnO_2(SS) and pure Pd metal. Peak current densities are observed due to the passivation of the Pd catalysts. As the Pd is oxidized to

form PdO, further adsorption of ethanol is inhibited resulting in the sudden decrease of current density.

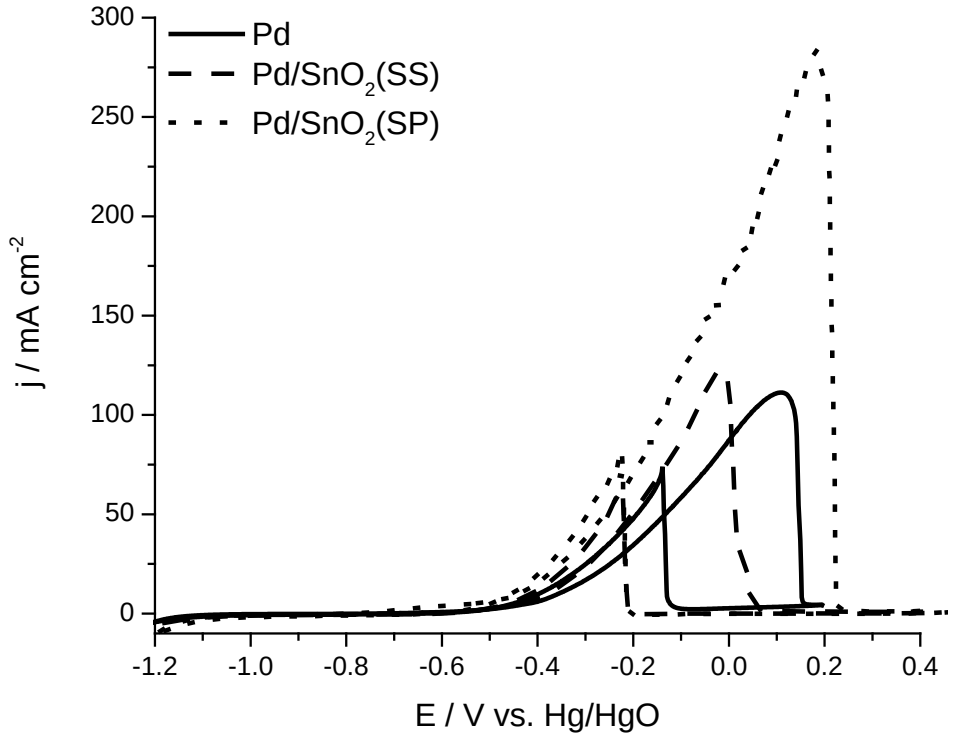

Figure 9-3. Cyclic voltammograms of Pd/SnO_2 catalysts in 1 M KOH at 22°C. Other conditions: 20 mV/s, 1M ethanol.

Further electrochemical analysis was performed along with the *in situ* infrared studies to provide a better understanding of the mechanism of reaction of the Pd/SnO_2(SP) catalyst at two different concentrations of electrolyte, 1.0 M and 0.1 M KOH.

9.3.3 Mechanistic Studies

In situ infrared reflection absorbance spectroscopy (IRRAS) studies were conducted in order to understand the mechanism of reaction of the highly active Pd/SnO_2(SP) at two different electrolyte concentrations. Figure 9.4a shows the infrared spectra for the ethanol oxidation reaction in a 1 M KOH electrolyte (1M ethanol). All spectra shown in Figure 9.4a and 9.5a are compared to a reference spectrum taken at the starting potential. Therefore, a trough represents the disappearance of species, while a peak represents a new kind of species being formed. The ethanol adsorption and oxidation can be followed by the characteristic infrared peaks for ethanol at 1086 cm^{-1} and 1045 cm^{-1} which correspond to the C-O stretch in C-C-O. Figure 9.4b shows the forward sweep of the cyclic voltammogram of the corresponding oxidation of ethanol at 1 mV/s. Plotted on the opposite y-axis are the calculated areas for characteristic peaks for ethanol (1045 cm^{-1}) and acetate (1410 cm^{-1}) as a function of the potential applied. The overlay of these peak areas together with the forward sweep of the cyclic voltammogram allows the visualization of the ethanol oxidation process. From figure 9.4b, the adsorption of ethanol can be observed to start at -0.94 V. Since a current is produced along with the increase of ethanol, the absorption of ethanol must proceed in the following way:

$$CH_3CH_2OH + OH^- \rightarrow CH_3CH_2O_{ads} + H_2O + 1e^- \qquad (9.4)$$

As the potential increases the onset potential for the oxidation of ethanol can be observed to start at -0.61 V. At this potential, acetate products start to appear. Acetate formation can be clearly observed from the characteristic infrared peaks at 1549 cm^{-1} and 1410 cm^{-1} which correspond to the C-O-O out-of-phase and in-phase stretch,

respectively. The presence of acetate species appear exactly at the onset potential of the ethanol oxidation. The amount of acetate produced increases as the potential is being increased reaching a maximum at the peak of the current density (-0.10 V). A maximum in the current density is observed due to the passivation of the Pd catalyst due to the formation of PdO; hence, losing its electrochemical activity. No other products or intermediates are present in the infrared spectra, although acetaldehyde formation, which might be an intermediate of the acetate formation, could be masked by the O-H vibration of the electrolyte at around 1630 cm^{-1}. Thus, according to these findings the electrooxidation of ethanol on Pd/SnO_2(SP) catalysts in a 1M KOH electrolyte might follow the overall reaction pathway below:

$$CH_3CH_2O_{ads} + 3OH^- \rightarrow CH_3COOH + 2H_2O + 3e^- \quad (9.5)$$

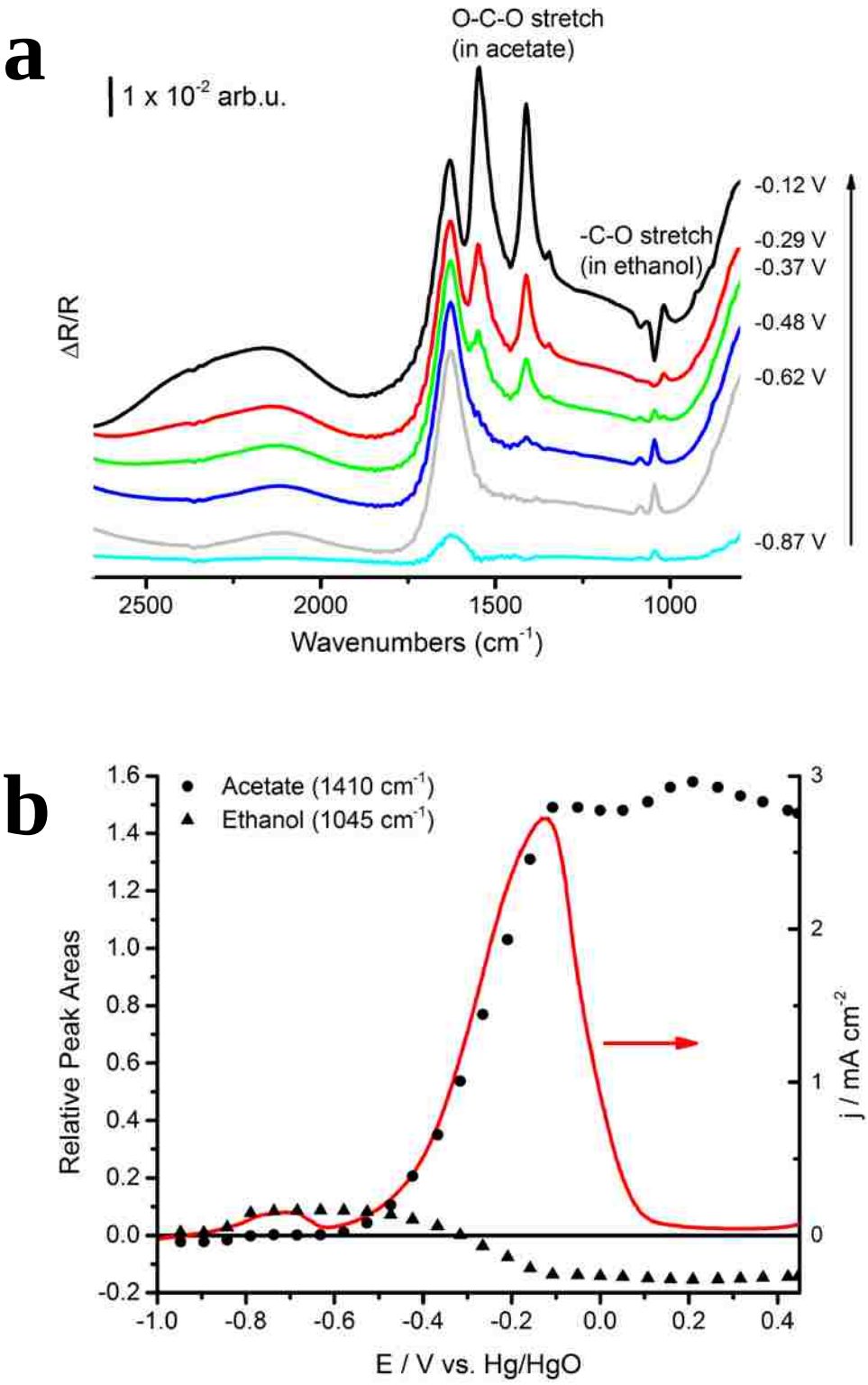

Figure 9-4. (a) IRRAS spectra of the ethanol oxidation by Pd/SnO_2 (SP) in a 1 M KOH electrolyte. (b) LSV of the oxidation reaction. Conditions: 1M ethanol, 1 mV/s, 22°C, 0rpm.

In order to better understand the role of the promotion effect of SnO_2 on Pd, *in situ* IRRAS were carried on spray pyrolyzed SnO_2 particles using the same conditions as the electrooxidation on Pd/SnO_2(SP). SnO_2 alone is inactive for the electrooxidation of ethanol, thus only developments on the spectra as a function of potential will be relevant to the better understanding of its contribution to the electroxidation of ethanol. Figure 9.5 displays the infrared spectra as a function of an applied potential for SnO_2 particles in 1M KOH electrolyte and 1M ethanol. The most active region for SnO_2 is the OH stretch region around 3200-3600 cm^{-1}. The presence of OH species starts to appear at about -0.58 V, which correlates with the onset potential for the ethanol electrooxidation on Pd/SnO_2 catalysts. These findings confirm that the presence of the SnO_2 promotes the oxidation of ethanol to acetate in a 1M KOH electrolyte by bringing hydroxide species to the surface of the electrode for the oxidation of the $CH_3CH_2O_{ads}$ species. Acetate production from $CH_3CH_2O_{ads}$ will require the dehydrogenation and further oxidation of adsorbed species which might proceed according to the following reactions,

$$CH_3CH_2O_{ads} + 2OH^- \rightarrow CH_3CO_{ads} + 2H_2O + 2e^- \quad (9.6)$$

$$CH_3CO_{ads} + OH^-_{ads} \rightarrow CH_3COOH + 1e^- \quad (9.7)$$

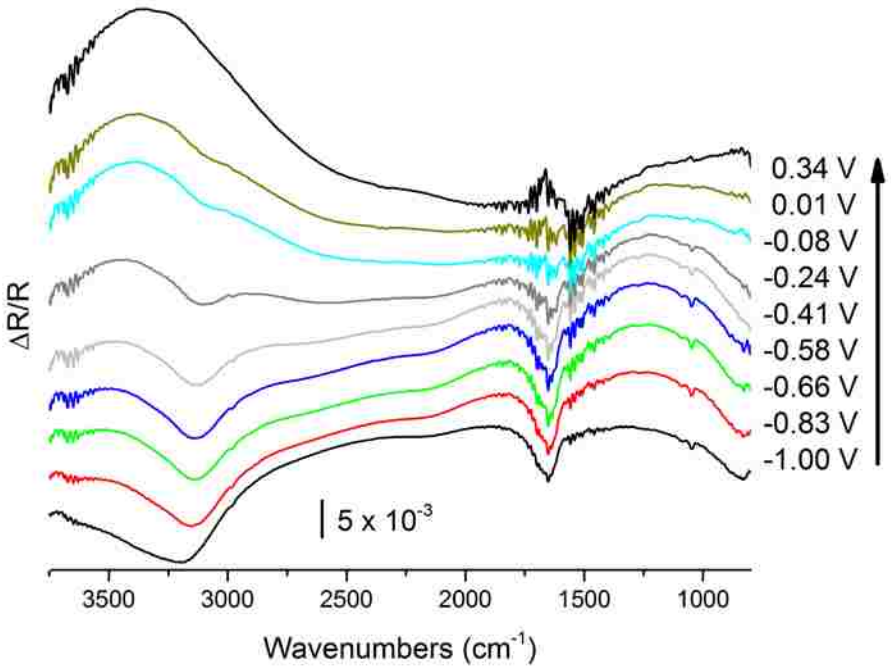

Figure 9-5. IRRAS spectra of SnO_2 in 1M KOH, 1M ethanol solution.

Electrolyte concentration effects have already been suggested by a few publications [106]. The fact that hydroxide ions are involved in the removal of the $CH_3CH_2O_{ads}$ species might indicate that the hydroxide ion concentration might play a role in the reaction pathway. The following studies were performed at a lower KOH concentration of 0.1 M. Figure 9.6a shows infrared spectra for the ethanol electrooxidation in a 0.1 M KOH solution. At first glance, it is clear to observe that the mechanism of oxidation is completely different from the one observed for a 1M KOH concentration. It is not clear if infrared peaks for acetate are observed. However, the appearance of a peak at 1408 cm^{-1} together with the broadening of the peak centered around 1626 cm^{-1} might indicate that acetate is being formed. Nevertheless, carbonate and CO_2 vibrations are observed at 1270 cm^{-1} and 2340 cm^{-1}, respectively. The presence of carbonate and CO_2 species indicate that complete ethanol oxidation is possible at

lower electrolyte concentrations. From figure 9.6b, the onset potential for the ethanol oxidation reaction occurs at -0.45 V, 160 mV higher than the onset potential observed in a 1 M KOH electrolyte solution. As the concentration of hydroxide ions in the bulk solution is decreased but the ethanol concentration remains the same, the diffusion of hydroxide ions to the electrochemical double layer will be limited and only ethanol will be able to diffuse through to adsorb on Pd (Figure 9.6b). Therefore, the coverage of the surface of the electrode will be dominated by adsorbed ethanol molecules. IRRAS spectra for only SnO_2 particles in a 0.1 M KOH electrolyte solution do not show any activity for the potential range swept (not shown). Slow kinetics due to the limited hydroxide ions allows for ethanol to proceed through to the full oxidation cleaving the C-C bond. Figure 9.6b plots the COOH, CO_2, and CH_3CH_2OH species along with the forward sweep of the potential. It is clear from the cyclic voltammetry as well as the relative peak area behavior that the cleavage of the C-C bond occurs at -0.16 V where the CO_2 and carbonate (O=C-OH) species start to appear. From figure 9.6b it can be observed ethanol adsorption reaches a maximum at the onset potential, where ethanol possibly partially oxidizes to acetate or carbonate. CO_2 species only start to appear 290 mV after the onset potential. Before CO_2 starts to appear, all of the adsorbed ethanol has been converted to an intermediate, either acetate or carbonate, as observed from the relative peak areas of ethanol in figure 9.6b. Since the potential where the CO_2 starts to appear (-0.16 V), corresponds to end of ethanol adsorption, it could be assumed that the vibrations occurring at 1270 cm^{-1} correspond to the COOH phase in acetate, *i.e.* -C-COOH.

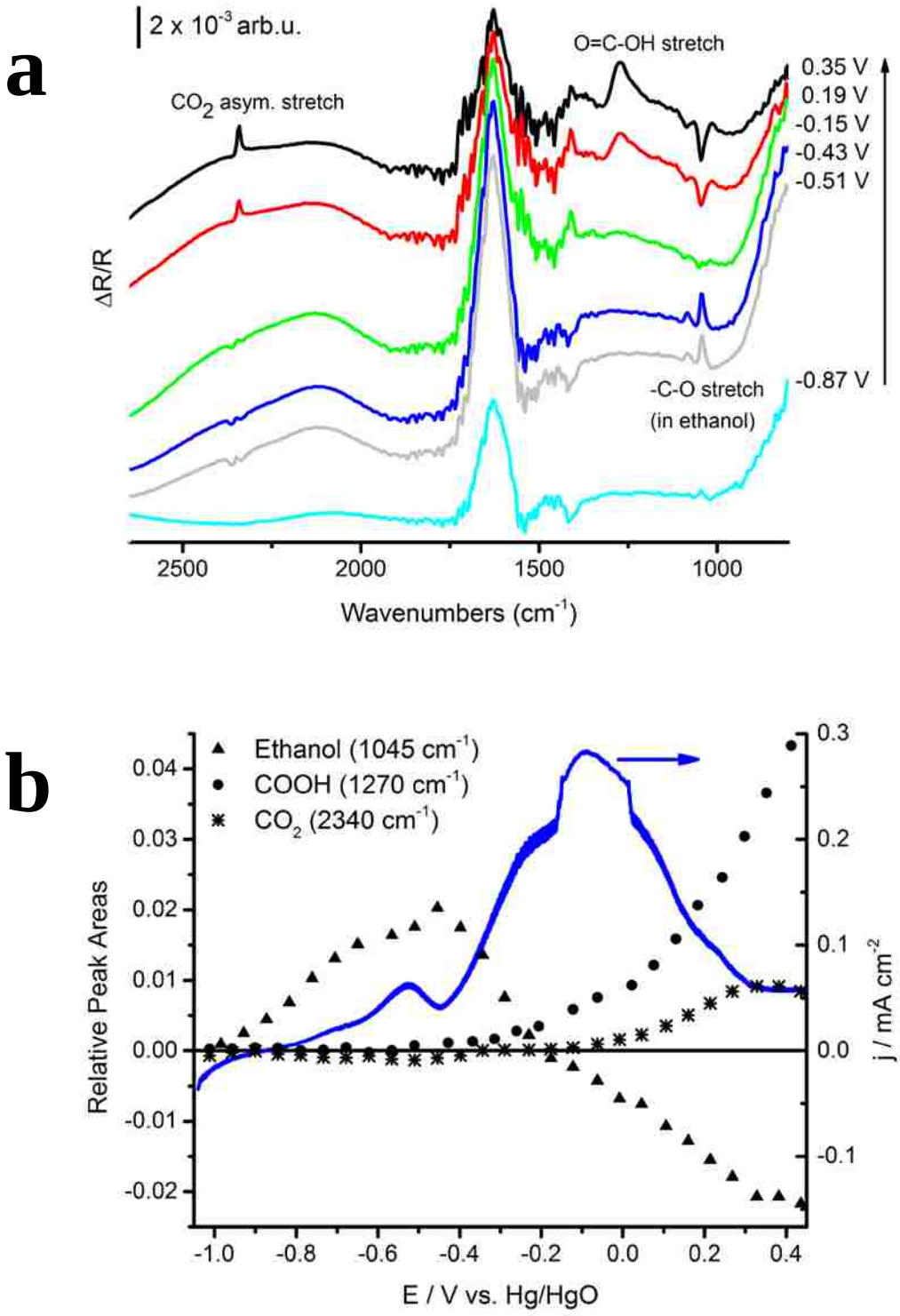

Figure 9-6 (a) IRRAS spectra of the ethanol oxidation by Pd/SnO_2 (SP) in a 0.1 M KOH electrolyte. (b) LSV of the oxidation reaction. Conditions: 1M ethanol, 1 mV/s, 22°C, 0rpm.

Table 9-1. IRRAS band assignments for the electrooxidation of ethanol.

Wavenumber (cm^{-1})	Assignment
3200-3400	OH stretch
2340	CO_2 assym. stretch
~1600	OH bend
1549, 1410	O-C-O stretch (in acetate)
1270	C-O stretch (in -COOH)
1086, 1045	C-O stretch (in –C-C-O)
801, 840	OH deformations

Tafel plots of both reactions were derived from the forward sweep voltammogram shown in 9.4b and 9.6b which were performed at 1 mV/s. Tafel slopes and exchanged current densities were calculated and tabulated below (Table 9.2).

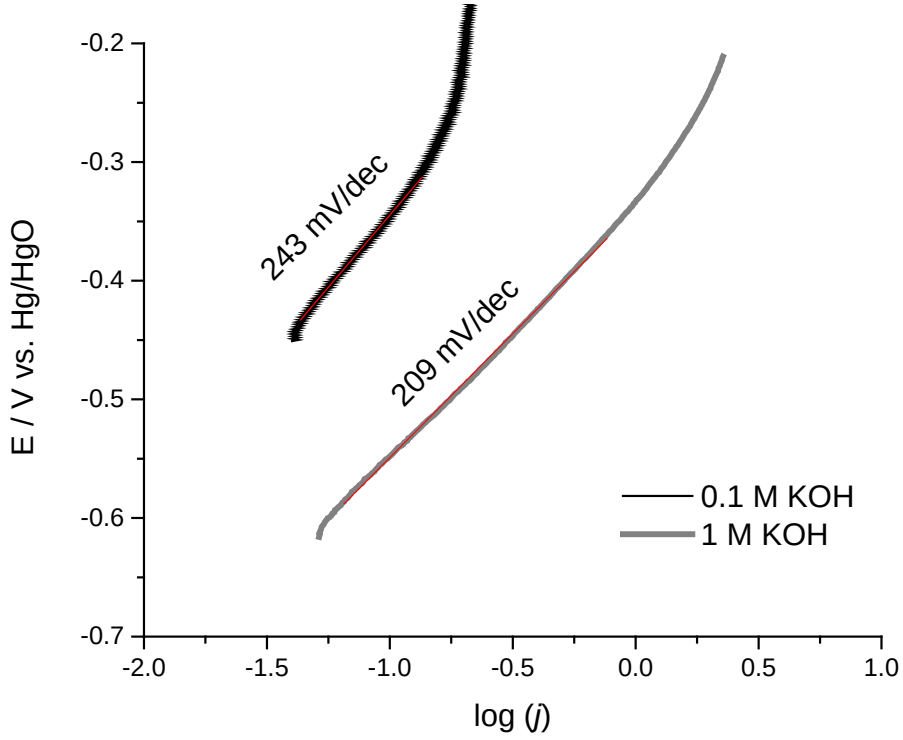

Figure 9-7. Calculated Tafel slopes for the electrooxidation of ethanol in two different electrolyte concentrations.

Table 9-2. Tafel constants calculated for the electrooxidation of ethanol on Pd/SnO_2(SP) catalysts at two different concentrations of electrolyte.

Electrolyte concentration	Tafel slope ($mV\ dec^{-1}$)	Exchange current density ($mA\ cm^{-2}$)
1 M KOH	209	42.3
0.1 M KOH	243	2.6

The combination of the information obtained from the Tafel plot calculations with the data obtained from the infrared studies could be interpreted in the following manner. Justification has been given for the mechanism of reaction in a 1 M KOH electrolyte (equations 9.6 and 9.7). Similar Tafel slopes for the reactions occurring near the onset potentials for both electrolyte concentrations could indicate a similar reaction mechanism resulting in acetate production. However, due to limited concentration of hydroxide ions at the surface of the electrode for a 0.1 M KOH electrolyte the rate of reaction is much lower. Exchange current densities from table 9.2 indicate that the rate of reaction is about 15 times faster for a 1 M KOH electrolyte than for a 0.1 M KOH electrolyte. Limited oxidation of adsorbed CH_3CO species could proceed to the C-C cleavage according to the following pathway,

$$CH_3CO_{ads} \rightarrow CH_{3ads} + CO_{ads} \qquad (9.8)$$

The resulting adsorbed species can then be further oxidized to produce CO_2 as observed in the infrared spectra from figure 9.6a.

9.4 Conclusions

Two different synthesis methods were compared for the synthesis of Pd/SnO_2 electrocatalysts for the electrooxidation of ethanol. XRD data showed FCC Pd as well as SnO_2 phases present. Crystallite sizes were similar for Pd, but the spray pyrolysis synthesis method resulted in smaller SnO_2 crystallite sizes than the sacrificial support method, 3.3 nm vs. 4.6 nm, respectively. Better dispersion of Pd on SnO_2 was observed for the Pd/SnO_2(SP) catalysts due to the smaller particle size and morphology of the SnO_2 phase. Current densities obtained from the Pd/SnO_2(SP) catalyst was three times higher than Pd/SnO_2(SS) and Pd. Mechanistic studies deduced from *in situ* IRRAS studies inferred that electrolyte concentration affects the kinetics and selectivity of the ethanol reaction. When the concentration of the hydroxide ions is higher (1 M), diffusion of these ions is possible to the electrochemical double layer and participate in the electrooxidation of the ethanol adsorbed species forming acetate. On the other hand, when lower concentrations of electrolyte are used (0.1 M), the diffusion of the hydroxide ions to the surface of the electrode is limited. This increases the overpotential of the onset potential by 160 mV. However, slow kinetics of the oxidation reaction and limited presence of hydroxide ions near the surface of the electrode permit complete oxidation of ethanol to CO_2 starting at a potential of -0.15 V.

10. Concluding Remarks and Future Outlook

10.1 Direct Hydrazine Anionic Fuel Cells

Successful development of novel electrocatalysts for the oxidation of hydrazine hydrate was achieved by the study of promotion effects caused by alloying as well as the presence of an oxide phase. Synthesis of electrocatalysts was performed via the spray pyrolysis of metal nitrate precursors which resulted in uniform hollow particles with homogenous compositions. This synthesis method provides the advantage of a facile scale-up process. Thus, potential production of the new catalysts developed for fuel cell applications is only a step away. Developed electrocatalysts were based on cheap and more abundant transition and rare-earth metals, making alkaline fuel cell technology more affordable than PEMFCs.

10.2 Direct Ethanol Anionic Fuel Cells

Thorough studies of the ethanol oxidation in alkaline environments using highly active Pd/SnO_2 electrocatalysts has provided insightful information about the selectivity of the oxidation reaction in response to different electrolyte concentrations. It was concluded that faster kinetics were observed at higher concentrations of hydroxide ions. However, the only product of the oxidation reaction is acetate. On the other hand, at lower concentrations of electrolyte, slower kinetics are observed but complete oxidation of ethanol to CO_2 is accomplished. It was concluded that complete oxidation of ethanol is possible to the limited diffusion of hydroxide ions to the surface of the electrode.

However, reaction rates for the complete oxidation are more than an order in magnitude lower than the partial oxidation of ethanol to acetate.

10.3 Future Outlook of the Development of Direct Alkaline Fuel Cells

Recent developments in the area of alkaline fuel cells might indicate that fuel cell operation in alkaline environments could make the application of fuel cell technologies more affordable. The wider range of possible materials to be used permits a better fine-tuning of novel electrocatalysts. A combination of already developed *ex situ* characterization techniques along with emerging *in situ* techniques provide a powerful tool to tackle challenges encountered in catalyst development. Lastly, promotion of catalysis was confirmed from binary catalytic systems either by alloying or a synergistic effect by the presence of an oxide phase. A combination of both promotion effects could lead to more selective and better performing electrocatalysts.

11. References

[1] S.M. Haile, Acta Materialia, 51 (2003) 5981-6000.
[2] K.A. Mauritz, R.B. Moore, Chemical Reviews, 104 (2004) 4535-4585.
[3] K. Kordesch, J. Gsellmann, B. Kraetschner, Proceedings of Power Sources, 9 (1983) 379.
[4] E. Gulzow, Journal of Power Sources, 61 (1996) 99-104.
[5] J.R. Varcoe, R.C.T. Slade, Fuel Cells, 5 (2005) 187-200.
[6] G. Couture, A. Alaaeddine, F. Boschet, B. Ameduri, Prog Polym Sci, 36 (2011) 1521-1557.
[7] J.R. Varcoe, R.C.T. Slade, E.L.H. Yee, S.D. Poynton, D.J. Driscoll, D.C. Apperley, Chem Mater, 19 (2007) 2686-2693.
[8] M. Tanaka, K. Fukasawa, E. Nishino, S. Yamaguchi, K. Yamada, H. Tanaka, B. Bae, K. Miyatake, M. Watanabe, J Am Chem Soc, 133 (2011) 10646-10654.
[9] J.S. Spendelow, A. Wieckowski, Physical Chemistry Chemical Physics, 9 (2007) 2654.
[10] A.V. Tripkovic, K.D. Popovic, B.N. Grgur, B. Blizanac, P.N. Ross, N.M. Markovic, Electrochimica Acta, 47 (2002) 3707-3714.
[11] S.C.S. Lai, S.E.F. Kleijn, F.T.Z. Öztürk, V.C. van Rees Vellinga, J. Koning, P. Rodriguez, M.T.M. Koper, Catalysis Today, 154 (2010) 92-104.
[12] F.T. Bacon, British Patent 725,661, in, 1955.
[13] F.T. Bacon, British Patent 667,298, in, 1950.
[14] H. Helmholtz, Pogg. Ann., LXXXIX (1853) 211.
[15] L.G. Gouy, Comt. Rend., 149 (1909).
[16] L.G. Gouy, J. Phys., 9 (1910).
[17] D.L. Chapman, Philos Mag, 25 (1913) 475-481.
[18] O. Stern, Z Elktrochem Angew P, 30 (1924) 508-516.
[19] A.J. Bard, L.R. Faulkner, Electrochemical methods, John Wiley & Sons Inc, 2001.
[20] A. Gurav, T. Kodas, T. Pluym, Y. Xiong, Aerosol Science and Technology, 19 (1993) 411 - 452.
[21] G.L. Messing, S.C. Zhang, G.V. Jayanthi, Journal of the American Ceramic Society, 76 (1993) 2707-2726.
[22] N.V. Rees, R.G. Compton, Energ Environ Sci, 4 (2011) 1255-1260.
[23] M.T.M. Koper, V. Rosca, M. Duca, M.T. de Groot, Chemical Reviews, 109 (2009) 2209-2244.
[24] A. Serov, C. Kwak, Appl Catal B-Environ, 98 (2010) 1-9.
[25] E.H. Yu, X. Wang, U. Krewer, L. Li, K. Scott, Energy & Environmental Science, 5 (2012) 5668-5680.
[26] A.J. Bard, Analytical Chemistry, 35 (1963) 1602-1607.
[27] G.E. Evans, K.V. Kordesch, Science, 158 (1967) 1148-1152.
[28] R.F. Kimball, Mutation Research/Reviews in Genetic Toxicology, 39 (1977) 111-126.
[29] K. Asazawa, K. Yamada, H. Tanaka, A. Oka, M. Taniguchi, T. Kobayashi, Angewandte Chemie International Edition, 46 (2007) 8024-8027.
[30] S. Karp, L. Meites, The Journal of the American Chemical Society, 84 (1966) 906-912.
[31] K. Yamada, K. Yasuda, N. Fujiwara, Z. Siroma, H. Tanaka, Y. Miyazaki, T. Kobayashi, Electrochemistry Communications, 5 (2003) 892-896.
[32] K. Asazawa, T. Sakamoto, S. Yamaguchi, K. Yamada, H. Fujikawa, H. Tanaka, K. Oguro, Journal of The Electrochemical Society, 156 (2009) B509-B512.
[33] K. Asazawa, K. Yamada, H. Tanaka, M. Taniguchi, K. Oguro, Journal of Power Sources, 191 (2009) 362-365.
[34] J. Sanabria-Chinchilla, K. Asazawa, T. Sakamoto, K. Yamada, H. Tanaka, P. Strasser, J Am Chem Soc, 133 (2011) 5425-5431.
[35] T. Sakamoto, K. Asazawa, K. Yamada, H. Tanaka, Catalysis Today, 164 (2011) 181-185.

[36] U. Martinez, K. Asazawa, B. Halevi, A. Falase, B. Kiefer, A. Serov, M. Padilla, T. Olson, A. Datye, H. Tanaka, P. Atanassov, Physical Chemistry Chemical Physics, 14 (2012) 5512.
[37] S.-i. Yamazaki, T. Ioroi, K. Tanimoto, K. Yasuda, K. Asazawa, S. Yamaguchi, H. Tanaka, Journal of Power Sources, 204 (2012) 79-84.
[38] F.X. Zhang, H.M. Zhang, J.X. Ren, C. Qu, J Mater Chem, 20 (2010) 8139-8146.
[39] V. Rosca, M.T.M. Koper, Electrochimica Acta, 53 (2008) 5199-5205.
[40] R.G. Compton, L. Aldous, Physical Chemistry Chemical Physics, 13 (2011) 5279-5287.
[41] T. Kodera, M. Honda, H. Kita, Electrochimica Acta, 30 (1985) 669-675.
[42] L.Q. Ye, Z.P. Li, H.Y. Qin, J.K. Zhu, B.H. Liu, Journal of Power Sources, 196 (2011) 956-961.
[43] J. Zhao, M. Zhu, M. Zheng, Y. Tang, Y. Chen, T. Lu, Electrochimica Acta, 56 (2011) 4930-4936.
[44] Y. Fukumoto, T. Matsunaga, T. Hayashi, Electrochimica Acta, 26 (1981) 631-636.
[45] N.V. Korovin, B.N. Yanchuk, Electrochimica Acta, 15 (1970) 569-&.
[46] G. Gao, D. Guo, C. Wang, H. Li, Electrochemistry Communications, 9 (2007) 1582-1586.
[47] G.-W. Yang, G.-Y. Gao, C. Wang, C.-L. Xu, H.-L. Li, Carbon, 46 (2008) 747-752.
[48] K. Korínek, J. Koryta, M. Musilová, Journal of Electroanalytical Chemistry and Interfacial Electrochemistry, 21 (1969) 319-327.
[49] J.A. Harrison, Z.A. Khan, Journal of Electroanalytical Chemistry, 26 (1970) 1-&.
[50] M. Fleischmann, K. Korinek, D. Pletcher, Journal of Electroanalytical Chemistry and Interfacial Electrochemistry, 34 (1972) 499-503.
[51] H. Tanaka, K. Asazawa, T. Sakamoto, T. Kato, M. Kai, S. Yamaguchi, K. Yamada, H. Fujikawa, Ecs Transactions, 16 (2008) 459-464.
[52] J. Schwank, AIChE Journal, 31 (1985) 1405.
[53] M.T.M. Koper, Surface Science, 548 (2004) 1-3.
[54] D.A. Konopka, M. Li, K. Artyushkova, N. Marinkovic, K. Sasaki, R. Adzic, T.L. Ward, P. Atanassov, J. Phys. Chem. C, 115 (2011) 3043-3056.
[55] P.W. Faguy, N.S. Marinkovic, Appl Spectrosc, 50 (1996) 394-400.
[56] D. Jung, S. Park, Y. Kang, Korean Journal of Chemical Engineering, 27 (2010) 1621-1645.
[57] D.A. Konopka, S. Pylypenko, P. Atanassov, T.L. Ward, ACS Appl. Mater. Interfaces, 2 (2010) 86-95.
[58] E.E. Switzer, A.K. Datye, P. Atanassov, Top. Catal., 46 (2007) 334-338.
[59] E.E. Switzer, T.S. Olson, A.K. Datye, P. Atanassov, M.R. Hibbs, C.J. Cornelius, Electrochimica Acta, 54 (2009) 989-995.
[60] H. Okamoto, Journal of Phase Equilibria, 24 (2003) 280-281.
[61] W.W. Liang, Y.A. Chang, S. Lau, Acta Metallurgica, 21 (1973) 629-637.
[62] S. Kameoka, T. Kimura, A.P. Tsai, Catal Lett, 131 (2009) 219-224.
[63] J.L. Gland, G.B. Fisher, G.E. Mitchell, Chem Phys Lett, 119 (1985) 89-92.
[64] P.A. Giguere, I.D. Liu, J Chem Phys, 20 (1952) 136-140.
[65] T. Tipton, D.A. Stone, K. Kubulat, W.B. Person, J Phys Chem-Us, 93 (1989) 2917-2927.
[66] H.D. Kaesz, R.B. Saillant, Chemical Reviews, 72 (1972) 231-&.
[67] A. Serov, U. Martinez, A. Falase, P. Atanassov, Electrochemistry Communications, 22 (2012) 193-196.
[68] P.K. Shen, C. Xu, Electrochemistry Communications, 8 (2006) 184-188.
[69] G. Karim-Nezhad, R. Jafarloo, P.S. Dorraji, Electrochimica Acta, 54 (2009) 5721-5726.
[70] W. Ye, B. Yang, G. Cao, L. Duan, C. Wang, Thin Solid Films, 516 (2008) 2957-2961.
[71] E. Antolini, J. Perez, International Journal of Hydrogen Energy, 36 (2011) 15752-15765.
[72] C. Xu, P.k. Shen, Y. Liu, Journal of Power Sources, 164 (2007) 527-531.
[73] C. Xu, Z. Tian, P. Shen, S.P. Jiang, Electrochimica Acta, 53 (2008) 2610-2618.
[74] R.P. Taylor, G.L. Schrader, Ind Eng Chem Res, 30 (1991) 1016-1023.

[75] S. Bernal, F.J. Botana, R. Garcia, J.M. Rodriguezizquierdo, Thermochim Acta, 66 (1983) 139-145.
[76] M.F. Sunding, K. Hadidi, S. Diplas, O.M. Lovvik, T.E. Norby, A.E. Gunnaes, J Electron Spectrosc, 184 (2011) 399-409.
[77] Y. Uwamino, T. Ishizuka, H. Yamatera, J Electron Spectrosc, 34 (1984) 67-78.
[78] D. Stoychev, I. Valov, P. Stefanov, G. Atanasova, M. Stoycheva, T. Marinova, Mat Sci Eng C-Bio S, 23 (2003) 123-128.
[79] W.Y. Howng, R.J. Thorn, J Phys Chem Solids, 41 (1980) 75-81.
[80] G.A. Camara, T. Iwasita, Journal of Electroanalytical Chemistry, 578 (2005) 315-321.
[81] H. Wang, Z. Jusys, R.J. Behm, The Journal of Physical Chemistry B, 108 (2004) 19413-19424.
[82] E. Antolini, Journal of Power Sources, 170 (2007) 1-12.
[83] J.K. Norskov, T. Bligaard, J. Rossmeisl, C.H. Christensen, Nat Chem, 1 (2009) 37-46.
[84] F. Colmati, E. Antolini, E.R. Gonzalez, Journal of Power Sources, 157 (2006) 98-103.
[85] W.J. Zhou, S.Q. Song, W.Z. Li, G.Q. Sun, Q. Xin, S. Kontou, K. Poulianitis, P. Tsiakaras, Solid State Ionics, 175 (2004) 797-803.
[86] C. Lamy, S. Rousseau, E.M. Belgsir, C. Coutanceau, J.M. Léger, Electrochimica Acta, 49 (2004) 3901-3908.
[87] L. Jiang, G. Sun, S. Sun, J. Liu, S. Tang, H. Li, B. Zhou, Q. Xin, Electrochimica Acta, 50 (2005) 5384-5389.
[88] Q. Wang, G.Q. Sun, L.H. Jiang, Q. Xin, S.G. Sun, Y.X. Jiang, S.P. Chen, Z. Jusys, R.J. Behm, Physical Chemistry Chemical Physics, 9 (2007) 2686-2696.
[89] J.P.I. de Souza, S.L. Queiroz, K. Bergamaski, E.R. Gonzalez, F.C. Nart, The Journal of Physical Chemistry B, 106 (2002) 9825-9830.
[90] K. Bergamaski, E.R. Gonzalez, F.C. Nart, Electrochimica Acta, 53 (2008) 4396-4406.
[91] N. Markovic, H. Gasteiger, P.N. Ross, Journal of The Electrochemical Society, 144 (1997) 1591-1597.
[92] B.B. Blizanac, P.N. Ross, N.M. Markovic, Electrochimica Acta, 52 (2007) 2264-2271.
[93] C. Coutanceau, L. Demarconnay, C. Lamy, J.M. Léger, Journal of Power Sources, 156 (2006) 14-19.
[94] E.R. Choban, J.S. Spendelow, L. Gancs, A. Wieckowski, P.J.A. Kenis, Electrochimica Acta, 50 (2005) 5390-5398.
[95] C. Xu, L. Cheng, P. Shen, Y. Liu, Electrochemistry Communications, 9 (2007) 997-1001.
[96] L.M.D.C.R. Chen, D. Chu, R. Chen, International Journal of Hydrogen Energy, 37 (2012) 11185-11194.
[97] E. Antolini, E.R. Gonzalez, Journal of Power Sources, 195 (2010) 3431-3450.
[98] F. Hu, C. Chen, Z. Wang, G. Wei, P.K. Shen, Electrochimica Acta, 52 (2006) 1087-1091.
[99] V. Bambagioni, C. Bianchini, J. Filippi, W. Oberhauser, A. Marchionni, F. Vizza, R. Psaro, L. Sordelli, M.L. Foresti, M. Innocenti, ChemSusChem, 2 (2009) 99-112.
[100] Z.X. Liang, T.S. Zhao, J.B. Xu, L.D. Zhu, Electrochimica Acta, 54 (2009) 2203-2208.
[101] E.D. Wang, J.B. Xu, T.S. Zhao, The Journal of Physical Chemistry C, 114 (2010) 10489-10497.
[102] A. Kowal, M. Li, M. Shao, K. Sasaki, M.B. Vukmirovic, J. Zhang, N.S. Marinkovic, P. Liu, A.I. Frenkel, R.R. Adzic, Nat Mater, 8 (2009) 325-330.
[103] R.B. Kutz, B. Braunschweig, P. Mukherjee, R.L. Behrens, D.D. Dlott, A. Wieckowski, Journal of Catalysis, 278 (2011) 181-188.
[104] F. Vigier, C. Coutanceau, F. Hahn, E.M. Belgsir, C. Lamy, Journal of Electroanalytical Chemistry, 563 (2004) 81-89.
[105] Z.-Y. Zhou, Q. Wang, J.-L. Lin, N. Tian, S.-G. Sun, In situ FTIR spectroscopic studies of electrooxidation of ethanol on Pd electrode in alkaline media, in: Electrochimica Acta, 2010, pp. 7995-7999.

[106] X. Fang, L. Wang, P.K. Shen, G. Cui, C. Bianchini, Journal of Power Sources, 195 (2010) 1375-1378.
[107] R.M. Modibedi, T. Masombuka, M.K. Mathe, International Journal of Hydrogen Energy, 36 (2011) 4664-4672.
[108] W. Du, K.E. Mackenzie, D.F. Milano, N.A. Deskins, D. Su, X. Teng, ACS Catalysis, 2 (2012) 287-297.
[109] Z. Zhang, L. Xin, K. Sun, W. Li, International Journal of Hydrogen Energy, 36 (2011) 12686-12697.
[110] T. Maiyalagan, K. Scott, Journal of Power Sources, 195 (2010) 5246-5251.
[111] Q. He, W. Chen, S. Mukerjee, S. Chen, F. Laufek, Journal of Power Sources, 187 (2009) 298-304.